Forschungszentrum Karlsruhe
Technik und Umwelt

Wissenschaftliche Berichte
FZKA 6218

Neutronics of the IFMIF Neutron Source: Development and Analysis

Paul P.H. Wilson

Institut für Neutronenphysik und Reaktortechnik
Projekt Kernfusion

1999

Forschungszentrum Karlsruhe

Technik und Umwelt

Wissenschaftliche Berichte

FZKA 6218

Neutronics of the IFMIF Neutron Source: Development and Analysis

Paul P.H. Wilson

Institut für Neutronenphysik und Reaktortechnik
Projekt Kernfusion

Von der Fakultät für Maschinenbau der Universität Karlsruhe (TH)
genehmigte Dissertation

Forschungszentrum Karlsruhe GmbH, Karlsruhe
1999

Als Manuskript gedruckt

Forschungszentrum Karlsruhe GmbH
Postfach 3640, 76021 Karlsruhe

Mitglied der Hermann von Helmholtz-Gemeinschaft
Deutscher Forschungszentren (HGF)

ISSN 0947-8620

Neutronics of the IFMIF Neutron Source: Development and Analysis

Zur Erlangung des akademischen Grades eines

Doktors der Ingenieurwissenschaften

von der Fakultät für Maschinenbau der Universität Karlsruhe (TH)

genehmigte

Dissertation

von
Paul P.H. Wilson, M.S.
aus Edinburg (Schottland)

Tag der mündlichen Prüfung:	18. Dezember 1998
Hauptreferent:	Prof. Dr.-Ing. G. Keßler
Korreferenten:	Prof. Dr.rer.nat. Dr.h.c. Dan. G. Cacuci
	Prof. Dr. K. Ehrlich

Neutronics of the IFMIF Neutron Source: Development and Analysis

Abstract

The need to extend and improve our knowledge of the effects of irradiation on fusion materials through experimental analyses has led to the proposal of the International Fusion Materials Irradiation Facility [IFMIF]. This accelerator-driven facility will provide fusion-relevant neutron irradiation conditions by accelerating deuterium ions onto a liquid lithium target. Detailed neutronics calculations are needed for the conceptual validation, engineering design and operation of the facility. This work presents a detailed analysis of the neutron flux and various neutron responses (*e.g.* damage, gas production, activation, nuclear heating) throughout the high flux test region of the IFMIF test facility and for the reference High Flux Test Module design.

The most urgent need for characterisation of the IFMIF neutronics is to ensure that the current conceptual design is able to fulfil the facility's requirements, including criteria for minimum available irradiation volumes, maximum possible gradients and an appropriate simulation of a DT fusion environment. In addition, input is needed to improve and optimise IFMIF's engineering design.

The accurate analysis of this system required the development of a code system and methodology capable of modelling the various physical processes. A generic code system for the neutronics analysis of neutron sources has been created by loosely integrating existing components with new developments: the data processing code NJOY, the Monte Carlo neutron transport code MCNP, and the activation code ALARA were supplemented by a damage data processing program, damChar, and integrated with a number of flexible and extensible modules for the Perl scripting language.

Specific advances were required to apply this code system to IFMIF. Based on the ENDF-6 data format requirements of this system, new data evaluations have been implemented for neutron transport and activation. Extensive analysis of the Li(d,xn) reaction has led to a new MCNP source function module, M^{c}DeLi, based on physical reaction models and capable of accurate and flexible modelling of the IFMIF neutron source term.

In depth analyses of the neutron flux spectra and spatial distribution throughout the high flux test region permitted a basic validation of the tools and data. The understanding of the features of the neutron flux provided a foundation for the analyses of the other neutron responses.

A three-dimensional characterisation of the entire high flux test region includes a variety of primary neutron responses, including the flux distribution, flux gradients, gas production, damage rate, and nuclear heating. Secondary responses, such as the gas-to-damage ratio and decay heat, and detailed characterisations, such as the cumulative damage deposition function and the activation inventory, serve demonstrate the facility's suitability as a fusion simulation environment. Detailed analyses of the reference HFTM have provided suggested design changes and guidance for the HFTM loading patterns.

Programmentwicklung und neutronenphysikalische Analyse zur "International Fusion Materials Irradiation Facility (IFMIF)"

Kurzfassung

Die internationale Bestrahlungsanlage IFMIF (International Fusion Materials Irradiation Facility) wurde zur experimentellen Untersuchung des Bestrahlungsverhaltens von Fusionsreaktormaterialien konzipiert. IFMIF ist eine beschleunigergetriebene Neutronenquelle, bei der durch den Beschuss eines flüssigen Lithiumtargets mit hochenergetischen Deuteronen (40 MeV) ein intensiver Neutronenfluss unter fusionsreaktorrelevanten Bedingungen erzeugt wird. Für Konzeptentwurf und Auslegung sowie den späteren Betrieb der Anlage werden eine Vielzahl neutronenphysikalischer Daten benötigt. In der vorliegenden Arbeit wird das neutronenphysikalische Verhalten von IFMIF untersucht. Detaillierte Analysen der Neutronenflussdichteverteilungen und einer Reihe neutronenphysikalischer Grössen wie z. B. die strahleninduzierte Schädigung, die Gasproduktion, die Materialaktivierung und die nukleare Wärmeerzeugung werden für den Hochfluss-Testbereich und den Referenzentwurf des Hochfluss-Testmoduls von IFMIF dargestellt.

Die Zielsetzung der neutronenphysikalischen Analyse bestand darin, nachzuweisen, dass der vorliegende Entwurf von IFMIF die Anforderungen bezüglich des verfügbaren Bestrahlungsvolumens, des erreichbaren Flussdichtegradienten sowie der Eignung als Simulationsanlage für die Bestrahlungsbedingungen eines (d,t)-Fusionsreaktors, erfüllt. Darüber hinaus soll mit Hilfe der Ergebnisse der neutronenphysikalischen Analyse der Entwurf verbessert und optimiert werden.

Für diesen Zweck wurde ein umfassendes Programmsystem entwickelt, das eine neutronenphysikalische Analyse einer Neutronenquelle in allgemeiner Form ermöglicht. Das Programmsystem integriert vorhandene Komponenten und neue Entwicklungen: Das Kerndaten-Aufbereitungs-Programm NJOY, das Monte-Carlo-Teilchentransportprogramm MCNP sowie das Aktivierungsprogramm ALARA wurden ergänzt um ein Programm, damChar, zur Aufbereitung von Schädigungsdaten. Die Komponenten des Systems wurden schließlich mit Hilfe einer Reihe flexibler und erweiterbarer Perl-Skript-Modulen miteinander gekoppelt.

Zum Einsatz des Programmsystems für IFMIF waren weitere Entwicklungen erforderlich. Es wurden neue hochenergetische Kerndaten für den Neutronentransport und für Aktivierung in ENDF-6-Format aufbereitet und implementiert. Nach einer gründlichen Untersuchung des physikalischen Modells der neutronenerzeugenden Kernreaktion Li(d,xn) wurde für MCNP das Quellfunktionsmodul M^{c}DeLi erstellt, das den Quellterm basierend auf kernphysikalischen Reaktionsmodellen in geeigneter Weise beschreibt.

Detaillierte Analysen der Neutronenspektren und ihrer räumlichen Verteilung im Hochfluss-Testbereich ermöglichten eine grundlegende Validierung des Programmsystems und der verwendeten Daten. Das Verständnis des Verhaltens der Neutronenflussdichteverteilung bildet dabei die Grundlage für die Analyse weitere Reaktionsraten von Bedeutung.

Der gesamte Hochfluss-Testbereich wurde anhand dreidimensionaler Berechnungen neutronenphysikalisch charakterisiert; es wurden primäre neutronenphysikalische Grössen wie Neutronenflussdichteverteilungen, Flussdichtegradienten, die Gasproduktion, Schädigungsraten sowie die nukleare Wärmeerzeugung berechnet. Abgeleitete neutronenphysikalische Grössen wie das Verhältnis der Gasproduktion zur Schädigungsrate, die kumulative Schädigungsenergieübertragungsfunktion, die Nachwärmeerzeugung und die Materialaktivierung, die für die Eignung von IFMIF als fusionsrelevante Neutronenquelle von grundlegender Bedeutung sind, wurden ermittelt und analysiert. Ergebnisse der hier durchgeführten neutronenphysikalischen Analyse haben zu Änderungen im Entwurf des Hochfluss-Testmoduls geführt und zur Entwicklung eines geeigneten Beladungsmusters des Hochfluss-Testmodules beigetragen.

Contents

List of Figures

List of Tables

List of Symbols and Abbreviations

For more detailed descriptions of a symbol or abbreviation, consult the page where it is first introduced, shown in parentheses.

ϵ_b	binding energy of deuteron (23)
θ_c	angle of deflection caused by Coulomb barrier (26)
θ_n	neutron angle in laboratory frame of reference (23)
σ_{strip}	fitting parameter for stripping reaction channel, closely associated with total stripping cross section (29)
σ_{comp_o}	primary fitting parameter for compound nuclear reaction channel (29)
$\nu_j(L)$	number of displacements caused in material j by a recoil with damage energy L (15)
A	mass of compound nucleus (27)
$appm$	atom parts per million (59)
CDA	Conceptual Design Activities (4)
DPA	displacement per atom (2)
E^*	excitation energy of compound nucleus (27)
E_c	Coulomb barrier energy (26)
E_d	kinetic energy of deuteron (23)
E_{max}	maximum threshold deuteron energy for compound nuclear reaction channel (29)
E_n	neutron energy in laboratory frame of reference (23)
f_{comp_s}	secondary fitting parameter for compound nuclear reaction channel (29)
fpy	full-power-year (3)
$G(y, y_o, \sigma)$	Gaussian distribution centred at y_o with width σ (35)
$H(y)$	Heavyside step function (35)
$HFTM$	High Flux Test Module of the IFMIF CDA reference design (40)
IFMIF	International Fusion Materials Irradiation Facility (1)
$L_d^{ij}(T)$	Lindhard damage energy deposited in material j by recoil of type i with energy T (15)

M	mass of a neutron (23)
$P_i(E_n, T)$	production of recoil of type i with energy T from a neutron of energy E_n (15)
PKA	primary knock-on atom (2)
$\mathbf{p}$	momentum vector of the neutron relative to the centre-of-mass of the deuteron (23)
p	magnitude of $\mathbf{p}$ (23)
$p_\perp$	magnitude of component of $\mathbf{p}$ perpendicular to flight path of deuteron (23)
$p_{\perp_x}$	magnitude of component of $\mathbf{p}$ in plane tangent to nuclear surface at point of interaction (25)
p_b	deuteron binding energy ϵ_b expressed as a momentum (24)
p_o	momentum of deteron's centre-of-mass (23)
p_x	component of $\mathbf{p}$ (and of $p_\perp$) normal to nuclear surface at point of interaction (25)
p_z	component of $\mathbf{p}$ parallel to flight path of deuteron (23)
Q	energy release of ^{7}Li(d,xn)^{8}Be reaction = 15.02 MeV (29)
R	radius of target Li nucleus (22)
R_d	radius of deuteron (22)
T	kinetic energy of a PKA (14)
$W(L_d)$	cummulative distribution function of damage energy deposition with Lindhard damage energy as abscissa (15)
$W(E_n, L_d)$	operator for cummulative distribution function of damage energy deposition with Lindhard damage energy as abscissa (15)
$W(T)$	cummulative distribution function of damage energy deposition with PKA energy as abscissa (14)

Chapter 1

Introduction

Binding energy differences between nuclei, the most dense source of energy available, can be harnessed either by fissioning heavy nuclei or fusing lighter nuclei. Although both processes were discovered at about the same time, to date, we have only been able to successfully employ the fission reaction to generate electricity. One of the technical obstacles to fusion energy's implementation is the list of requirements for the materials, structural and otherwise, which will make up the fusion reactor. A greater understanding of the behaviour of present materials when exposed to high levels of neutron irradiation is required to ensure a safe and reliable fusion reactor design. An intensive neutron source must be built to provide a suitable environment to study the effects of radiation on these materials. For this purpose, the international fusion materials research community has recommended the development of the International Fusion Materials Irradiation Facility [IFMIF][1], an accelerator-driven intense neutron source based on existing technology. Computational estimates of the various neutron-induced effects on the samples irradiated within IFMIF will be important throughout its conceptualisation, design and operation. At the current stage of development, these estimates are important for two reasons: to demonstrate the suitability of IFMIF as a simulation of the (d,t)-fusion irradiation environment and to provide feedback for improvements in its engineering design.

The implementation of fusion energy systems is a natural continuation of our experience with fission-based nuclear power, offering the possibility of larger fuel supplies and smaller and cleaner waste streams.[2] Most recent research has focused on implementing the deuterium-tritium fusion fuel cycle:

$$D + T \rightarrow \alpha(3.514MeV) + n(14.056MeV).$$

Following recent successes of large fusion experiments such as the Tokamak Fusion Test Reactor [TFTR][3] in the USA and the Joint European Torus [JET][4] in Europe, fusion research has focused on the design of a "Next Step" reactor. The International Thermonuclear Experimental Reactor [ITER][5] is an example of such a reactor with hopes of reaching the ignition point of the plasma and having power levels approaching those of future power reactor. Expected to follow this "Next Step" machine is a reactor concept which truly demonstrates the capability of generating electricity from fusion energy, the so-called DEMO[6] reactor concept.

The behaviour of materials when subjected to radiation is just one of the physical and technological uncertainties which must be resolved during this development process. Fusion reactor materials have a number of different roles to play in the reliable operation of a reactor. The interface between the plasma and the structure, the *first wall*, has the primary role of minimising the plasma contamination by avoiding, as much as possible, the sputtering of material into the plasma. The *blanket* and *shield* immediately behind the first wall must absorb the neutrons and their energy to convert lithium to tritium as fuel, protect the radiation-sensitive magnets and generate the heat required for electricity production. At the same time, these materials are responsible for the structural integrity of the reactor.

The exposure to neutron radiation affects the ability of the materials to perform all of these tasks, but has a particularly strong influence on its structural integrity. Neutron-induced damage is caused by so-called "primary knock-on atoms", or PKA's, atoms of the base material knocked out of their lattice position by the neutron. These PKA's go on to collide with other atoms, transferring some of their energy, and possibly knocking them out of their lattice position. Many of these atoms find their way back to other stable lattice positions, only to be knocked out again by another collision. Radiation induced damage is often quantified by the number of displacements per atom [DPA], or the number of times, on average, that an atom has been knocked out of its lattice position. Full characterisation of the damage, however, also requires some knowledge of the form of those displacements. If the PKA is created with low energies, it will result in a small number of isolated displacements, known as point defects. PKA's with high energies will create large cascades of displacements, with a completely different final effect on the material from the point defects. In addition to this, neutron irradiation causes the production of gases, namely hydrogen and helium, within the grains of the material. The combination of these microscopic effects results in measurable macroscopic changes, either in the material parameters (such as the ductile-to-brittle transition temperature, yield strength and hardness), or the materials behaviour (such as swelling and creep). These macroscopic changes establish the lifetime of a component in the reactor, affecting the reactor's overall reliability and availabilty. Before designing a reactor it is important to know exactly how the structural integrity of the materials will change due to radiation exposure.

Another important neutron response is activation. By interacting with the reactor materials, the neutrons transmute the initial isotopes into other, often radioactive isotopes. Rather than affecting structural integrity, the induced activity in the material affects the radiation dose received by workers and equipment during the life of the reactor, the decay heat after shutdown of the reactor, and the waste disposal rating of the reactor materials when decommissioned. Since one of the roles of the structure during operation is to shield the magnets and other components from radiation it is desirable to have as little activation as possible. This is reinforced by the desire to minimise the dose to the workers and ensure the easy disposal of the materials at the end of a component's lifetime.

These effects are accentuated in a fusion energy systems since it has a harsher irradiation environment than fission energy systems of the same power. For a given power level, the total neutron population of a fusion reactor is about 4.5 times larger and the initial neutron energy is about 14 times larger.[†] Understanding these effects requires a large material database acquired in part from experiments on materials which have been irradiated in conditions similar to a fusion reactor. Existing fission and fusion neutron sources are not well suited to this purpose because their low power levels preclude irradiation to end-of-life conditions in a reasonable time. While a "Next Step" machine might provide appropriate conditions, design for the DEMO-type reactors has already begun and construction is expected to start during its operation, before a meaningful material database can be compiled.

A separate intense neutron source facility will be required to establish this database. To contribute the material database in the necessary time scale, the facility must:

- be based upon existing science and technology,
- simulate the radiation environment of a DT fusion reactor in both the magnitude and the characteristics of the neutron responses,
- produce damage rates at least as high as those expected in a DEMO-type reactor (approx. 20 DPA/full-power-year[fpy] in iron) in a volume of at least 500 cm^3,
- have sufficiently low neutron flux gradients that the response vary by less than 10% across a single probe,
- have quasi-continuous operation to prevent the annealing of point defects within the duty cycle of the pulsing, and
- provide testing at a variety of sample temperatures.

[†] For each 200 MeV of released energy, there are about 2.5 fission neutrons and about 11 fusion neutrons ($11/2.5 \approx 4.5$). Similarly, each fission neutron has about 1 MeV in comparison to the 14 MeV per fusion neutron.

Although not a specific requirement, it is implied that part of the 500 cm^3 volume will have damage rates much higher than the DEMO-relevant values, and thus allow for end-of-life damage levels (approx. 150 DPA) in a few years.

The Conceptual Design Activities [CDA] of the International Fusion Materials Irradiation Facility [IFMIF] concluded in December 1996 with a viable conceptual design meeting the above criteria. Two continuous-wave linear accelerators will each generate 125 mA of 40 MeV deuterons which will strike a flowing liquid lithium target, with every hundred incident deuterons producing approximately 7 neutrons with energies up to about 55 MeV. The facility is expected to begin operation within 8 years of the beginning of the engineering validation phase which follows sometime after the completion CDA. The development of IFMIF during the CDA phase was broken down into four major technical foci: project management and design integration, test facilities, target facilities, and accelerator facilities. The neutronics analyses of IFMIF are of particular interest to the test facilities group, whose task it is to design the test modules themselves, all their supporting structure, and the test cell as a whole. The IFMIF test facility will be divided into 4 regions as shown in figure 1.1: the high flux region defined by a damage rate higher than 20 DPA/fpy in iron, the medium flux region defined by a damage rate higher than 1 DPA/fpy, a low flux region with damage rates above 0.1 DPA/fpy, and a very low flux region outside that.

As shown in figure 1.2, three Vertical Test Assemblies (VTAs) will provide the support and cooling structure for the four different test regions. VTA1 will support the high flux test module, VTA2 will support the in-situ creep-fatigue testing module and/or the ceramic breeder tritium release module in the medium flux test region. Finally, the Vertical Irradiation Tube (VIT) system will be integrated into a third VTA to service the low and very-low flux test regions. As part of the CDA, both helium-cooled and NaK-cooled modules have been designed for the high and medium flux test regions.

Of all the calculations and analyses performed during the conceptual design phase, perhaps the most important is that of the neutron fluxes within the IFMIF test facility.[7] As the sole purpose of IFMIF is to simulate the neutron-irradiation environment of a DT fusion power reactor, the calculated neutron fluxes are one of the most significant parameters in assessing the viability of the design. In particular, the neutronic characteristics of the high flux test region distinguishes IFMIF from other irradiation facilities. As the design process transitions into an engineering design phase, the neutron flux calculations continue to play an important role. Not only will the structure of IFMIF itself be subjected to the same neutron flux raising the same questions of mechanical integrity, but the nuclear heat generation is necessary for designing an effective heat removal system and performing safety analyses. Finally, during operation the calculation of the neutron

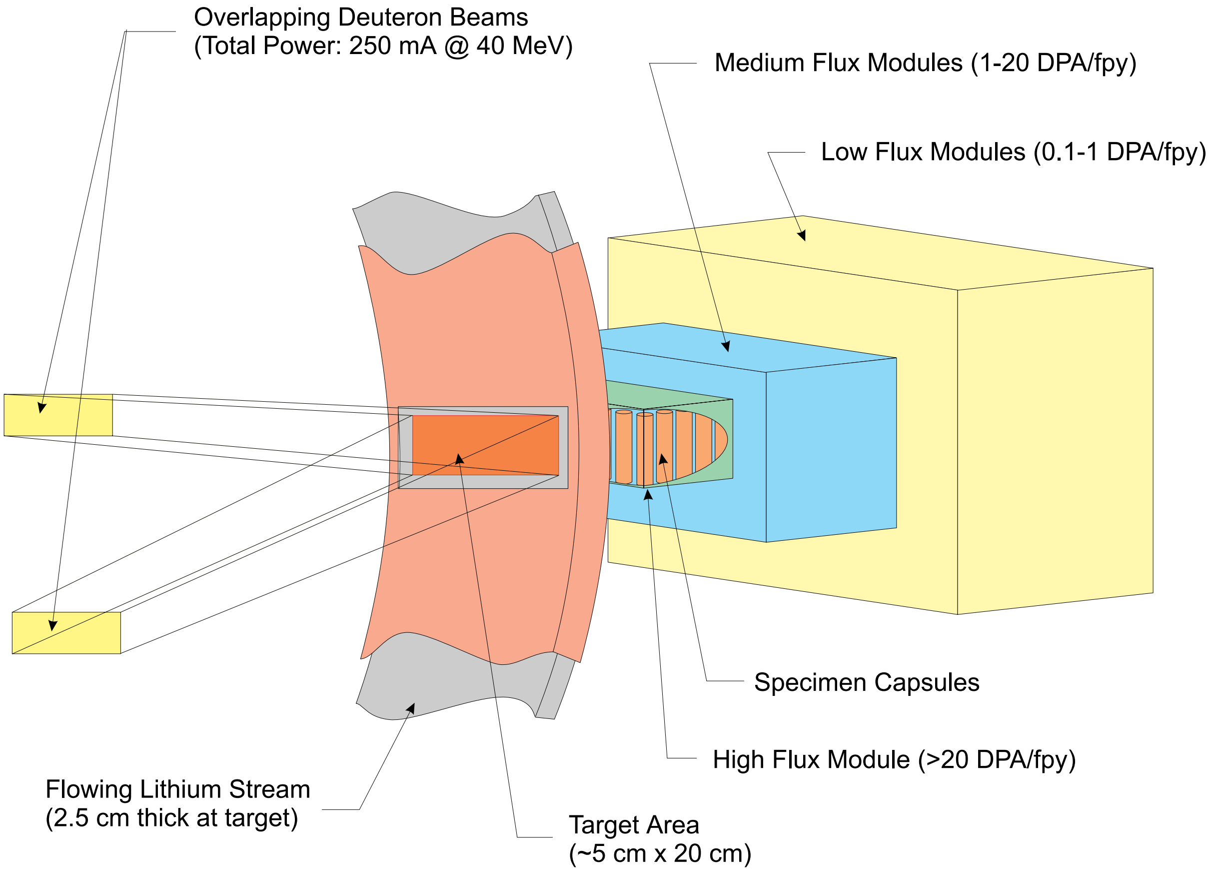

Figure 1.1: Schematic representation of IFMIF target and test modules.

flux spectra throughout the test facility will determine which position in the test facility should be used to achieve a certain effect.

Throughout this progression of design and operation phases, the detail and precision of the neutronics calculations become more and more complex. During the conceptual design phase it was sufficient to estimate the total volume of iron which would be exposed to a neutron flux generating 20 DPA/fpy and the gradients through such a volume. In the engineering design phase, however, it is necessary to calculate the neutron fluxes and responses in the detailed 3-dimensional test modules. Finally, during operation, it may be necessary to calculate the neutron flux, gradients and responses within a single miniaturised probe in one of the test modules. Such calculations necessitate a code system capable of producing these results in greater complexity as the design and operation requires it.

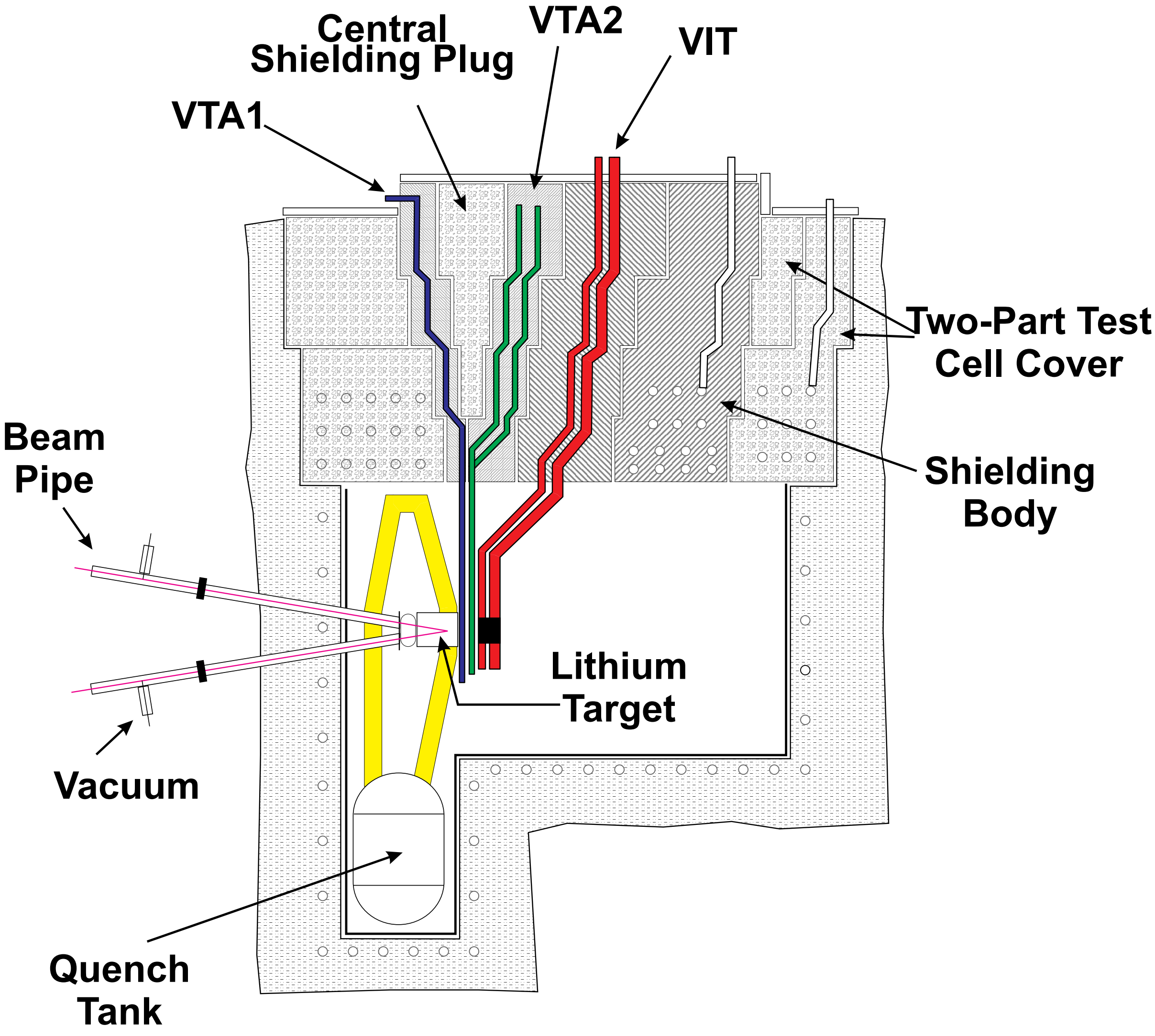

Figure 1.2: Test cell arrangement.

1.1 Goals of this Work

The goal of this work is to provide the basis for a thorough neutronics analysis of IFMIF's high flux test region and thereby contribute to the design and development of the IFMIF neutron source. Following the calculation of the neutron flux throughout the high flux test region and an analysis of its characteristics, specific primary and secondary engineering responses will be calculated. Analysis of these results will help determine the suitability of IFMIF as a simulation of a fusion irradiation environment and provide feedback to the various IFMIF design groups for improvements and optimisations with respect to the neutronics behaviour. Since the purpose of IFMIF is to perform neutron irradiation of material samples, a complete understanding of the neutron field and its responses is of the utmost importance.

One necessary step in achieving this goal is to develop a methodology and code system for performing such an analysis. A variety of computational tools and nuclear data will be necessary to perform an accurate neutronics analysis of the IFMIF test facility. Specific improvements and new developments will be necessary to ensure that the code system will be flexible and accurate enough for the future analyses. The most significant new development is the modelling of the Li(d,xn) neutron source term itself. If designed well, this code system can become a complete toolkit for the future analysis of IFMIF as its design is improved and refined. Furthermore, by carefully separating the generic components of the system from those that are specific to the IFMIF application, a general tool for the integrated neutronics analysis of other neutron sources can be developed.

Chapter 2 discusses the general requirements, available components, and generic developments for a neutronics code system. In chapter 3, the specific developments needed for modelling IFMIF are described with emphasis on all the aspects of the Li(d,xn) neutron source model. Using the primary result of the neutron flux, chapter 4 describes rudimentary testing of the code system through a thorough analysis of the neutron flux spectra and distribution.

Finally, in chapter 5, a complete volumetric analysis of the high flux region of IFMIF is presented, including specific detailed characterisations of some of the most important primary and secondary responses. The reference design of the High Flux Test Module is also analysed and its suitability as a simulation of a DT fusion environment is demonstrated. The impact of this analysis on the future requirements of the IFMIF neutronics development and the design of the test facility are discussed.

Chapter 2

General Code System Design and Integration

The first step in the development of any code system is to identify the tool and data requirements. Existing tools and data can be used directly, while others require further development. The first part of this chapter examines the general system requirements and identifies the existing components, followed by a description of new developments generic to any neutron source analysis. The specific developments necessary to apply this code system to IFMIF analysis are described in chapter 3.

Although the selection criteria used for the various components remain general, no code system can promise a turnkey solution for the analysis of all neutron source systems as the specific requirements of each must be considered. However, by separating the tasks which are certainly common to all analyses from those which are specific to each application, and choosing code system components which facilitate this separation, it is possible to design a code system which is applicable to the majority of neutron source applications.

The successful development of a code system requires an understanding of the general demands of each system component. Figure 2.1 shows a schematic representation for a code system with the global task of calculating the neutron responses of the system broken down into three functions: data processing, neutron transport, and post-processing. In addition, a number of input requirements have been identified: a description of both the neutron source and facility geometry and various neutron reaction cross-sections. Intermediate results within the system include neutron fluxes and cross-sections for neutron transport and engineering responses. Finally, the entire package needs to be integrated within some system capable of facilitating the flow of data amongst all the components and of delivering the final results in an easily usable form. Each of the three primary functions will be considered in turn, providing detailed analysis of the component selection, followed by a discussion of the system integration.

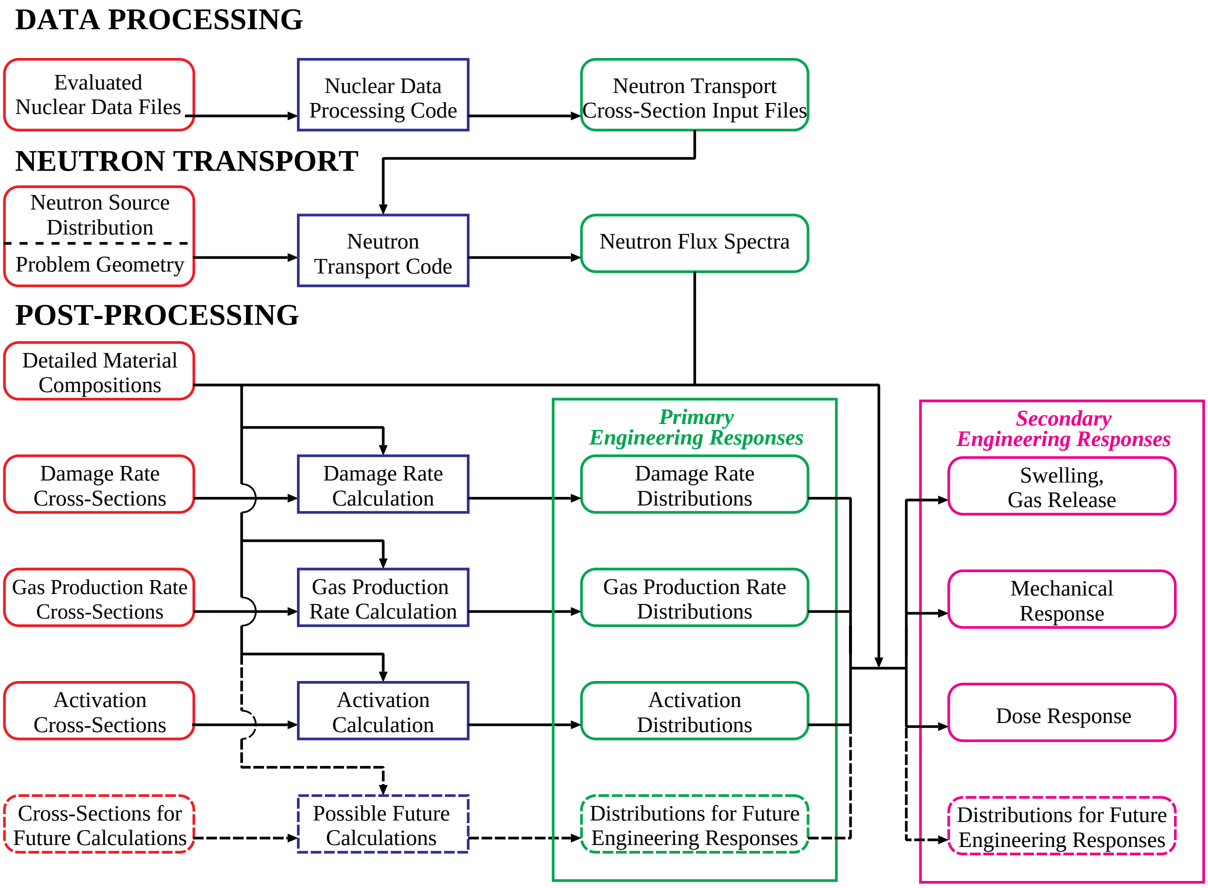

Figure 2.1: Flowchart describing code system functions.

2.1 Data and Data Processing Requirements

The primary requirement of any neutronics analysis code system is cross section information to describe the interactions of the neutrons with the material. Coupled to this is the need for a code to process this data from the formats in which they are freely available to those required by the other code system components.

There are many sources of nuclear data providing evaluated data files intended for many applications. Furthermore, as the evaluation and distribution of this data is a well-developed and internationally standardised activity, most of these choices conform to the same format description, and in some cases, even share the same data. These files include not only cross-section information for the transport of neutrons within materials, but also for the calculation of the effects of those neutrons, such as radiation induced damage, activation, or gas production. In the framework of a generic neutron source analysis code system, the selection of a particular data source is unreasonable. Every application will have specific characteristics, such as the energy domain of the neutron source, which affect the selection of the data source. The continual updating and improvement of these data files has a further impact on there appropriateness to a specific application.

Alternatively, it is necessary to determine a specific data format given its impact on subsequent decisions. The predominant format for nuclear data is the flexible ENDF-6[8] format, which allows many different types of nuclear data to be presented in a variety of sub-files for each isotope. The ENDF-6 format is well-documented and well-supported by both the providers of nuclear data and the various codes using this nuclear data. It is therefore only logical that the data for any generic code system for neutron source analysis also conform to this format.

The NJOY[9] nuclear data processing system has been specifically designed to process ENDF-6 formatted data, and is therefore an obvious choice to fulfill this role. The system consists of many modules each with a specific task, either reconstructing the physical cross-sections from the ENDF-6 data or converting the data to a particular data format. NJOY's flexibility and wide distribution have led to a symbiotic relationship with other neutronics programs such that most use one (or more) of the many formats NJOY can produce. This ensures that choosing NJOY does not introduce undue constraints on the selection of other code components.

2.2 Neutron Transport

Perhaps most important to any system for the neutronic analysis of a neutron source (equalled only by the existence of good nuclear data), is the accurate calculation of the neutron transport throughout the system. In general, this requires a code system component whose accuracy is not limited by the dimension or complexity of the energy domain or geometry of the problem. Since specific applications may have very different neutron source terms themselves, a further requirement is that the neutron transport component allow the accurate and flexible implementation of the source term.

Neutron transport codes are traditionally divided into two primary categories: Monte Carlo and deterministic. For a general code system, there are many advantages to the selection of a Monte Carlo code. Deterministic transport codes, such as those using the discrete ordinates method, generally require that the geometry be divided into a grid-like arrangement, a complicated task for complex geometries often leading to approximations. The neutron transport equation is then computationally solved using averaging approximations in space and energy. Instead, Monte Carlo codes describe each of the individual 3-dimensional domains of a problem by defining its bounding surfaces and statistically simulate the behaviour of individual neutrons at a microscopic level. The precision of the spatial and energy modelling is virtually arbitrary.

Deterministic methods typically give a solution throughout the phase space of the problem and, as a rule, their computational complexity (and hence the time required to solve a problem) scales exponentially with the number of dimensions and the precision of the geometrical grid. Monte Carlo methods, on the other hand, provide the results of specific user-defined tallies. The primary influence on the run-time is simply the number of particles which must be simulated to reduce the statistical error of the tally results. While the complexity of the geometry does play a general role, finely segmented geometries tend to decrease the area or volume in which a result is tallied, causing a corresponding decrease in the number of particles in that tally, and thus requiring a larger total number of particles. While this has been cited as an argument against Monte Carlo methods in the past, the wide-spread availability of high speed computing platforms and the ability to easily parallelise Monte Carlo applications makes this less poignant today.

MCNP[10] is an widely-used and well-supported Monte Carlo transport code with a long history in both the fission and fusion neutronics communities. In addition to the general advantages of Monte Carlo codes, MCNP's design permits the implementation of an arbitrary neutron source. When the various internal source descriptions are insufficient to accurately describe the neutron source, an entire code segment can be added with as much detail as required. An MCNP source routine, whether it is very simple or quite complicated internally, must only define a small set of initial parameters for the neutron, most importantly the location, energy and direction. As this routine must be used for each source particle, its efficiency affects the overall efficiency of the MCNP solution, representing the primary limitation. As will be seen later, this is an important advantage since the description of the neutron source as a closed form probability distribution or initial flux/current is not always possible.

2.3 Neutron Responses

Since the purpose of most neutron sources is to determine the effects of neutrons on materials, the calculation of these responses is also an important part of any generic code system. Many currently important neutron responses depend predominantly on the systems primary initial isotopes, the same ones which determine the neutron transport characteristics, and their calculation is a simple matter of multiplying the neutron flux by a neutron response cross-section. As a result, this role is adequately and fortuitously performed directly by MCNP. In particular, this is true for many of those responses related to the mechanical properties and structural integrity, such as the damage rate, measured by the number of displacements per atom, and the gas production.

Other responses often include both the direct and indirect influence of materials other than those primary materials which define the neutron transport characteristics. For example, the damage rate in alloys and composite materials depends specifically on the mixture of the isotopes in addition to the properties of the individual isotopes. Similarly, the activation of a system depends on the characteristics of isotopes non-existent in the original material, being produced by the neutrons themselves. Specific responses which have currently been identified and require extra processing tools are:

- induced activation,
- radiation damage in multi-species materials, and
- the cumulative distribution function of damage energy deposition, $W(T)$.

Figure 2.1 alludes to neutron responses which have not yet been identified, but may be significant in the future. While it is impossible to accommodate these unknowns directly, the ability to extend the code system to include them in the future is an important feature.

2.3.1 Radiation Induced Activation

As mentioned above, the activity calculations are based on all the various components of the initial material, including trace quantities, and on their reaction products. This requires a special code component capable of determining what isotopes are created by transmutation and decay during and after irradiation. There are many such activation codes in wide-spread use, particularly for fusion activation problems.[11–14] After comparing the features, methods and capabilities of these various codes, the most limiting factor for many is the number of reaction channels they can simulate. The number of actual reaction channels is a function of the energy domain of the system, with more channels opening in higher energy domains. Many activation codes rely internally on fixed coded tables of all the possible reactions. Since these codes were designed for use in the traditional energy range (below 20 MeV), the reaction tables usually exclude many of the reaction channels which exist in higher energy systems. Furthermore, these codes are usually based on the similarly restrictive ENDF-6 reaction numbers (MT numbers). To correctly use the new data, not only would the codes themselves require internal changes, but arbitrary reaction codes would have to be assigned outside of the ENDF-6 conventions. One exception to this is the activation code ALARA.[15] The data library structure of the ALARA activation code contains all the information about the reaction and does not depend on ENDF-6 MT numbers. Other features of ALARA include its ability to quickly and accurately solve the activation problem at a number of spatial points simultaneously and to accurately model intermittent or pulsed operation.

2.3.2 Radiation Damage Parameters

The basic process of radiation induced damage was described in chapter 1. The cross-sections used within MCNP to compute damage rates are calculation under the assumption that only one type of isotope exists in the material. This assumption is necessary to estimate the energy transfered from the PKA's to the other atoms, and therefore, determine how many displacements each PKA creates, on average. The presence, in large quantities, of other isotopes introduces a number of sources of error. Not only will the estimate of this energy transfer be incorrect, but the amount of energy to knock the each subsequent atom out of its lattice position may also be different. For this reason, special damage cross-sections need to be calculated which take into account both the individual parameters of the constituent nuclides and their mixture.

Characterisation of the induced damage is also important. While the displacements per atom provides a quantitative measure of the damage, it does not indicate the nature of this damage. One qualitative is the cumulative distribution function of the damage energy deposition, known as the $W(T)$ function. This distribution indicates the probability that damage will be caused by a PKA with energy less than T. This is related in the usual way to the probability density function, which indicates the probability that damage will be caused by a PKA with a specific energy. For a given material, this function is a type of spectrum with the PKA damage energy as its independent variable. Therefore, a special matrix operator must be calculated for use in transforming the neutron spectra into this $W(T)$ function.

The data used as input to the calculation of these cross-sections are available by processing the standard neutron transport data files with the NJOY program described in section 2.1. As an extra feature, the GROUPR module of NJOY can generate the PKA production matrices as a function of both the incoming neutron energy and the outgoing recoil energy. Also important are the other ions which may be emitted by the various neutron reactions, such as protons or alpha particles. The program damChar (see appendix C), based on SPECOMP,[16] has been written to calculate both the multi-species damage cross-sections and the $W(T)$ operator from the recoil spectra produced by NJOY. For each isotope in the mixture, the damage energy deposited by each type of recoil and charged particle is calculated using the polyatomic version of the Lindhard[17] energy partition model. The NRT[18] model then compares the damage energy to the displacement energy of the "‘target"’ isotope to calculate the number of displacements caused by a given recoil energy. A triple integration, twice over the number of isotopes (once as a target and once as a PKA) and once over the recoil energy domain, weighted by the isotopic fractions and the production spectra, respectively, gives the total displacement cross-section:

$$\sigma_D(E_n) = \sum_{i=1}^{N} f_i \sum_{j=1}^{N} f_j \int_{E_{d_j}}^{T_{max}} dT \left[P_i(E_n,T)\nu_j\left(L_d^{ij}(T)\right) + \sum_{x=1}^{M} P_x^i(E_n,T)\nu_j\left(L_d^{xj}(T)\right) \right] \quad (2.1)$$

where:

$N \equiv$ number of isotopes
$i, j \equiv$ isotope index $\in [1, N]$
$f_i \equiv$ isotopic fraction of i
$E_{d_j} \equiv$ displacement energy of j
$P_i(E_n, T) \equiv$ production matrix for recoil of type i
$L_d^{ij}(T) \equiv$ Lindhard damage energy for i in type j
$M \equiv$ number of charged particles
$x \equiv$ charged particle index $\in [1, M]$
$P_x^i(E_n, T) \equiv$ production matrix for charged particles of type x
$L_d^{xj}(T) \equiv$ Lindhard damage energy for x in type j
$\nu_j(L) \equiv$ # of displacements produced in j from ion with damage energy L

If the integration over the recoil energy domain is instead performed cumulatively for each recoil energy, the result is the the $W(T)$ transformation matrix. While this is valid for the damage created by PKA's impacting their own species, the inclusion of charged particles or multi-species damage terms affects its physical significance. If the damage contribution from alpha particles in iron, for example, this formulation would not account for the fact that due to the Lindhard energy partition model an alpha particle of energy T produces damage with very different characteristics from a PKA with the same energy. In order to solve this inconsistency, the damage can be characterised with the function $W(L_d)$ rather than $W(T)$. Although not as common as the $W(T)$ analysis, its physical meaning is similar. Furthermore, it does not misrepresent the importance of highest energy PKA's which should all create similar damage because of a saturation in the $L_d(T)$ function. Using this function to characterise the damage allows the meaningful inclusion of the charged particle damage as well as an approximation of the damage characteristics of multi-species materials.

$$W(E_n, L_d) = \sum_{i=1}^{N} f_i \sum_{j=1}^{N} f_j \int_{E_{d_j}}^{L_d} dL \left[P_i(E_n, T(L))\nu_j(L) + \sum_{x=1}^{M} P_x^i(E_n, T(L))\nu_j(L) \right] \quad (2.2)$$

where $P_i(E_n, T(L))$ is the same production matrix as in equation 2.1, but evaluated at a recoil energy found by inverting the Lindhard damage energy function, $L(T)$.

These data have the same limitations as the Lindhard and NRT models themselves, namely that they are less appropriate for lighter materials.[19] In addition, the weighted sum over the number of isotopes is also an approximation to a problem which otherwise requires the exact transport of all the recoils and charged particles.

The final step in both these calculations is simply the folding of the neutron flux vector with some cross-section operator, whether it be a vector in the case of total damage, or a matrix in the $W(L_d)$ case. This kind of multiplication can be generically expressed as a simple linear transformation of the flux results provided by MCNP. Many future responses can also be expected to require this kind of treatment, suggesting that it be a feature of an external program or of the system integration itself.

2.4 INACS: System Integration

System integration is necessary to facilitate the flow of data throughout this disjoint set of computer codes. At this point, four code components have been identified: NJOY, MCNP, ALARA and damChar. It is important to be able to use MCNP's neutron flux results as input to ALARA, to fold them with the results of damChar and to extract and interpret MCNP's other results. With this data handling as a primary function, an environment must be created where the user can easily extract the data they need from one stage to use as input for the next.

Other functions of such an environment include the ability to mathematically manipulate data, from simple scalar normalisation to transformations such as mentioned in section 2.3.2. Although not considered here, further extensions include graphical user interfaces and data visualisation, and their possible future implementation should be considered. All of these issues and considerations suggest that scripting language be used rather than a system programming language.[20]

The two most widely-used scripting language, Perl[21] and Tcl/Tk,[22] offer various important features such as simple extensibility and flexibility. In general, scripting languages are ideally suited to combining code components not necessarily designed to fit tightly together. Of these two languages, Perl has been chosen to create the Integrated Neutronics Analysis Code System [INACS] primarily because of its intrinsic support of object-oriented methods. These methods allow the creation of modular extensions where the user need not worry about how the data are manipulated, but rather, can request certain operations on the data through an easy to use interface. Thanks to their nature as interpreted and weakly-typed languages, the applications which combine and use these modules can be developed rapidly and evolve easily to handle new problems.

While it is true that new users to this system will have to be (or become) somewhat familiar with the Perl scripting language, the modules developed as part of INACS should make the tasks required within Perl quite straightforward.

This section will describe the development of an integrated neutronics analysis code system, or INACS, implemented as two primary Perl modules. The first, Mcplot.pm, provides a generic interface to the MCTAL files produced by MCNP, while the second, DataPath.pm, is an extensible interface to various output formats. Each specific output format is supported through a sub-module of DataPath.pm. Further information about the specific implementation of each module and related sub-modules can be found in Appendix B.

2.4.1 Mcplot.pm

The first task for the integrated system is to process and provide access to the tally results from MCNP. The MCNP program can itself be operated in the MCPLOT mode to process and plot these tally results, but it does not provide a truly flexible interface to manipulate these data in any way. Creating a Perl module by borrowing and extending some of the command syntax from MCPLOT, however, means that portion of INACS may already be familiar to many MCNP users.

The Mcplot.pm Perl module first reads and indexes the standard MCTAL output file, then, using the command syntax described in detail in appendix B.1, users can extract various subsets of the 8-dimensional tally results. Other INACS modules, as described below, will then be available to save these data sets in formats appropriate for the other components.

2.4.2 DataPath.pm

Since the volume of data can be very large (consider a 205 group neutron flux tallied at 5000 different spatial points), it is preferable to handle the data by reading directly from the MCTAL input file and into the required output file. Since this function is necessary for a number of different data output formats, the basic/generic user interface can be defined once and the functionality re-implemented by other sub-modules as they are created for each specific output type. The DataPath.pm module provides this base user interface and its functionality is implemented through a standard application program interface [API] to its sub-modules.

One of the DataPath.pm module's functions is to perform mathematical transformations on the data, from simple scalar normalisation to the application of cross-section operators. This, for example, allows calculations such as those described in section 2.3.2. The `scaleData()` method of the DataPath.pm module's interface facilitates this activity, allowing the user to define a scalar normalisation factor, a cross section vector, or a transformation matrix. The nature of this scaling operator will be automatically determined and used accordingly to modify the result.

Flux.pm and ALARA.pm

The Flux.pm module implements the DataPath.pm interface for extracting the neutron fluxes generated by MCNP from the MCTAL file for the purpose of viewing and/or plotting the fluxes. Up to eight fluxes can be saved in a file, with one column per flux and the flux energies given in the first column.

An extension of this module, ALARA.pm removes the 8 flux limit and ensures that the file conforms to ALARA's format requirements. Each flux is numbered sequentially and stored as a block with no information about the energy group structure.

Geom.pm

The analysis and visualisation of the data generated by MCNP is often complicated by difficulties in cross-referencing the tally results to spatial co-ordinates. While, in theory, it should be possible to calculate this from the well defined MCNP geometry information (e.g., calculating the centre of mass of a particular cell or surface where the tally is calculated), this function is not part of MCNP.

The Geom.pm sub-module implements the DataPath.pm interface to accomplish a partial automation of this task. Designed to directly extract tallies arranged on a regular geometry, it is possible to define the geometrical extents of a set of tallies, and the number of tallies in each dimension within those bounds. The tally information is then saved with this geometrical information and sorted in a user defined order based on the geometrical co-ordinates. In addition to implementation details, Appendix B.2.3 describes how this module may also be used for less regular geometries.

Sample implementations of the INACS integration package, used to facilitate the design neutronics calculations for IFMIF in the following chapters, are given in appendix B.2.4.

Chapter 3

IFMIF-Specific Code Design

Having described the general requirements, existing tools and generic developments in chapter 2, it is now necessary to describe those developments specific to the IFMIF system. The two most important aspects of the IFMIF neutronics analysis system are the necessity for intermediate energy data and the accurate modelling of the neutron source term from the Li(d,xn) reaction.

3.1 Data Requirements

The majority of the available nuclear data refered to in section 2.1 are limited to energies below 20 MeV.[23,24] In IFMIF, however, the accelerated deuterons will impact the lithium target with an energy of 40 MeV resulting in neutrons energies up to 55 MeV. As will be seen in chapter 5, the intermediate energy neutrons are not only a reality of IFMIF, but are essential for fulfilling its requirements. The availability of intermediate energy data for neutron transport calculations is therefore vital to the accurate modelling of the IFMIF facility. While some higher energy data and partial evaluations exist,[25] the data traditionally used for fission and/or fusion neutronics calculations are not sufficient and new data evaluations are necessary.

The significance of this intermediate energy data is primarily due to the various reaction channels with thresholds above 20 MeV. Figure 3.1(a) shows the cross-sections for the various neutron production reaction channels for ^{56}Fe. While in some cases, a channel may have a threshold below 20 MeV, its contribution to the total cross-section in the intermediate energy range may be much more significant. To perform calculations with the previously available data, various approximations have been made at energies above 20 MeV. The two most common approaches are: (a) to extrapolate the data linearly (or exponentially by a linear extrapolation in a log-log space), and (b) to assume a constant cross-section above 20 MeV.[26] While this may be appropriate (coincidentally) in some cases, the hydrogen production cross-section in ^{56}Fe shown in figure 3.1(b) demonstrates how wrong such approximations can be.

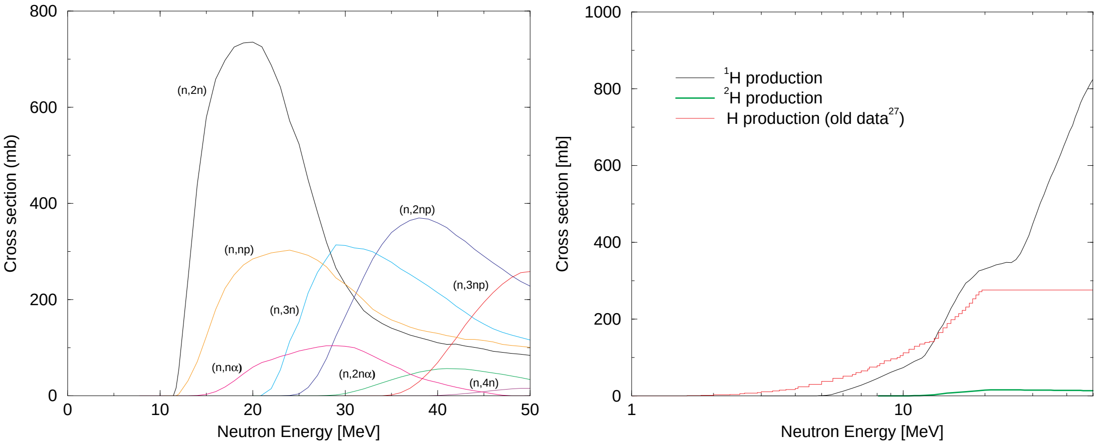

(a) Neutron producing reactions (b) Hydrogen producing reactions

Figure 3.1: Sample Cross sections for new ^{56}Fe data evaluation.

To fill this void, neutron transport data files have been evaluated in recent years by a variety of sources.[28,29] Due to their ENDF-6 format and their completeness, these data files meet the requirements described in chapter 2. Most importantly, they can be processed by NJOY to generate cross-sections for neutron transport, neutron-induced damage, nuclear heating, and gas production.

As complete as these data files are, however, they generally do not provide enough information to describe the cross-sections for the various neutron activation reaction channels. Additionally, since neutron transport calculations are dominated by the primary components of a material, effort has focused on complete and reliable transport files for a few important isotopes, rather than files for a wide range of isotopes. Activation calculations, on the other hand, are often influenced quite heavily by those components which exist in smaller quantities and their reaction products. For that reason, the activation data must be more complete, including as many isotopes as possible rather than just the main isotopes. For this reason, a collaboration between Forschungszentrum Karlsruhe and IPPE, Obninsk, Russia, was initiated within the framework of the IFMIF project to generate additional evaluated data files dedicated to activation at higher energies.[30] Due to the decades of effort devoted to the development of such data at lower energies, these data files simply adopt traditional data below 20 MeV, in this case version 4.1 of the European Activation File [EAF97][23] and provide new evaluations up to 150 MeV, all conforming to the ENDF-6 format.

Rather than just containing higher energy data for the same reaction channels, this data includes up to 170 reaction channels for many important structural material isotopes. Limitations on the ENDF-6 reaction codes (the MT numbers) prevent these reaction channels from being indexed in the same way as the other activation files, such as the European Activation File upon which the low energy portion is based. The ENDF-6 format allows an alternative method for describing this data, based directly on the target and product nuclei, rather than on the type of reaction which takes place. The intermediate energy activation files [IEAF] can be processed directly for use with ALARA.

3.2 Neutron Source Modelling

The most important new development required in the neutron transport area for IFMIF is an accurate model of the Li(d,xn) neutron source term. The ability of MCNP to employ an arbitrary source description will be fully exploited in the development of this source model. A complete description of each neutron in the MCNP calculation includes the initial energy and direction of the neutron as well as its initial location. In the IFMIF Li(d,xn) case, these parameters are determined by three different physical models. The energy and direction are determined entirely by the energy and angular distributions of the d-Li interaction. The initial location of the neutron is defined by the two other components: the deuteron beam intensity distribution defines two of the dimensions and the stopping power/range of the deuteron within the lithium target defines the third. For the latter component, the well known empirical model of Ziegler, *et al.*,[31] is used, and will not be further discussed here. Following a detailed discussion of the Li(d,xn) reaction model, there will be a description of the beam intensity model and a demonstration of the flexibility of the entire neutron source modelling package.

In developing a source model for the Li(d,xn) reaction, there are three possible routes: an analytical model based on the relevant reaction theories, a data file based on a full theoretical physics cross-section evaluation, or a data file based directly on the available experimental data.

While much experimental data have been published about the Li(d,xn) reaction,[32–35] there is not enough to directly create a complete cross-section data file. In particular, the neutron yield depends not only on the energy and angle of the emitted neutron, but also on the energy of the incoming deuteron. Very little data exist for 40 MeV deuterons as planned for IFMIF. Furthermore, most experiments are carried out at a fixed deuteron energy, and therefore give little information about the deuteron energy dependence of the cross-section. Recent experiments have attempted to measure the neutron yield from the Li(d,xn) reaction with 40 MeV deuterons, but the angular domain of the results is quite small and the results are not yet available.[36] This data provides a basis, however, for developing a description of the Li(d,xn) reaction based on theoretical reaction models.

In the field of nuclear physics, much is known about the various reaction mechanisms which are believed to be involved in the Li(d,xn) reaction.[37–40] The fact that lithium is such a light nucleus, however, means that many of the nuclear energy levels are resolved and a detailed treatment of each one must be carried out using all the tools of modern physics and quantum mechanics, including such techniques as distorted-wave Born analysis, R-matrix theory and consideration of pre-equilibrium reactions. To uses these models directly in the MCNP source routine, although theoretically possible, would be extremely inefficient. Recalling that this calculation must be performed once for each initial neutron, of which there may be up to 10 or 100 million, a complicated physical model would greatly slow down the solution. Instead, these models must be used to evaluate cross section information for the Li(d,xn) reaction which can then be used as the neutron source term. Such an extensive data evaluation is not within the scope of this work, but would certainly be valuable to the IFMIF project in the future.

The remaining alternative is to use approximate analytical representations of the reaction cross-sections to develop an engineering model. This has been done extensively in the past, most notably for a previous fusion materials irradiation facility study, FMIT.[41] Such models are usually based on two reaction components: the stripping reaction first described by Serber in 1947,[42] and a compound reaction component, traditionally described by a nuclear evaporation model. These two models are combined by adjusting the total cross-section of each to fit to experimental data.

3.2.1 Serber Stripping

The first description of the stripping reaction was offered by Robert Serber in 1947, following early experiments with high energy deuterons impinging upon a variety of targets. Serber's semi-classical development used data from both uranium and beryllium targets, but the theory itself is independent of the target nucleus. The basic principle of the theory is that the loosely bound deuteron impacts the nucleus directly, where one nucleon is trapped and the other continues free. With purely geometrical arguments, a classical development is used to determine the total cross-section for such reactions. Two limiting cases arise: the transparent case in which the nuclear radius, R, is assumed to be much smaller than the deuteron's radius, R_d, and the opaque case, in which $R \gg R_d$. The opaque case is somewhat more realistic requiring that the emitted nucleon remain outside the nuclear radius, while the transparent case allows the emitted nucleon to pass through the nucleus.

The derivation of angular and energy distributions begins quite simply with the wave function describing the neutron's position relative to the deuteron's centre of mass. A variety of Fourier transforms and the geometrical requirement for the opaque limiting case for neutron emission result in a probability distribution for the neutron's internal momentum relative to the deuteron's centre of mass. While very large momenta are possible, even if improbable, the probability distribution has a characteristic width related to the deuteron's binding energy, $\epsilon_b = 2.2$ MeV. From this point in Serber's development, there are two important steps which have often been misused in applications of the Serber stripping theory to the Li(d,xn) reaction in thick targets.

First, since the experiments upon which Serber based his development used 190 MeV deuterons, he made the valid assumption that the neutron's internal momentum would be very small when compared to the momentum of the centre of mass itself. Since he was using a thin target, there was no concern for the situation when the deuteron energy was of the same order of magnitude as the binding energy. This leads, in turn, to approximations for both the emitted angle and energy of the neutron. By considering the neutron's internal momentum, $\mathbf{p}$, in two components, one parallel to the deuteron's flight path, p_z, and one perpendicular to that flight path, $p_\perp$, we can define the angle and energy of emission of the neutron:

$$\begin{aligned} \sin\theta_n &\equiv \frac{p_\perp}{p_o + p_z} \\ E_n &\equiv \frac{1}{2M}\left[(p_o + p_z)^2 + p_\perp^2\right] \\ &= \frac{1}{2M}\left[p_o^2 + 2p_o p_z + p^2\right], \end{aligned} \tag{3.1}$$

where $p_o^2 = ME_d$ and M is the mass of the neutron and E_d is the kinetic energy of the deuteron. However, with the assumption that the internal momentum (and therefore any component of that momentum) is much smaller than the momentum of the centre of mass, these definitions become:

$$\begin{aligned} \sin\theta_n \approx \theta_n &\cong \frac{p_\perp}{p_o} \\ E_n &\cong \frac{1}{2M}\left[p_o^2 + 2p_o p_z\right]. \end{aligned} \tag{3.2}$$

In both cases, the error introduced by this assumption is of the order $p^2/p_o^2 = \epsilon_b/E_d$. For the energies in Serber's problem this is about 1%.

The second important step, and perhaps more subtle, is to derive angular and energy distributions from the probability distributions by integrating over either the parallel or perpendicular momentum, respectively. This is important first because the derivation of these distributions depends implicitly on the first assumption about the ratio between the energies. Second, it is important because these distributions should not be interpreted as the energy-independent angular dependence and angle-independent energy dependence of a double-differential cross-section. Using the probability distribution of the transparent case (for simplicity), and applying the assumption of large deuteron energy:

$$\begin{aligned} P(p) \cdot 2\pi p_\perp dp_\perp dp_z &= \frac{p_b}{\left(p_b^2 + p^2\right)^2} \cdot 2\pi p_\perp dp_\perp dp_z \\ &= \frac{p_b}{\left(p_b^2 + p_\perp^2 + p_z^2\right)^2} \cdot 2\pi p_\perp dp_\perp dp_z \\ &= \frac{p_b}{\left[p_b^2 + \theta^2 p_o^2 + \frac{M}{E_d}\left(E_n - E_d/2\right)^2\right]^2} \cdot 2\pi p_\perp dp_\perp dp_z, \end{aligned} \tag{3.3}$$

where $p_b^2 = M\epsilon_b$. It is clear that the angular distribution depends on the energy, and vice versa, even under the assumption of large deuteron kinetic energy.

Since Serber's initial work, the cross-section distributions for the more realistic opaque nucleus distributions have been used many times to explain and understand the thick target production of neutrons from the Li(d,xn) (and Be(d,xn)) reaction. As derived by Serber, these distributions are:

$$\frac{d\sigma}{d\Omega_\zeta} = \frac{RR_d}{\pi} \frac{1}{\left(1+\zeta^2\right)^{3/2}} \left\{1 - \left(1/2\zeta^3\right)\left[\left(1+\zeta^2\right)\tan^{-1}\zeta - \zeta\right]\right\} \tag{3.4}$$

$$\frac{d\sigma}{dE_n} = \frac{1}{4}\pi RR_d \frac{E_d\epsilon_b}{\left[\left(E_n - \frac{1}{2}E_d\right)^2 + E_d\epsilon_b\right]^{3/2}}, \tag{3.5}$$

where $\zeta = \theta/\theta_o = \theta\sqrt{E_d/\epsilon_b}$. In equation 3.4, the term in curly brackets is often assumed to be unity, particularly for large deuteron energies. Most applications, however, have considered neither the assumptions made by Serber in the development of these distributions nor the physical meaning of the distributions themselves. Instead a double differential cross-section has been formed simply by multiplying the energy and angular distribution derived by Serber and then used at energies all the way down to the threshold (between 6 and 10 MeV for lithium). In an often cited justification of the use of the Serber theory and Serber derived distributions to model a thick-target neutron yield, August, *et al.*,[43] compared experimental spectra to the results of Serber model in the forward direction only. The momentum distribution for the opaque nucleus in Serber's derivation is:

$$P(p) \cdot 2\pi p_\perp dp_\perp dp_z = \int_0^{2\pi} d\phi \frac{2\pi p_\perp dp_\perp dp_z}{\left(p_b^2 + p_\perp^2 + p_z^2\right)\left(p_b^2 + p_z^2 + p_\perp^2 \sin^2\phi\right)^{3/2}}. \tag{3.6}$$

By using Serber's assumptions to convert to angle and energy, and then setting the neutron angle to zero, the distribution in the forward direction should be proportional to

$$\frac{1}{\left[\left(E_n - \frac{1}{2}E_d\right)^2 + E_d\epsilon_b\right]^{5/2}}. \tag{3.7}$$

Instead, Serber's broader distribution, described by equation 3.5 is used. The theory is found to fit well at high energies, but to over-estimate the low energy neutrons. As a whole, however, it is concluded that the Serber theory is adequate to model the neutron yield in the forward direction from thick targets.

Using this work as a justification for the application of the Serber theory to thick targets while modelling the Li(d,xn) reaction for the FMIT project, great effort was expended to fit this model to a large base of experimental data.[41] With a passing reference to the validity of the Serber theory at low deuteron energies, another angular distribution term is included as a (somewhat arbitrary) correction for low energies. The fitting was carried out first for the total angular yield, a valid application of Serber's distributions. As expected, this other correction term dominates at low deuteron energies. Furthermore, after fitting the angular distributions, the double-differential cross-section is once again formed by simply multiplying by the angle-independent energy distribution derived by Serber.

These methods were employed in order to find a mathematical representation for the Li(d,xn) stripping reaction in terms of the angle and energy. The simplicity of the distributions, however, depends very strongly on the assumption that the deuteron's kinetic energy be sufficiently high. Without this assumption and its results, closed-form distributions would be much harder to derive and the independence of the angular and energy distributions harder to justify. However, since Monte Carlo programs are based on the sampling of probability distributions, it is just as easy for the source routine to sample the momentum distribution directly as it is to sample a double-differential cross-section.

The probability distribution of the momenta in the opaque nucleus limiting case is:

$$P(p) \cdot dp_x dp_y dp_z = \frac{\hbar}{8\pi^2} \frac{p_b}{P^3 \left(p_x^2 + P^2\right)} \cdot dp_x dp_y dp_z, \tag{3.8}$$

where $P^2 \equiv p_b^2 + p_y^2 + p_z^2$ and the x-direction is perpendicular to the surface of the nucleus. Note that this differs from the transparent nucleus case. The distribution is not uniform in all three directions due to the condition that the neutron must miss the nucleus and the proton impact it. If $p_{\perp_x}$ is the momentum in the y-z plane ($p_{\perp_x}^2 \equiv p_y^2 + p_z^2$), then we can integrate over all the possible values of p_x to get:

$$\begin{aligned} P(p_{\perp_x}) \cdot 2\pi p_{\perp_x} dp_{\perp_x} &= \int_{-\infty}^{\infty} \frac{\hbar}{8\pi^2} \frac{p_b dp_x}{P^3 \left(p_x^2 + P^2\right)} \cdot 2\pi p_{\perp_x} dp_{\perp_x} \\ &= \frac{\hbar}{4\pi} \frac{p_b}{P^3} \int_{-\infty}^{\infty} \frac{dp_x}{\left(p_x^2 + P^2\right)} \cdot p_{\perp_x} dp_{\perp_x} \\ &= \frac{\hbar}{4\pi} \frac{p_b}{P^3} \frac{\pi}{P} \cdot p_{\perp_x} dp_{\perp_x} \\ &= \frac{\hbar}{4} \frac{p_b}{\left(p_b^2 + p_{\perp_x}^2\right)^2} \cdot p_{\perp_x} dp_{\perp_x}. \end{aligned} \tag{3.9}$$

Since both this distribution and equation 3.8 are analytically integrable and their integrals are analytically invertible, we can now follow standard Monte Carlo sampling methods to calculate the momenta of any particular neutron:

1. directly sample $p_{\perp_x}$ using the distribution of equation 3.9
2. sample $\theta_{\perp_x}$ uniformly on $[0, 2\pi]$ to calculate $p_y = p_{\perp_x} cos\theta$ and $p_z = p_{\perp_x} sin\theta$
3. **using the value for** $p_{\perp_x}$, and equation 3.8, directly sample p_x.

At this point not only have there been no assumptions as to the relative magnitude of the deuteron's kinetic energy, but by using the sampled value of $p_{\perp_x}$ as a parameter for sampling p_x, there have also been no assumptions about the independence of the angular and energy distributions.

It now remains to transform this momentum vector, defined in a co-ordinate system with the x-direction normal to the nuclear surface, into the macroscopic co-ordinate system of the target. Since it is equally probable that this reaction occurs at any place on the nuclear surface, the angle of interaction, ϕ, can be found by uniformly sampling on the interval $[0, 2\pi]$. This is the angle in the xy-plane between the local y-axis of the reaction and the global y-axis of the laboratory frame of reference.

In this transformation, it is also possible to add the physical effect of the coulomb repulsion between the deuteron and the nucleus, an effect ignored in most models because, once again, at high deuteron energies, it is negligible. The deflection angle deflection due to the coulomb repulsion between the nucleus and a passing deuteron can be derived as $sin\theta_c = E_c/2E_d$, where $E_c = Ze^2/4\pi\epsilon_o R$ is the coulomb barrier energy. Important to the derivation of this angle, however, is that the deuteron maintains its charge throughout the interaction. In the neutron stripping case, the coulomb repulsion is only in effect for the first half of the interaction, and therefore, the angle of deflection is $sin\theta_c = E_c/4E_d$. With the z-direction defined by the original direction of the deuterons, this is the angle in the xz-plane between the local z-axis of the reaction and the global z-axis of the laboratory frame of reference.

The two angles, ϕ and θ_c, are used to transform the vector $\mathbf{p}$ into the laboratory co-ordinate system. It is then trivial to calculate the direction vector (normalise $\mathbf{p}$) and the energy (the magnitude of $\mathbf{p}$) of the neutron as input for the Monte Carlo transport calculation.

Although this model is semi-classical, it can produce neutrons which have an energy higher than the kinetic energy of the incoming deuteron. While this is possible in this Li(d,xn) reaction, these exothermic neutrons are not modelled properly by the Serber stripping theory. In this implementation if the neutron's energy is higher than the deuteron energy it is rejected and another one is created.

3.2.2 Compound Reactions

Competing with direct reaction processes are the processes of compound reactions. In these reaction channels, the deuteron is temporarily absorbed by the target lithium nucleus forming a beryllium compound nucleus in an excited state. In the decay from many of these excited states, neutron emission is possible.

When there are enough nucleons in the compound nucleus, and therefore its internal energy levels are sufficiently dense, all of these compound reactions can be well described by a statistical model such as the evaporation model. In this model, nucleon emission is considered analogous to the evaporation of a single water molecule. A full development of this theory results in a neutron emission probability naturally isotropic in angle and with the following energy distribution:

$$\frac{d\sigma}{dE_n} \propto E_n e^{-E_n/T}, \tag{3.10}$$

with a statistical temperature, $T \propto \sqrt{E^*/A}$, for an excitation energy, E^*, in the compound nucleus of mass A.

Most previous attempts to simulate the Li(d,xn) reaction have used this standard evaporation model in addition to the Serber stripping model to fully describe the reaction process.[41,44] With only 9 nucleons, however, such statistical models are perhaps outside their domain of validity. The binding energies of the deuteron and lithium-7 nucleus result in a compound nucleus in an excited state of about 16.7 MeV plus the kinetic energy of the deuteron. The level density, however, is not sufficient to treat the resulting neutron decay statistically, and each possible level should be individually modelled and analysed. The search for better models invariably leads directly to the most intricate models which are more likely to be used in a complete nuclear physical evaluation of the cross-section, as referred to above.

Since this leaves only the somewhat poorly suited evaporation model, returning to its first principles allows modifications which improve its applicability to this reaction. The first of these modifications is to reevaluate the relationship between the excitation of the energy of the compound nucleus and the statistical temperature. The relationship indicated in equation 3.10 above is based on a number of thermodynamics considerations derived primarily from the assumption that the excitation energy is lower than a critical value of roughly $9A^{1/3}$ MeV.[45] The nucleons should therefore be considered as a highly degenerate "gas". Given that the ^{9}Be compound nucleus formed by combining ^{7}Li with a deuteron at rest has an excitation of about 16.7 MeV and a critical energy of $9 \cdot 9^{1/3} = 18.7$ MeV, the compound nucleus resulting from faster deuterons will almost always be above this critical energy. The nucleus need not, therefore, be treated as a degenerate gas, but rather, a linear relationship between the excitation energy and the statistical temperature can be assumed.

It is still necessary to determine a proportionality constant between this statistical temperature and the excitation energy, with a logical choice being the inverse of the number of nucleons, 9. That is, the statistical temperature is simply found by dividing the excitation energy equally amongst all the nucleons of the compound nucleus.

Following the derivation of this theory (see [45, pp. 367]) and using a statistical temperature of $T = E/A$, the level density is:

$$S(E^* - E_n) = A \cdot \ln(E^* - E_n) + c,$$

which gives an energy distribution:

$$P(E_n)dE_n = E_n(E^* - E_n)^A. \tag{3.11}$$

While this change does slightly improve the compound nucleus reaction channel modelling, there is still a significant low energy peak in the forward direction of most experimental results which is not yet included. This is the purpose of the second modification of the standard evaporation theory: the introduction of a linear model limited to low energies. This model was first recommended during analysis of the FMIT facility as an approximation to all succeeding evaporations, those occurring from the still excited nucleus following the first evaporation. The form of this model is:

$$P(E_n)dE_n = E^* - m_2 E_n, \tag{3.12}$$

for neutron energies below E^*/m_2, and 0 otherwise. Once again, a logical choice is to assume the remaining excitation energy is uniformly distributed among the remaining 8 nucleons, and therefore, a value of $m_2 = 8$ has been chosen.

The implementation of this model directly samples the neutron energy of a primary evaporation using equation 3.11 and an angle isotropically distributed on [0,π]. These values are transformed to the laboratory frame of reference and used as the initial parameters of the neutron.

Since MCNP's source function method only allows one neutron to be described, the treatment of subsequent evaporations must be implemented carefully. Before converting to the laboratory reference frame, the excitation energy of the primary evaporation's residual nucleus is calculated and used to determine if a subsequent evaporation also takes place, with the probability being proportional to the square of the residual excitation energy. If a subsequent evaporation is determined to take place, the deuteron energy and neutron energy are stored for use when the subsequent evaporation is forced for the next MCNP asks for a source particle. When the source particle is requested, the stored information is retrieved and used to sample distribution 3.12.

3.2.3 Fitting to Experimental Results

The last step in creating the Li(d,xn) reaction model is to fit these two models to neutron yield data from various experiments using each model's remaining free parameters.

Serber's stripping theory leads to the derivation of a purely geometrical constant cross-section of $\sigma_{strip} = 50A^{1/3}\mathrm{mb} = 97\mathrm{mb}$ for ^{7}Li, with a threshold of $2(R/R_d)\epsilon_b \simeq 3A^{1/3} = 5.7$ MeV. While this cross section is a normalization constant for the probability distribution integrated over an infinite domain, the rejection of exothermic neutrons by this implementation of the stripping model corresponds to a finite domain. Therefore, it is impossible to use this cross section directly as a fitting parameter. In the thin targets bombarded by Serber, nearly all the reactions occurred at the very high 190 MeV energy, resulting in only about 14% of the neutrons with energies higher than the incoming deuteron. In the IFMIF problem the neutrons are produced throughout the thick target from deuterons with energies from the 40 MeV initial energy all the way down to the threshold of about 6 MeV. At these energies, 31% to 64% of the neutrons, respectively, are generated at energies above the incoming deuteron energy. The fitting parameter, therefore, must be somewhere between 36 and 69% of the nominal cross section as determined from the Serber theory.

The Serber stripping model will be fit to the experimental data with a lower energy threshold of 6 MeV and an initial guess of $\sigma_{strip} = 97$ mb/2 = 48.5 mb. Since the stripping component heavily dominates the forward directed yield at energies above 5 MeV, the stripping cross-section can easily be determined by comparing the model and the yield in the forward direction.

For the compound nucleus reactions, a two-part total cross-section is assumed: a $1/v$-shaped part at lower energies and a linear part at higher energies. The transition between these two shapes is determined by an upper energy limit, E_{max}, at which the total cross-section vanishes. By requiring that both the cross-section and its first derivative be continuous at the transition, it can be shown that the transition occurs at $E_{max}/3$. Including the coulomb threshold as a lower energy limit the final form is:

$$\sigma_{comp}(E_d) = \sigma_{comp_o} \cdot \begin{cases} \frac{1}{\sqrt{E_d}} & E_d \in [E_c, E_{max}/3], \\ \frac{3}{2}\sqrt{\frac{3}{E_{max}}}\left(1 - \frac{E_d}{E_{max}}\right) & E_d \in [E_{max}/3, E_{max}]. \end{cases} \tag{3.13}$$

As mentioned above, the probability that a neutron is produced by a subsequent evaporation is proportional to the square of the residual excitation energy. In addition to being normalised by the square of the maximum possible excitation energy, $E_{max} + Q$, there is a fitting parameter used to scale the distribution for a rejection sampling, f_{comp_s}.

The primary data set is a direct measurement of the angular spectral neutron yield performed by Dr. Sugimoto of JAERI.[46] Although there is a lack of published information about the details of this experiment, it is a complete measurement of the neutron yield from 32 MeV deuterons bombarding a thick target with full spectral data up to 56 MeV at 17 angles between 0 and 140 degrees. The parameters which result from a fit to this data set will be refered to as set 'S'.

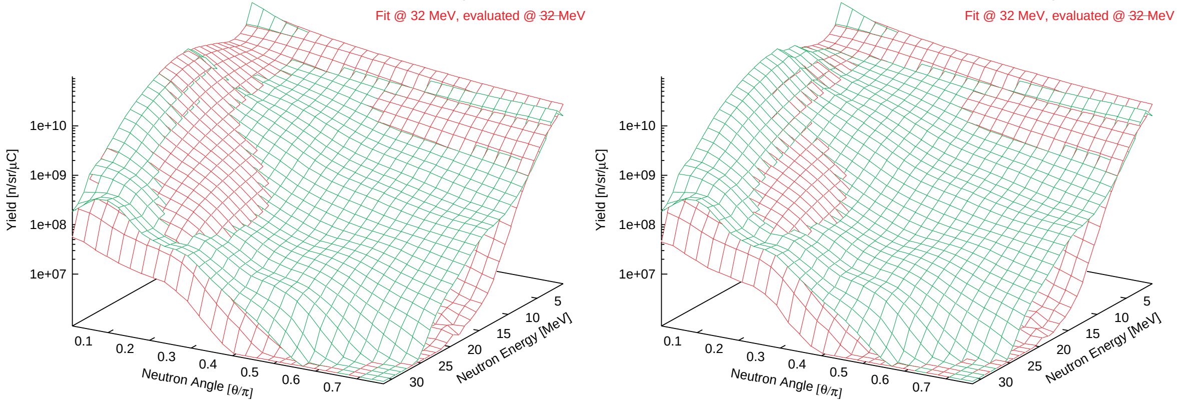

(a) Fit set S (b) Fit set F

Figure 3.2: Comparison of model with Sugimoto experimental data set.

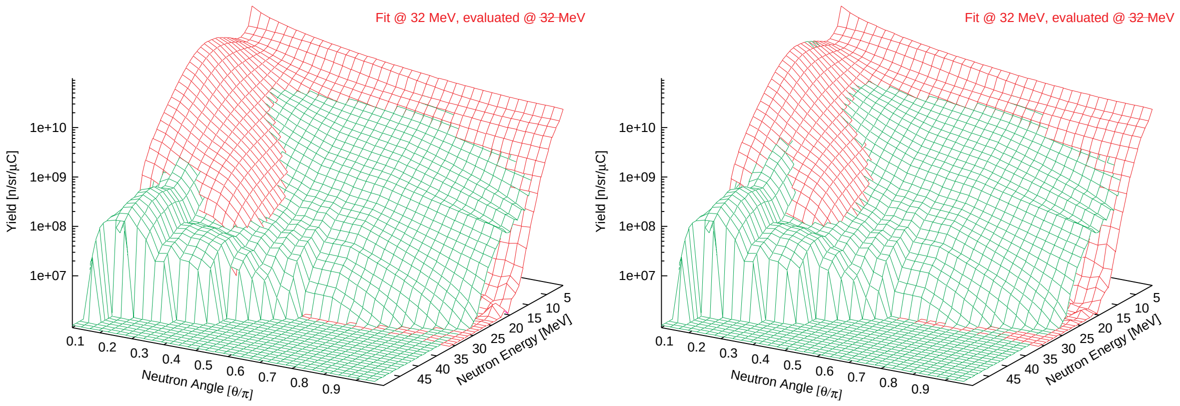

(a) Fit set S (b) Fit set F

Figure 3.3: Comparison of model with FMIT model data set at 32 MeV.

As a secondary data set, the results of Mann, *et al.*,[47] will be used. They fit these and other models to a large array of experimental data during the FMIT development. The experiments used in this fitting exercise each used a variety of initial deuteron energies and measured the neutron yield spectrum at a variety of different emission angles, but none was as complete as the above-mentioned data set from Sugimoto. Differences between the stripping model used in this fitting exercise and the one developed in this work have already been described. Furthermore, the fitting process was purely mathematical, using physical models as the fitting functions, but not constraining the fitting parameters to be physically consistent. In this work, however, the fitting parameters will be total reaction cross-sections which are both consistent with the models themselves and more physically realistic. The parameters which result from a fit to this data set will be refered to as set 'F'.

A computationally robust fitting of the models to the experimental data is hampered by a number of factors. The mathematical form of the Serber stripping model as a neutron momentum probability distribution cannot be transformed to a traditional cross section to be used as a fitting function. The effect of the transformation between the center-of-mass and laboratory reference frames in the compound reaction model combined with the effect of the subsequent evaporation sub-model make this similarly inappropriate. Finally, the desire to ensure that the final source model is physical realistic leads to a graphical fitting process.

After fitting the stripping parameter using higher energy portion of the forward-directed yield, the compound reaction parameters were fit graphically by comparison to the full 2-dimensional domain. An initial guess of 15 MeV was used for E_{max}, as suggested by Oyama,[44] and the other parameters were fit with the main purpose of matching the low energy forward-directed peak and the backward-directed spectral yield.

The results of fitting the four available parameters of this model, σ_{strip}, σ_{comp_o}, f_{comp_s}, and E_{max}, are shown in figures 3.2 through 3.4, and the values of the parameters are shown in table 3.1.

Data Set	Fitting Parameters				Total Neutron Yields			
					Model		Data	
	σ_{strip}	σ_{comp_o}	f_{comp_s}	E_{max}	32 MeV	40 MeV	32 MeV	40 MeV
S (Sugimoto)	48.5 mb	1.25	1.75	15 MeV	6.3%	7.2%	6.4%	N/A
F (FMIT)	40 mb	1.25	1.75	15 MeV	6.0%	6.7%	4.9%	7.0%

Table 3.1: Model fitting parameters for two data sets.

Due the Serber stripping model's clear dominance in the forward direction, it is the easiest model to fit to the experimental data and the initial guess of 48.5 mb is a very good fit to the Sugimoto data. On the other hand, because the compound reaction model is a gross approximation to the actual process, choosing correct values for its parameters is more complicated and uncertain. In particular, when comparing the yield to Sugimoto at 140° (0.77π), in figure 3.2(a), it is clear that the evaporation processes of this model do not fully describe this angular region. However, comparing the same region in figure

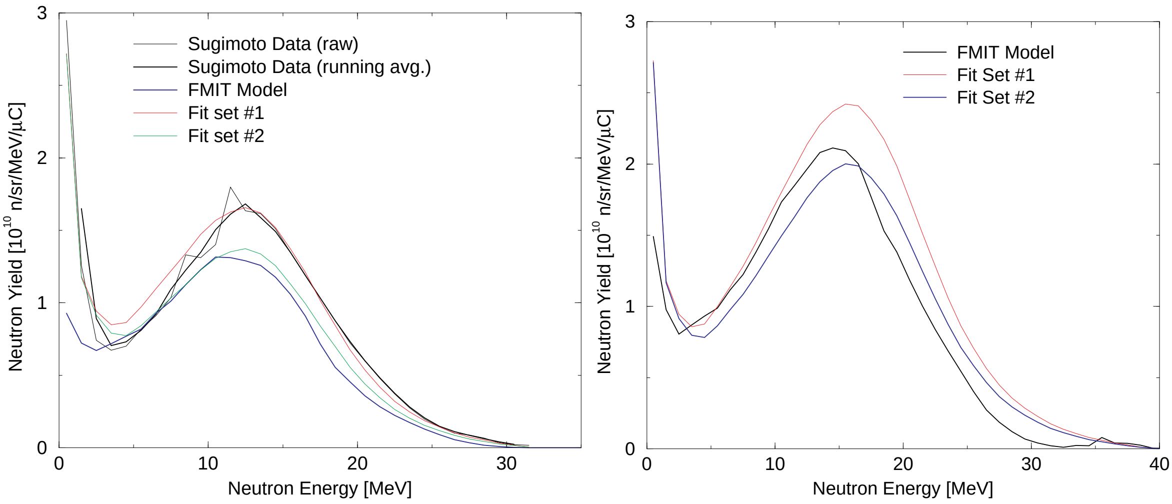

(a) 32 MeV (b) 40 MeV

Figure 3.4: Comparison of model with data sets in forward direction.

3.5(a), it is evident that the contribution to the total yield from this region is very small. The same can be seen of the exothermic region in the forward direction.

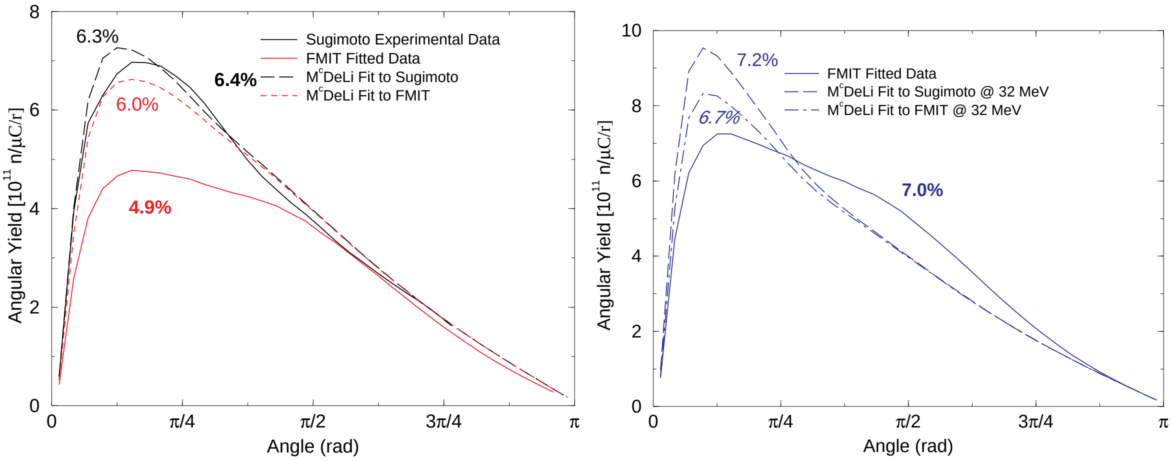

(a) Evaluated at 32 MeV (b) Evaluated at 40 MeV

Figure 3.5: Angular distributions of data sets and model. All parameters were determined by fitting at 32 MeV.

When comparing this model to the FMIT model, a number of features are apparent. First, the low energy component modelled by the subsequent evaporations is very different. This can be explained by both the purely mathematical fitting of the models in the FMIT case combined with a number of approximations made at low energies. Since most of the experiments used in the FMIT fitting exercise had minimum neutron detection energies of at least 1 MeV, the data were extrapolated to include information down to a neutron energy of 0 MeV. Using this corrected data, a mathematical fit was performed for the angular yield, which was then simply multiplied by the energy distributions. As noted in the above discussion of the Serber stripping treatment, this assumes that the energy and angular distributions are independent of each other. This is clearly not the case for compound reactions in which an interdependence is explicitly introduced during the transformation from the centre-of-mass reference frame to the laboratory reference frame.

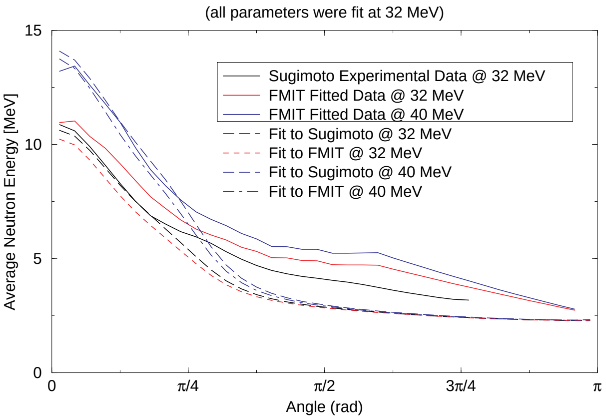

Figure 3.6: Average neutron energy of data sets and model.

The validity of these fits can be further examined with some somewhat independent measures: the total yield, the total yield's angular distribution, and the average neutron energy's angular distribution. The Sugimoto data set, when extrapolated to 180°, has a yield of 6.4% (0.064 neutrons are produced per incident deuteron) for 32 MeV deuterons. The total yields for the FMIT data at 32 MeV and 40 MeV are 4.85% and 7.02%, respectively. Table 3.1 shows the total model yields for the two parameter sets. Figure 3.5 shows the comparison of the angular yield distributions of the model to those of the experimental data sets, while Figure 3.6 shows the same comparison for the angular distributions of the average neutron energy.

Comparing the various results of the FMIT data set at 32 and 40 MeV, it is apparent that this data includes a major contribution from compound reactions at these higher energies. Since deuterons with energy higher than 15 MeV do not contribute to the compound reaction channel in the new model, the increase of 0.7% in the FMIT fitting parameter set's total yields is due entirely to the stripping component. Since the stripping component of the new model fits reasonably with that of the FMIT data (see figure 3.4) the additional 1.5% difference in the FMIT data's total yields must be due to the compound reaction model of that data. This is confirmed by the comparing the angular yield distributions in figure 3.5, in which the FMIT data results exhibit an increase in the yield through a large angular domain. Alternatively, the effect of the increased maximum deuteron energy on the new model's results is isolated to angles less than approximately $\pi/4$. The purely mathematical fitting, the low energy extrapolation of the experimental data upon which it was based, and the introduction of a second angular distribution for the stripping reaction all contribute to this physically unrealistic effect in the FMIT data.

3.2.4 Shortcomings and Uncertainties

Even after these adjustments and modifications there are some obvious shortcomings.

First, there are other possible direct reactions which could contribute to the neutron production. Most importantly, the possibility of the disintegration of the loosely bound deuteron due entirely to the long-range electric forces between it and the nucleus was described by Dancoff in the paper immediately following Serber's in 1947.[48] However, as Dancoff himself notes, this reaction will only be "experimentally prominent" for large values of Z.

Second, the ^{7}Li(d,n)^{8}Be reaction is exothermic with a Q-value of 15.02 MeV. While this value is included intrinsically in the excitation energy, E^*, of the compound nucleus reactions, it is not possible to account for it in the Serber stripping theory. To accurately model the yield from these exothermic reaction modes would, once again, require the implementation of detailed modern physical models. Therefore, the kinetic energy of the neutron is restricted to that of the incoming deuteron. Since experimental data show this represents a very small fraction of the yield, this should be of little concern.

Above all, it is clear from the two data sets used to fit the data that the yield from the Li(d,xn) reaction includes a great deal of uncertainty. This uncertainty will be somewhat quantified in chapter 5 by comparing the neutron response results for both sets of fitting parameters. While the two parameter sets found here may be useful for early conceptual design calculations, a full evaluation of the Li(d,xn) reaction must be performed to further reduce the uncertainty and improve the reliability of the neutronics calculations for the detailed design and operation.

3.2.5 Deuteron Beam Intensity

While the depth of the Li(d,xn) reaction within the lithium target is determined by the model for the range of deuterons in lithium, the location of the interaction in the other two directions is determined by the distribution of the deuterons as they impact the target. The beam intensity distribution model is based on calculations which have been performed within the accelerator design group to describe the high energy beam transport characteristics.[49]

Initial results indicated that a relatively flat beam with edge effects on the order of 5% would be achievable with existing technology. As a result, the beam has been modelled with a uniform distribution for the purpose of IFMIF conceptual design activities. However, more recent calculations have shown that the beam intensity at the target will be much less uniform and spread over a larger area, as shown in red in figure 3.7. The concentration in the edge peaks and the spread over a larger footprint is expected to result in a generally reduced average flux and local "hot-spots", necessitating a non-uniform beam model.

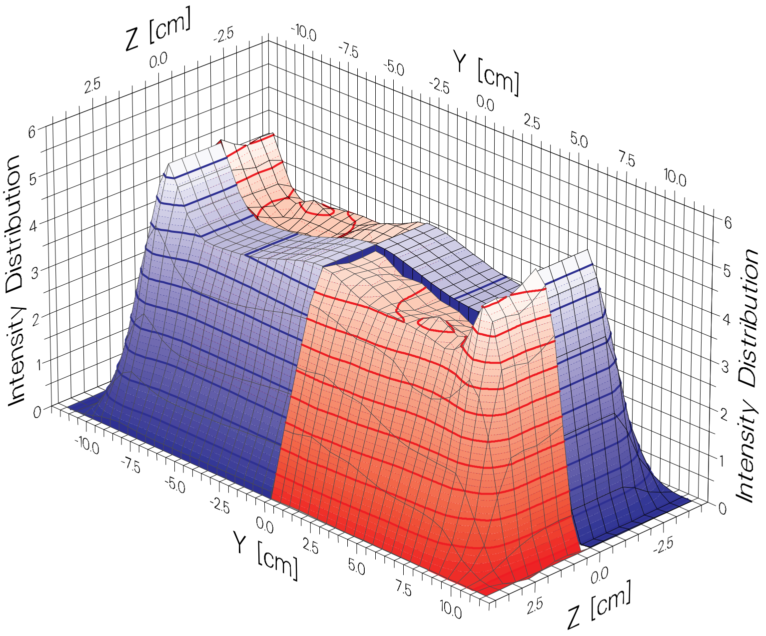

Figure 3.7: Comparison of model with calculated beam distribution.

The beam distribution was assumed to be separable in the two directions, y and z, transverse to the beam propagation. In each direction the beam profile is modelled by the sum of three functions based on the normalised Gaussian distribution:

$$G(y, y_o, \sigma) = \frac{1}{\sqrt{2\pi\sigma}} e^{-(y-y_o)^2/2\sigma}. \tag{3.14}$$

The basic function in each direction is a flat distribution with Gaussian edges defined as:

$$\begin{aligned} I_{y,b}(y, y_o, \sigma_o, m_o) =& m_o \left[G(y, -y_o, \sigma_o) \cdot H(y + y_o) + G(y, y_o, \sigma_o) \cdot H(y - y_o) \right] \\ & + G(0, 0, \sigma_o) \left[H(y + y_o) - H(y - y_o) \right], \end{aligned} \tag{3.15}$$

where y_o is the width of the flat portion, σ_o the width of the Gaussian edges, and m_o is restricted to 1 or 0, depending on whether or not the distribution has Gaussian edges.

To this base function, two correction terms may be applied, each with the form:

$$I_{y,c_i}(y, y_{c_i}, \sigma_{c_i}, m_{c_i}) = m_{c_i}\left[G(y, -y_{c_i}, \sigma_{c_i}) + G(y, y_{c_i}, \sigma_{c_i})\right]. \qquad (3.16)$$

For each correction term, $i = 1, 2$, if y_{c_i} is non-zero, the form will be a symmetric pair of Gaussian distributions, centred on $\pm y_{c_i}$ with width σ_{c_i} and height m_{c_i}. Alternatively, corrections with $y_{c_i} = 0$ will simply take the form of a central Gaussian with width σ_{c_i} and height $2m_{c_i}$. An example is shown in figure 3.8.

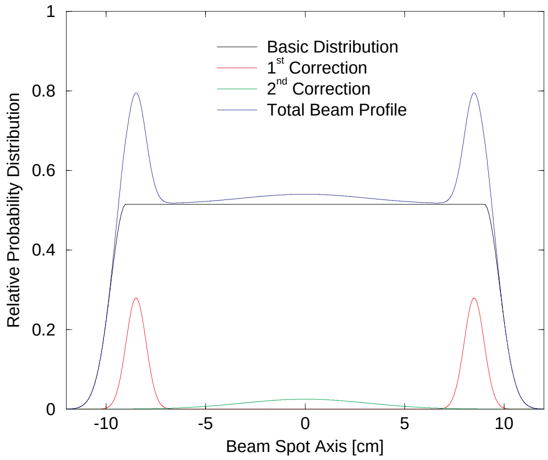

Figure 3.8: Sample of beam distribution modelled with Gaussian functions.

Beam fitting parameters			IFMIF values		
y_o	σ_{y_o}	m_{y_o}	9	0.6	1
y_1	σ_{y_1}	m_{y_1}	8.5	0.45	0.3
y_2	σ_{y_2}	m_{y_2}	0	5	0.2
z_o	σ_{z_o}	m_{z_o}	2	0.6	1
z_1	σ_{z_1}	m_{z_1}	0	0	0
z_2	σ_{z_2}	m_{z_2}	0	0	0

Table 3.2: Fitting parameters for IFMIF deuteron beam distribution.

The choice of this model is based on both the physics of the system and the mathematical requirements of the Monte Carlo model. Since the physical distributions are related to Gaussian distributions, this type of model permits relatively good agreement with the edge effects and general shapes of the real distributions. Furthermore, well-known and efficient methods exist to sample a Gaussian distribution, not the case for a polynomial of arbitrary order which might be used to fit the data more accurately.

Using the parameters shown in table 3.2, figure 3.7 shows a 3-dimensional representation of this IFMIF beam intensity distribution model. The blue quadrants show the results of the model and the red quadrants show the original data. Since only the relative intensity is important for this implementation (the absolute intensity is simply a measure of the total beam current), the units of figure 3.7 are arbitrary. The model's parameters could be further improved if the high energy beam transport calculation were performed on a finer mesh.

3.2.6 The $\mathsf{M^cDeLi}$ Neutron Source Modelling Package

These various models have been implemented together as a library of FORTRAN-77 subprograms known as the Monte Carlo Deuteron Lithium [$\mathsf{M^cDeLi}$] source module. The main interface to this module is through a subroutine written with the MCNP standard source routine interface as defined by the MCNP4B manual.[10]

As the IFMIF facility is still in the conceptual design stages, it is important that this model offer enough flexibility in both the geometrical description and the beam parameter definition to accommodate any possible changes to the beam and target design. For example, in previous Li(d,xn) based irradiation facility designs and early considerations for IFMIF,[50] one of the many options was the use of multiple beam and target arrangements. To accommodate both small and large changes in the design, $\mathsf{M^cDeLi}$ uses a variety of scalar and vector input parameters to define each beam and target. Most importantly, however, $\mathsf{M^cDeLi}$ can be used to model an arbitrary number of beams and targets arranged in arbitrary geometrical configurations. Additionally, the beam profile model allows a wide variety of profiles to be modelled, including rectangular uniform and central gaussian profiles.

Including the 6 vectors used to describe the beam intensity profile, each beam requires 12 input parameters to be fully defined and each target requires 3, as illustrated in figure 3.9 (see also appendix A). It is also important to note that there need not be an equal number of beams and targets. In fact, in the current IFMIF design, there are 2 beams impinging on a single target.

Three of the beam parameters are simply scalar variables describing the beam current and energy, and which target the beam is incident upon. Three more beam parameters are true vectors representing the direction and orientation of the beam and the position of the centre of the beam spot on the target in the global co-ordinate system of the problem. The beam orientation vector simply defines which direction, in the plane normal to the beam direction, should be used in the modelling of the beam intensity distribution. The final 6 parameters are vectors in the (x, σ, m) phase space of the beam intensity model, defining the three model components for each direction.

Of the three parameters which describe the targets, two are scalars defining the target's density and relating the target to an MCNP cell definition. The final parameter is a vector which defines the normal of the target in the global co-ordinate system.

The accuracy and efficiency of this set of input parameters is based on a loose set of assumptions about the beam-target arrangement. All of these assumptions are related to reasonable physical requirements of the system. Most notably, the target's dimensions are assumed to be larger than the volume in which the beam's energy is deposited. Since no target dimensions are defined in the $\mathsf{M^cDeLi}$ input, the calculated neutron birthplace

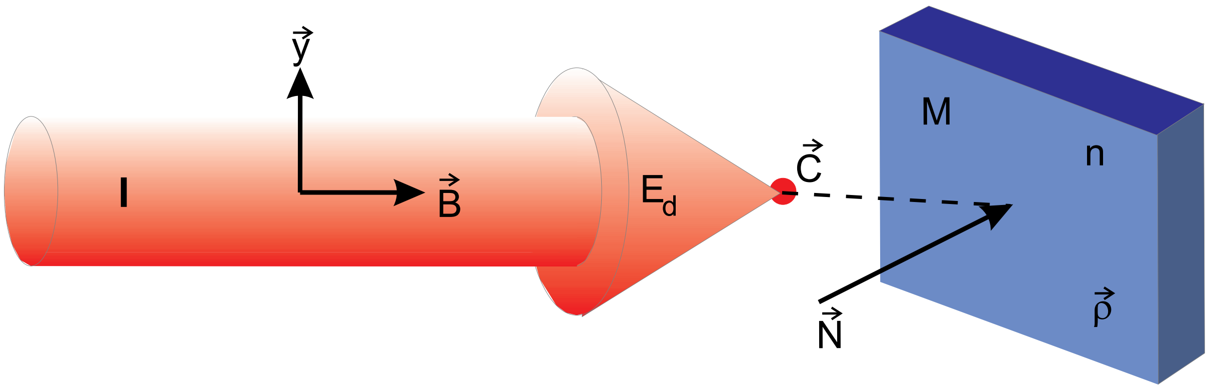

Beam Parameters		Target Parameters	
n	target number	M	MCNP cell number
$\vec{B}$	beam direction vector		
$\vec{y}$	beam orientation vector	$\vec{N}$	target surface normal vector
$\vec{C}$	beam spot centre		
I	beam current [mA]	ρ	target density [g/cm^3]
E_d	beam energy [MeV]		

Figure 3.9: Parameters used to describe beams and targets in M^{c}DeLi. They are described in more detail in appendix A

is not implicitly restricted to the domain inside the target. Instead, once a location is calculated, it is checked to ensure that it is inside the cell which defines the target in the MCNP geometry. If this is not the case, the neutron will be rejected and a new birthplace will be sampled. Each rejected neutron represents an inefficiency in the sampling routine. It is therefore up to the user to ensure that the beam and target definitions are consistent with each other. Since the real system will also require that the beam's energy be deposited in the target, this requirement simply means that the model should be a realistic representation of the physical system.

Other primary assumptions of the M^{c}DeLi module are that the beam is symmetric and separable in the two transverse directions. In general, due to the complicated distributions generated by the high-order magnetic fields of the accelerator, neither of these assumptions will be true. On the other hand, for various engineering reasons it is desirable that the beam approach both of these assumptions as improvements in the design and technology of accelerators are realized. Finally, it is important that the beam direction not be parallel to the surface of the target, a logical assumption since if this was the case, no deuterons would impact the target, resulting in no neutron production.

Chapter 4

IFMIF Neutron Flux: Testing and Analysis

The neutron flux distribution is the fundamental result of any neutronics analysis as all the other neutron responses are derived from it. This chapter will focus on an analysis of the neutron flux's spatial distribution in IFMIF. Understanding the details of the flux distribution throughout the high flux test region will facilitate a deeper understanding of the other neutron responses. Characteristics such as the total flux, the high energy flux ($E_n > 14\ MeV$), and the ratio between them provide important links between the neutron source and the neutron responses.

Through an analysis and understanding of the features of this neutron flux it is also possible to subject the code system, and particularly its new developments, to a number of simple tests for self-consistency and basic physical validity. By comparing the results of an MCNP calculation in an empty (vacuum) test cell to those of a simple deterministic neutron streaming program, INS,[51] it is possible to partially validate the M^{c}DeLi neutron source module and its integration with MCNP. Following this, the self-consistency of the neutron transport data can be tested by performing neutron transport calculations on a loaded test cell and comparing these results to the unloaded case. Finally, using the neutron flux results from a loaded test facility, activation calculations can be performed to demonstrate the necessity for, and completeness of, the intermediate energy activation data.

The only way to truly and completely validate the data and tools used for neutronics calculations is by benchmarking them against well designed experiments. While some experiments are currently underway to provide data for this kind of benchmarking, other testing methods must be explored for the time being.[36]

4.1 Problem Definition and Data Representation

A standard MCNP problem definition has been used for all detailed characterisations and comparisons in this work. Using all the components described in chapter 3, a geometry was defined in order to calculate detailed results in three dimensions. The geometry consisted of an $8.25 \times 23.5 \times 10.5$ cm^3 volume representing the high flux region of IFMIF. The results were calculated in one quadrant of this volume using volume track-length tallies (type 4) in each of the $0.5 \times 0.5 \times 0.5$ cm^3 cells/segments. Additional surface track-length estimators (type 2) were used on the $x = 0$ surface to give a complete set of results on the domain $([0, 8.0], [0.0, 11.5], [0.0, 5.0])$. In problems where this region was loaded with material, ^{56}Fe was used at 50% of the theoretical density to represent a helium cooled test module.

This volume was intentionally chosen to be larger than the reference High Flux Test Module [HFTM] which has dimensions $5 \times 20 \times 5$ cm^3. In cases where the high flux region is loaded, this serves not to model the HFTM exactly, but rather, to demonstrate the responses in a larger available volume. The relatively small extra volume of material will have a small, although measurable, effect on the final neutron transport results. Results of final calculations using the reference HFTM geometry itself will be shown in chapter 5 to better provide a comparison to DT fusion conditions. All MCNP calculations were performed with at least 50 million source neutrons.

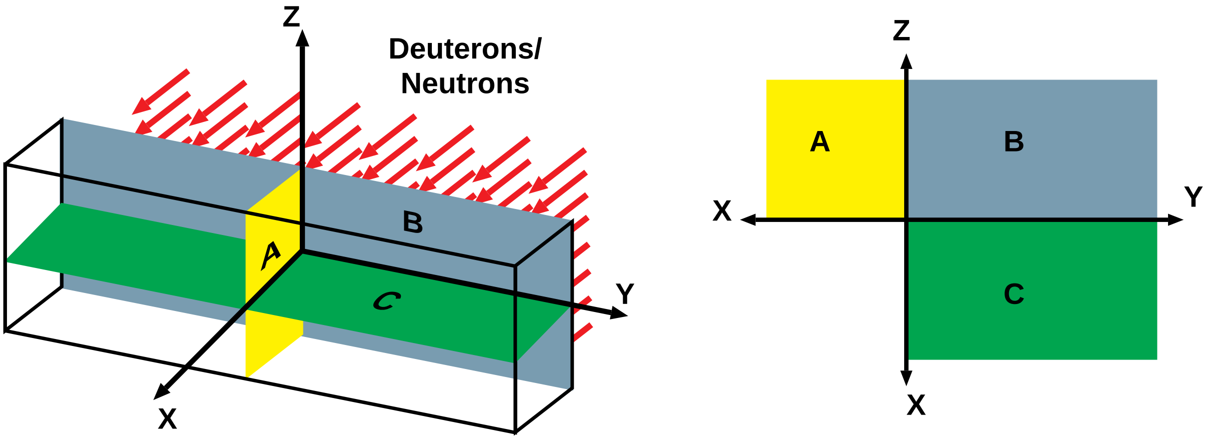

Figure 4.1: Explanation of detailed data representation.

It can be a challenge to visualise this large set of three-dimensional data in a meaningful manner. In general, two-dimensional contour plots only show the results on a single plane while three-dimensional isosurfaces only show the results at a single value. In order to include as much information as possible, a compromise has been chosen to represent the data in this work. As explained in figure 4.1, three important planes, $x = 0$, $y = 0$

and $z = 0$, were chosen to represent the data. The first of these represents the conditions at the lithium target backplate, while the other two are symmetry planes within the high flux test region. Unfolding these three planes into a single two-dimensional diagram allows an understanding of both the detailed quantitative results and the general shape throughout the volume. This is only valid if the data change smoothly, which is the case in these analyses. This representation will be used for many of the results in this and the following chapter.

4.2 MCNP-M^{c}DeLi Testing

During the early conceptual design of IFMIF, the INS program was written to help select a beam-target configuration. While this program only performs deterministic neutron streaming through a void volume, rather than neutron transport through material, it does provide results with which the MCNP-M^{c}DeLi results can be compared. Although most MCNP results in this work will be generated with the Sugimoto parameter set ('set S'), this section will show results generated with the FMIT parameter set ('set F') since the INS program is based on the FMIT data set.

The INS program was developed to quickly and simply model the spatially dependent uncollided neutron flux in the test region of an accelerator driven neutron source. The target is discretised spatially to account for the dependence of the Li(d,xn) cross section on both the deuteron energy and the beam intensity distribution. For each chosen point in space, the contribution from each of these target regions is calculated using simple $1/r^2$ attenuation, and the total flux calculated by integrating over all the target regions. The INS code uses the rough evaluated data file from the FMIT project as cross section data to determine the neutron source. The INS program also has a slightly different beam intensity distribution model. For comparison with the MCNP-M^{c}DeLi calculation, the spectrum was calculated by INS at each of the same points described in section 4.1. In this case the MCNP results were calculated using an empty test region, so as to also calculate a neutron streaming solution.

The value of such a comparison is a final test of the MCNP-M^{c}DeLi tool's ability to model the neutron source. The INS code's simplicity prevents it from being used for more detailed calculations, but the results should be very similar for this equivalent MCNP problem. Any differences which do exist in either the neutron spectra or the spatial flux distribution should be primarily a consequence of the differences between the M^{c}DeLi model and the FMIT data set itself.

Figure 4.3 shows the neutron flux's spatial distribution for both the INS and the MCNP-M^{c}DeLi tools. Similarly, figures 4.4 and 4.5 show comparisons of the fast flux (flux with energy greater than 14 MeV) and the fraction of the flux with this greater energy, respectively.

4.2.1 Features of Uncollided Neutron Flux

Before making any comparisons, it is instructive to analyse the features of the uncollided neutron flux distribution arising from this neutron source. The most obvious feature in figures 4.3 through 4.5 is the effect of the deuteron beam intensity distribution, directly responsible for the flux distribution on the backplate. In addition to the hot-spot near $y = 8.5$ cm caused by the beam peaks, the rapidly decreasing beam intensity causes large gradients along the y-axis for $y > 8.5$ cm.

The spatial distribution of the total flux away from the backplate can be explained by two geometrical considerations. In addition to the geometrical attenuation expected when moving away from a finite source, there is also a strong influence from the Li(d,xn) source's angle-energy distribution. The total flux has a total attenuation of about 65% between $x = 0$ and $x = 6$ cm along the x-axis. The fast flux, on the other hand, has an attenuation of only 37% along this same distance. This difference is reflected in the fast flux's increasing importance in the direction away from the target, from less than 18% at the backplate to more than 30% near $x = 7$ cm.

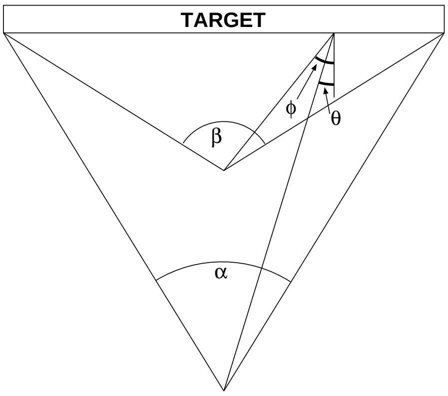

Figure 4.2: Dependence of angle subtended by target on the distance from the target.

The difference in this level of attenuation is essentially due to the difference between the total flux's angular distribution and that of the fast flux. Considering a finite sized target, as described in figure 4.2. Moving away from the target reduces the solid angle subtended by the target at that point ($\alpha < \beta$), corresponding to a decrease in the original angle of each initial contribution ($\theta < \phi$). Since the majority of the fast flux is due to small angle contributions, it is less affected. Put another way, since the neutrons' average energy increases for smaller angles (see figure 3.6), the average energy of the neutron flux increases in the direction away from the target.

The angle-energy distribution of the neutron source combines with the deuteron beam distribution to have a significant effect on the fast flux and the fast flux fraction. The gradients along the y-axis are much higher for the fast flux because the large angle contributions from the nearby peak dominate the direct contributions from that point of the target. Due to the angular distribution of the source's average energy, these large angle

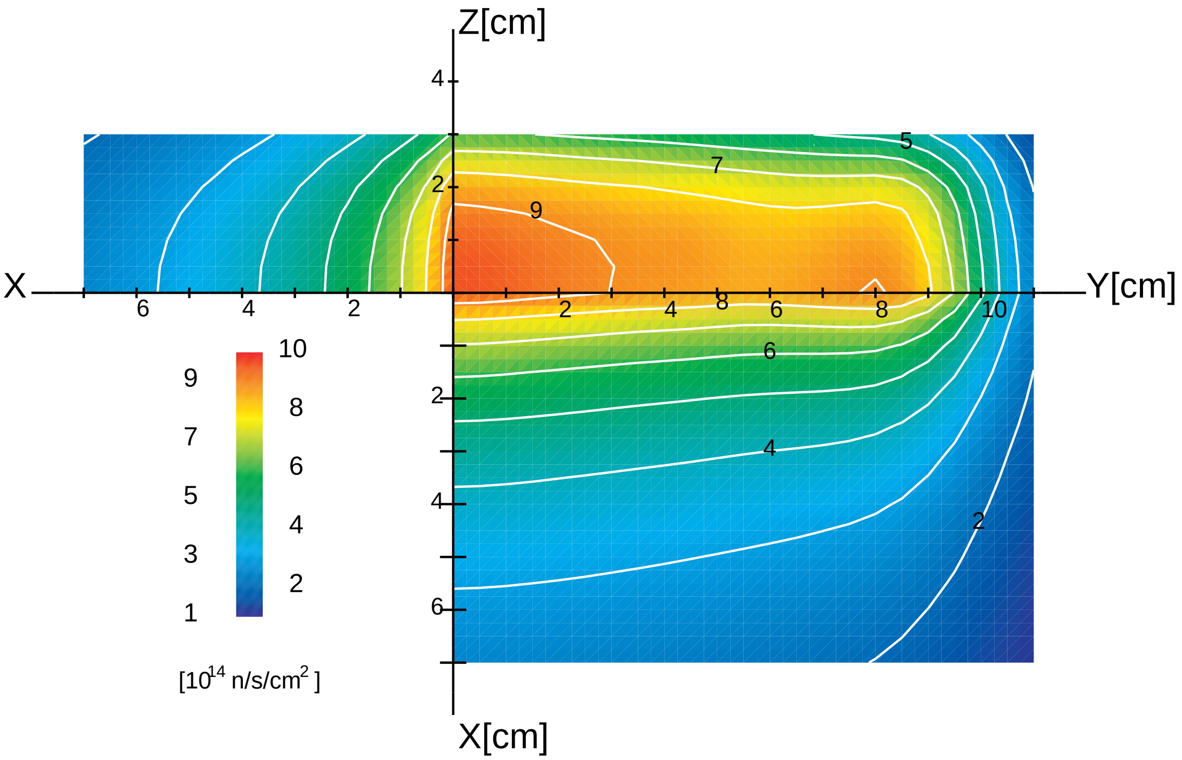

(a) INS

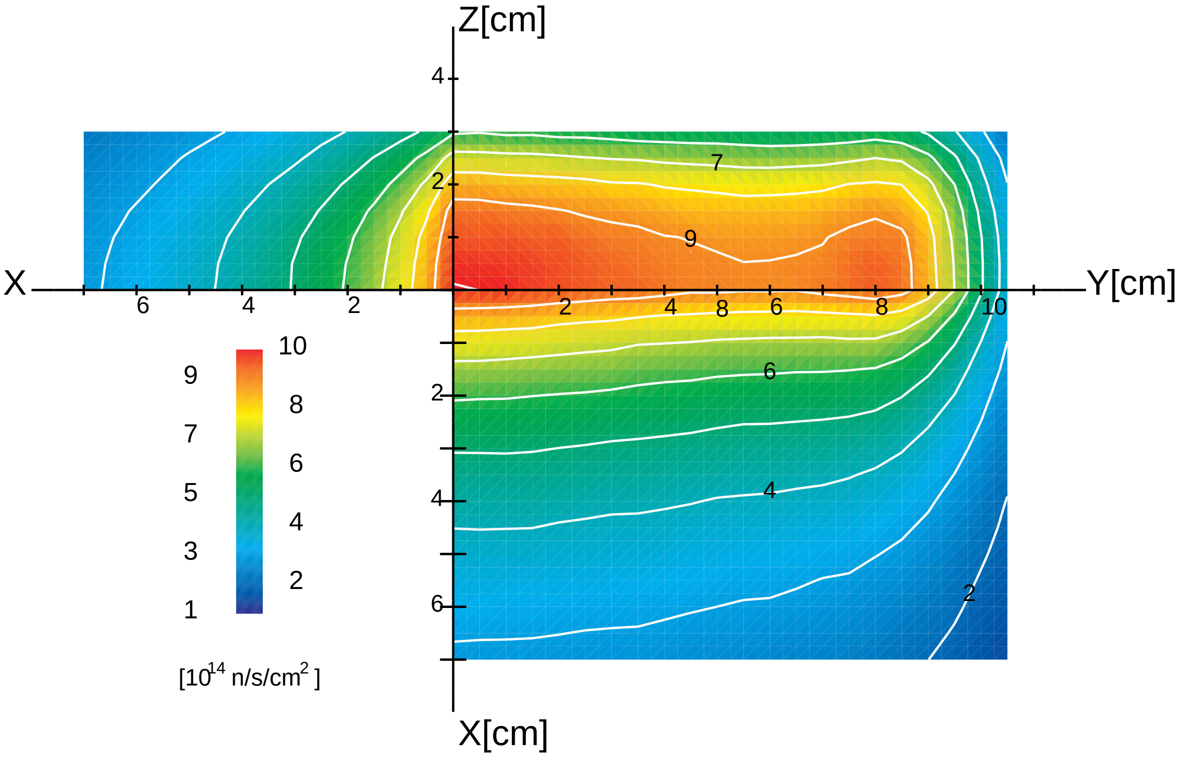

(b) MCNP

Figure 4.3: Total neutron flux in void test region.

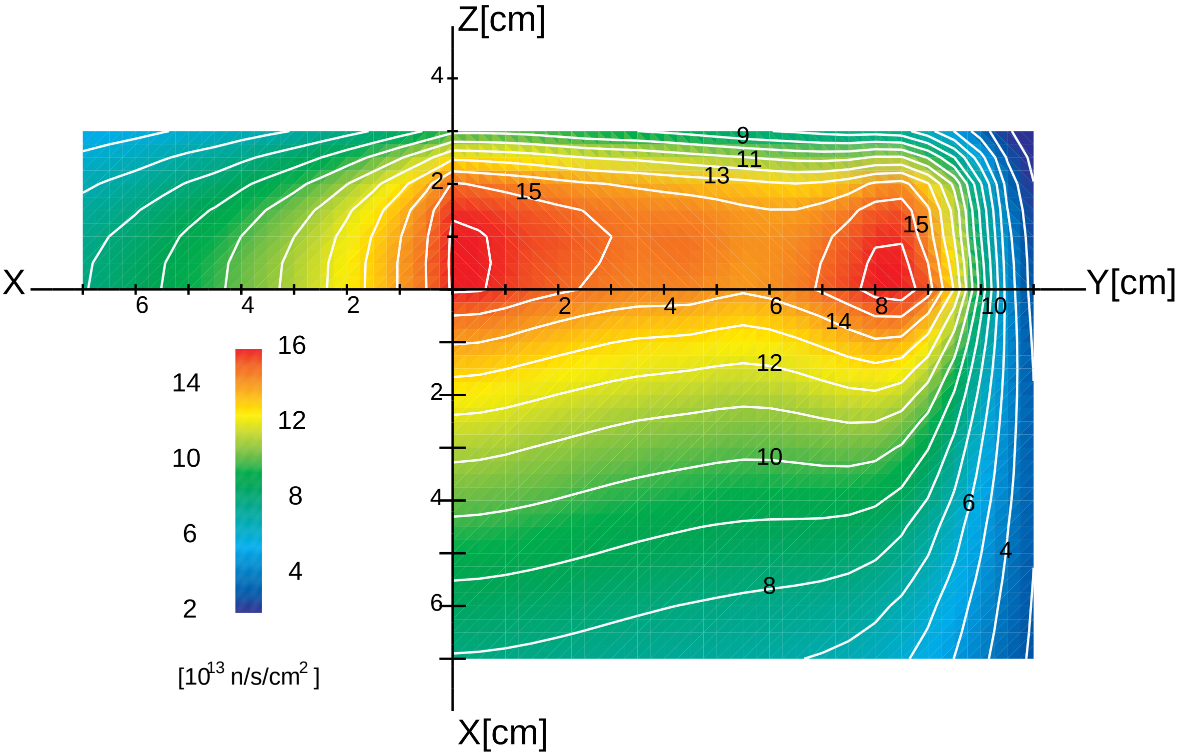

(a) INS

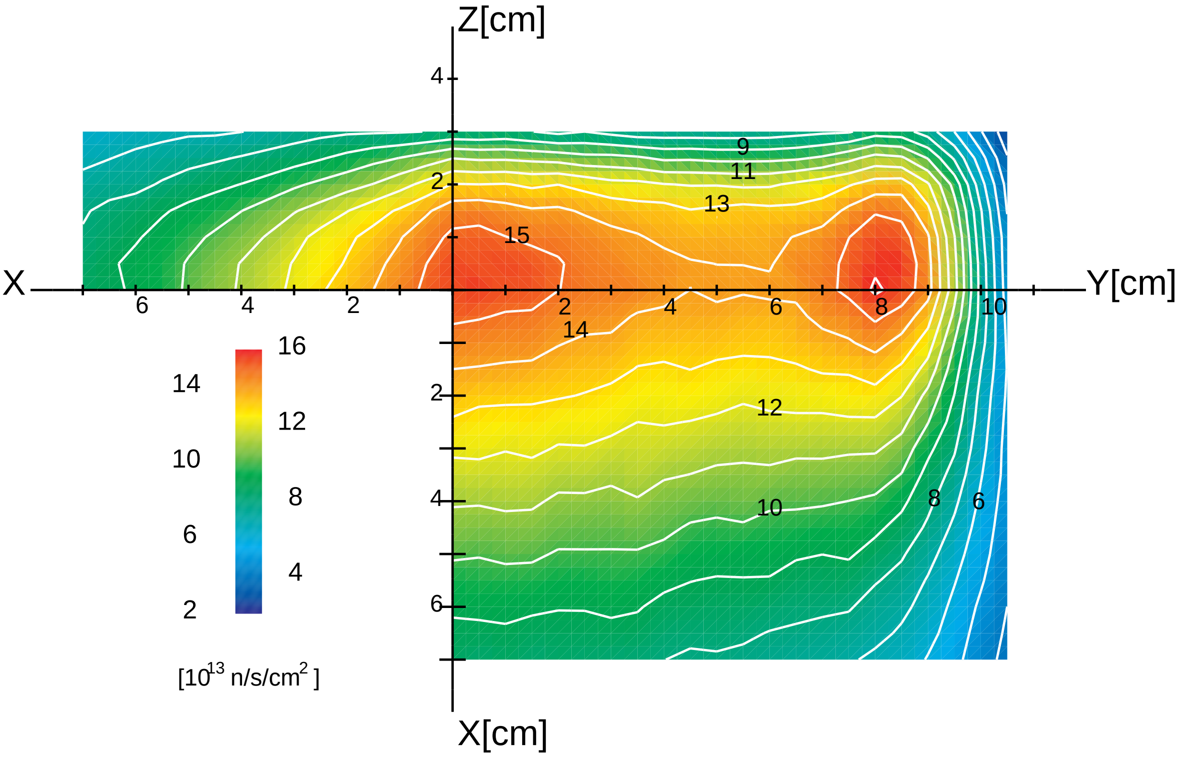

(b) MCNP

Figure 4.4: Neutron flux with energy greater than 14 MeV.

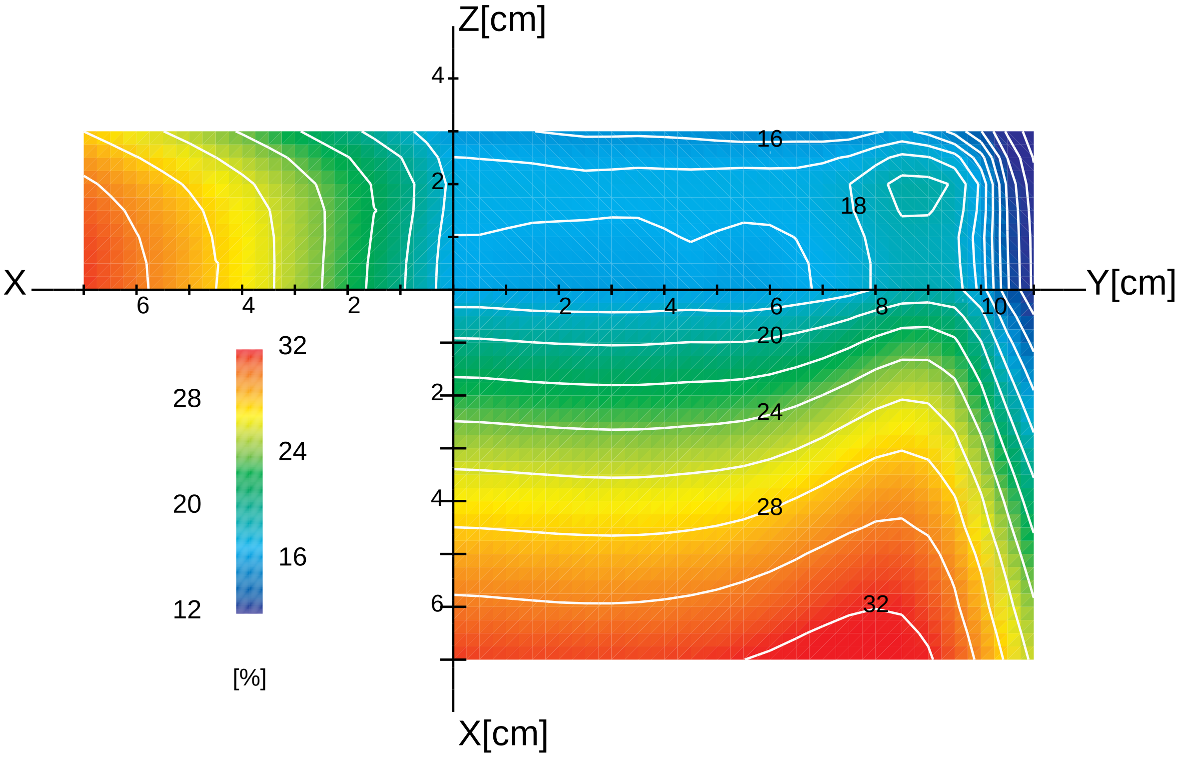

(a) INS

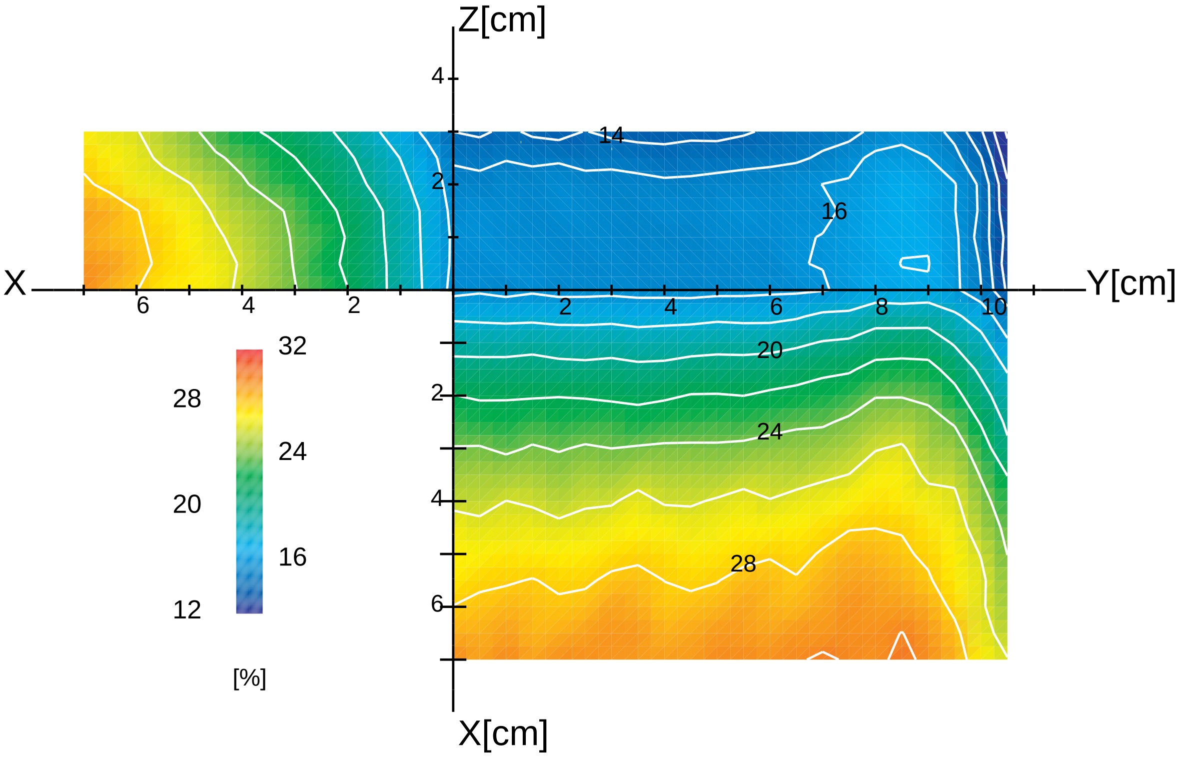

(b) MCNP

Figure 4.5: Fraction of neutron flux with energy greater than 14 MeV.

contributions lead to a reduced average energy and related lower fast flux. Throughout the test region, the fast flux fraction distribution is also directly influenced by the neutron source. The conical regions in front of each peak (at $y = 8.5$ cm) are dominated by the small angle contribution from the peaks themselves which have a higher average energy. Simultaneously, the flux peak at this location also serves to increase the contribution from source neutrons with large initial angles at other points in the distribution.

4.2.2 Neutron Spectra Comparison

Figure 4.6 shows a comparison of the neutron spectra at four points in the high flux test region. The 40 MeV maximum energy for the MCNP-M^{c}DeLi fluxes, particularly noticeable in figure 4.6(b), is due to the endothermic restriction of M^{c}DeLi. Even in the INS spectra, however, more than 99% of the flux has an energy below 40 MeV.

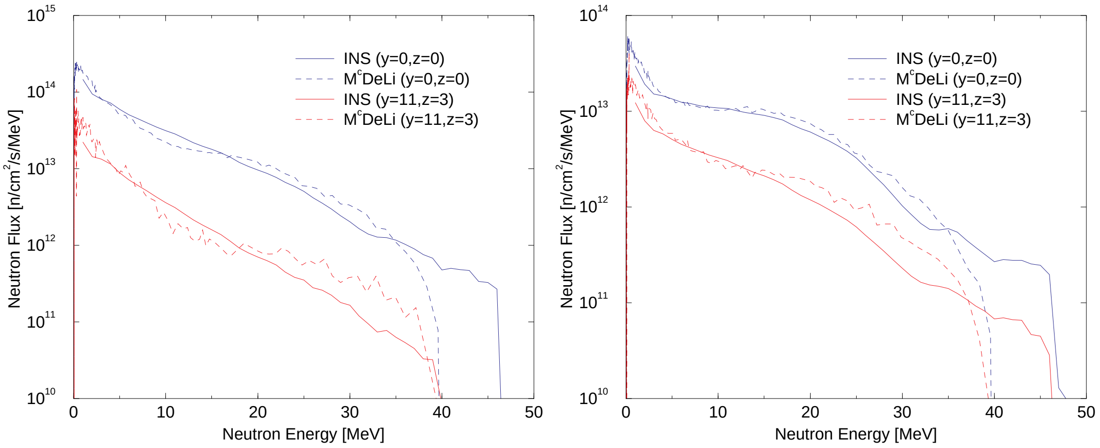

(a) $x = 0$ (b) $x = 6$

Figure 4.6: Flux spectra for INS and MCNP-M^{c}DeLi calculations.

The four chosen locations each demonstrate a particular feature of the neutron source itself as well as illustrating the differences between the model and the data set. The flux at the backplate centre ($x = y = z = 0$ cm) directly shows the energy dependence of the neutron flux summed over all the angles from 0° to 90°. In contrast, the position at the edge of the backplate ($x = 0, y = 11, z = 3$ cm) is outside the peak of the beam intensity distribution and its flux is therefore dominated by the larger angle contributions. While neither results have a strong stripping peak, the broader angular distribution of the FMIT data (see figure 3.5(b)) results in absence of a stripping peak in the INS results. At the central point away from the target ($x = 6, y = z = 0$ cm), the above mentioned geometrical effects cause the flux to be dominated by the small angle contributions, causing the stripping peak to be more prominent. The difference between the INS and

MCNP results is directly related to the differences between the FMIT data and the model in the forward direction (see figure 3.4(b)). The geometrical effect is much more significant at the outside point away from the target ($x = 6, y = 11, z = 3$ cm). In this case, there is actually an increase in flux for energies above 10 MeV in comparison to the point at the backplate's edge in both the INS and the MCNP results. This is due to a replacement of the strong large angle contribution from the beam intensity distribution peak with a strong small angle contribution from that same peak.

4.2.3 Neutron Flux Distribution Comparison

The spatial distributions agree quite well, certainly demonstrating that the MCNP-M^{c}DeLi tool produces reasonable results. The MCNP results exhibit a larger total flux than the INS results, namely due to the total neutron yield's angular distribution (recall figure 3.5). Although the total yield of the MCNP model with parameter set F is smaller, the yield is concentrated in the forward direction, resulting in a higher yield in the high flux test region. The fast flux ($E_n > 14$ MeV) of the INS results is greater at the backplate than the MCNP results. This can be explained by the average energy's angular distribution (recall figure 3.6). The average energy of the FMIT data used in INS is slightly higher than the average energy of the M^{c}DeLi model for all angles between 5° and 30° and much higher for greater angles. Since the neutron flux close to the target contains large contributions from all of these angles, the higher average energy translates directly into a larger fast flux. The stronger spatial attenuation of the fast flux in the INS case is further evidence of this cause. The combination of these differences results in a slightly larger fast flux fraction for the INS results. The larger average energy of the S parameter set for all angles would give a fast flux fraction more similar to the INS results.

MCNP-M^{c}DeLi agrees well with INS for the individual flux spectra as well as the shape and magnitude of the neutron flux's spatial distribution. Any disagreement can be explained by the difference between the M^{c}DeLi model and the FMIT data set.

4.3 Using the Intermediate Energy Transport Data

A comparison the partially validated 3-dimensional results of the previous section to similar results for a non-streaming problem with 50% ^{56}Fe in the high flux test volume permits a basic testing of the intermediate energy transport data. Figure 4.7 shows such a comparison using the the parameter set fitted to the Sugimoto data.

The most notable feature of this comparison is the increased total flux at locations near

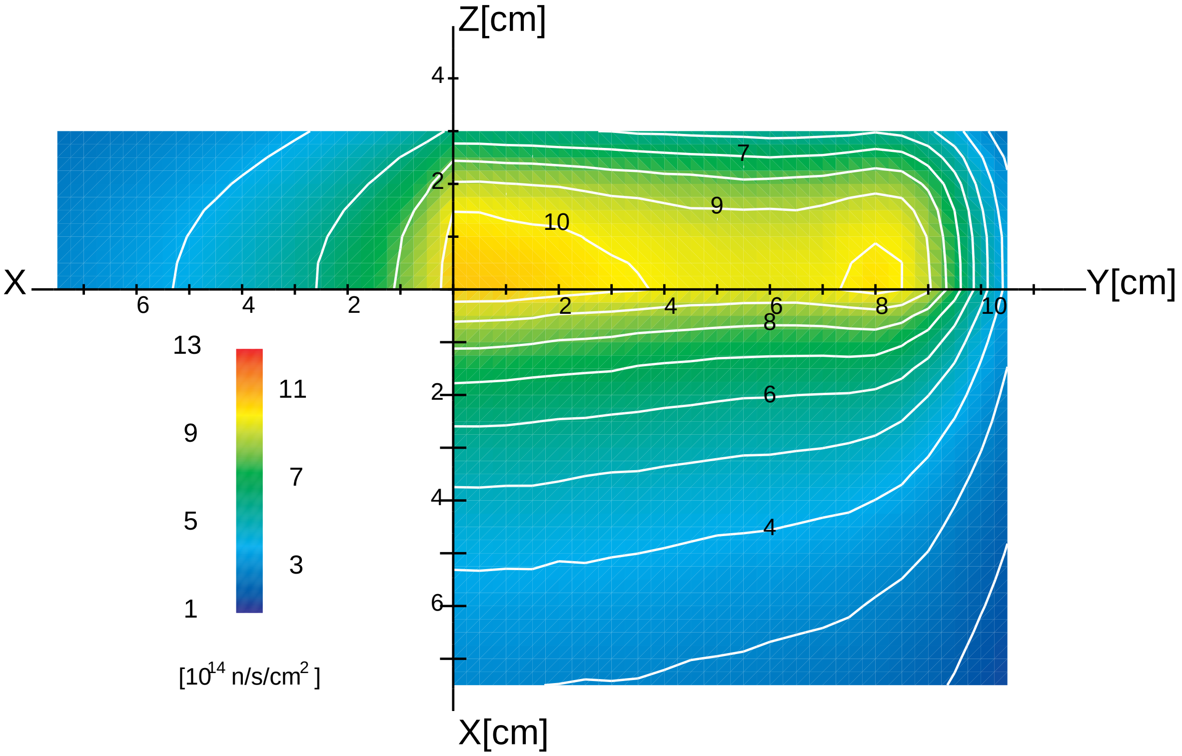

(a) Empty test cell

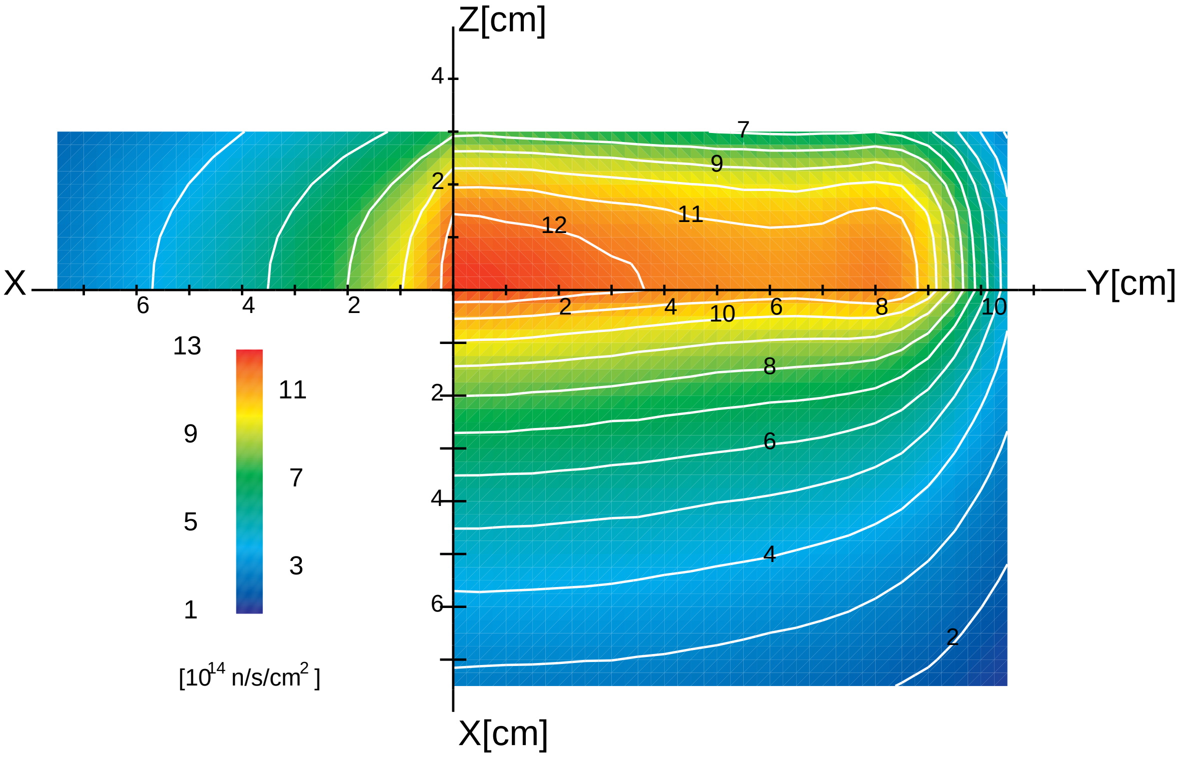

(b) 50% ^{56}Fe

Figure 4.7: Comparison of neutron flux in void and loaded test cells.

the backplate where the collided flux is approximately 20% larger ($>1.2 \times 10^{15}$ n/cm^2/s) than the uncollided flux ($> 1.0 \times 10^{15}$ n/cm^2/s). Similarly, by comparing the location of the contour line indicating 3×10^{14} n/cm^2/s in the x-y plane, a decrease in the flux can be seen as a result of the material loading at locations further downstream from the target. This changes combine to result in an increased spatial attenuation – over 70% between $x = 0$ and $x = 6$ cm along the x-axis.

Figure 4.8 shows a similar comparison for the flux fraction with energy greater than 14 MeV. Most notable in this comparison is that the high energy flux is virtually unchanged at positions near the backplate, but is otherwise lower throughout the high flux test region. At $x = 6$ cm on the x-axis, the material causes more than a 30% decrease in the fast flux, although the total flux is virtually unchanged at this point. This combines to lower the importance of the collided fast flux (less than 22% throughout) compared to the uncollided case (up to 33%). Note, however, that the fast flux's importance does still increase in the direction away from the target, indicating that the purely geometrical effects are still prominent.

The behaviour of the neutron flux with the addition of material to high flux test region is exactly as expected. With the iron now present in the high flux test region, the neutrons undergo a wide variety of reactions which can be classified into three general groups: scattering reactions, absorption reactions, and neutron-producing reactions. The effect of all three of these can be seen, to some extent, in the above comparisons. The increase in flux near the backplate is due to a combination of neutrons being scattered back into this region from downstream material and neutrons being produced in all parts of the high flux region. The flux attenuation, both the slight decrease seen in the total flux in regions further from the backplate and the more general decrease seen in the high energy flux, is due to the scattering and absorption reactions which reduce the number of neutrons which reach these region. Since many of the neutron-producing reactions have fairly high energy thresholds, they represent a major mechanism for the slowing down of the flux, with a number of low energy neutrons replacing each high energy neutron which undergoes such a reaction. This is the reason that the high energy flux attenuation caused by the material at a single spatial point is far more prominent than that of the total flux.

While this does not constitute a true benchmark or validation of the neutron transport data, it does demonstrate that the data are within a reasonable range and produce results within expectations.

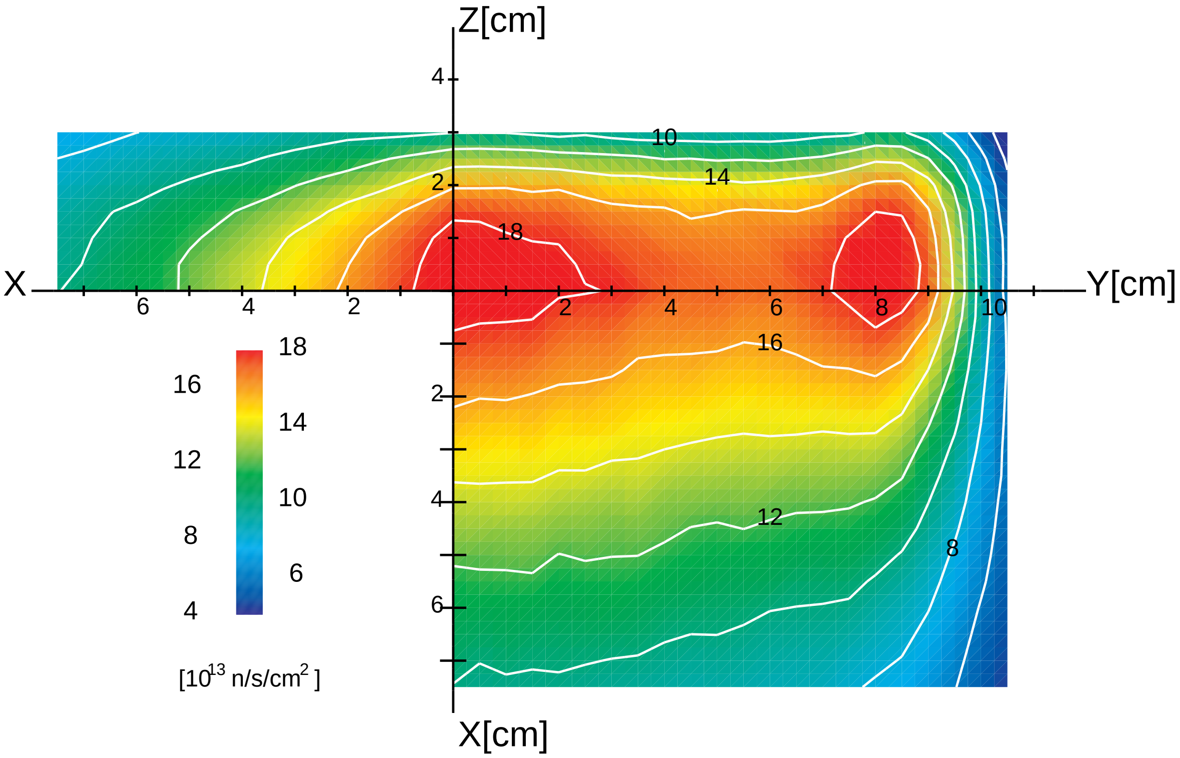

(a) Empty test cell

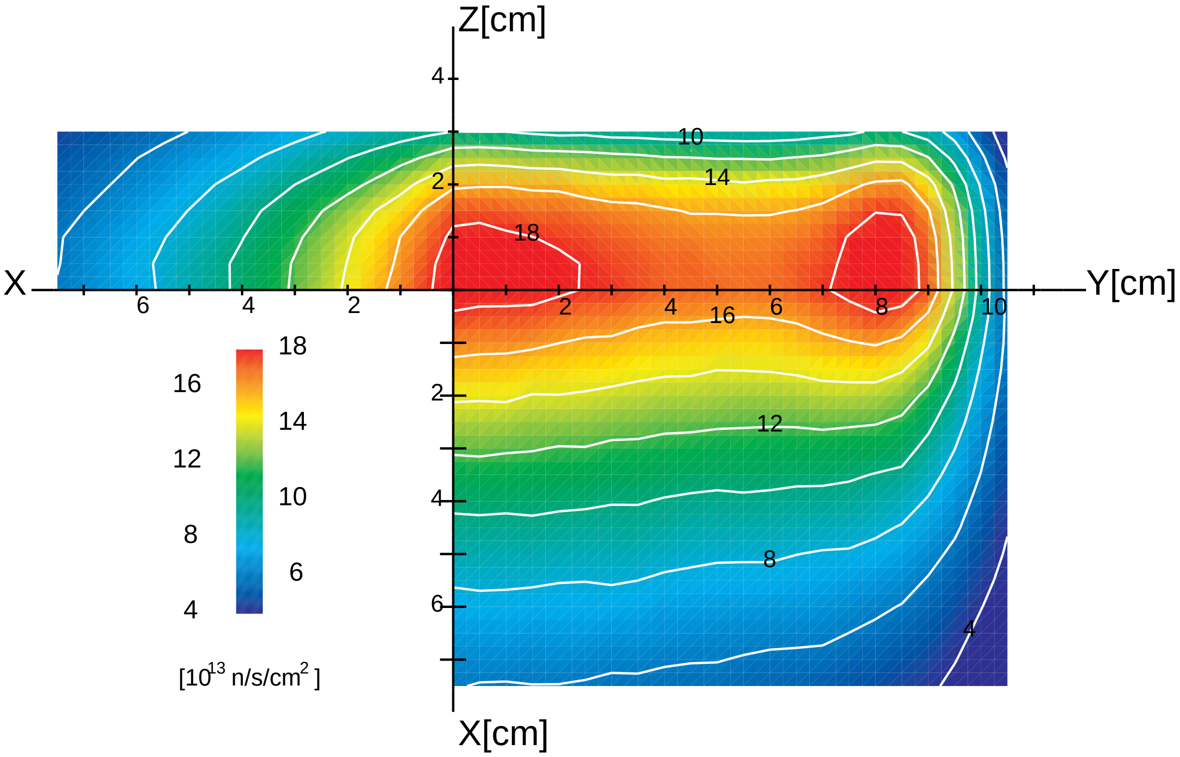

(b) 50% ^{56}Fe

Figure 4.8: Comparison of neutron flux with energy greater than 14 MeV.

4.4 Neutron Source Uncertainty

One important source of uncertainty in the neutron flux, and therefore all the neutron responses, is due to the M^{c}DeLi neutron source model itself. By calculating and analysing results for both sets of M^{c}DeLi fitting parameters given in table 3.1, some measure of the uncertainty can be obtained. These parameter sets will be referred to as set S for the set which was fitted using the Sugimoto data, and as set F for the set which was fitted using the FMIT data. Figures 4.9 and 4.10 give more information about the geometrical variation of this flux and the fraction of this flux with energies higher than 14 MeV, for both parameter sets.

The spatial distribution's general shape is not affected by the choice of parameter set. In both cases, all the features of section 4.2 are visible, whether they are due to the beam intensity distribution, the geometrical attenuation, or the Li(d,xn) model's angular distribution. There are differences, however, in the magnitudes of the results.

Comparing the total neutron flux distributions of the two parameter sets, the difference in the total neutron yield (7.2% *vs* 6.7%) corresponds directly to a difference of 6.5 to 8% in the fluxes close to the target. Parameter set F, however, shows a higher level of attenuation than set S, resulting in a difference of about 13% away from the target. The narrower angular distribution of set S has a mitigating effect on the total flux spatial attenuation, as described in section 4.2.1.

The differences in the high energy flux fraction is also due directly to the fitting parameters. From table 3.1 it is clear that the only difference between the two parameter sets is the magnitude of the Serber stripping component. Since the majority of the high energy flux is produced by this component of the neutron source model, the 21% difference in these values corresponds directly to a nearly uniform 21% difference in the magnitude of the high energy flux throughout the high flux test region.

The uncertainties in many of the other neutron responses will be directly related to this neutron flux uncertainty. Chapter 5, where these other responses will be considered, will be based primarily on the results of set S, with discussion of the other parameter set in situations where the uncertainty a particularly important impact on IFMIF.

4.5 Importance and Completeness of the Intermediate Energy Activation Data

Now that the neutron flux results are available for a region loaded with material, the intermediate energy activation files [IEAF] can be tested. More detailed information about expected activation and decay heat levels in the IFMIF high flux test region will

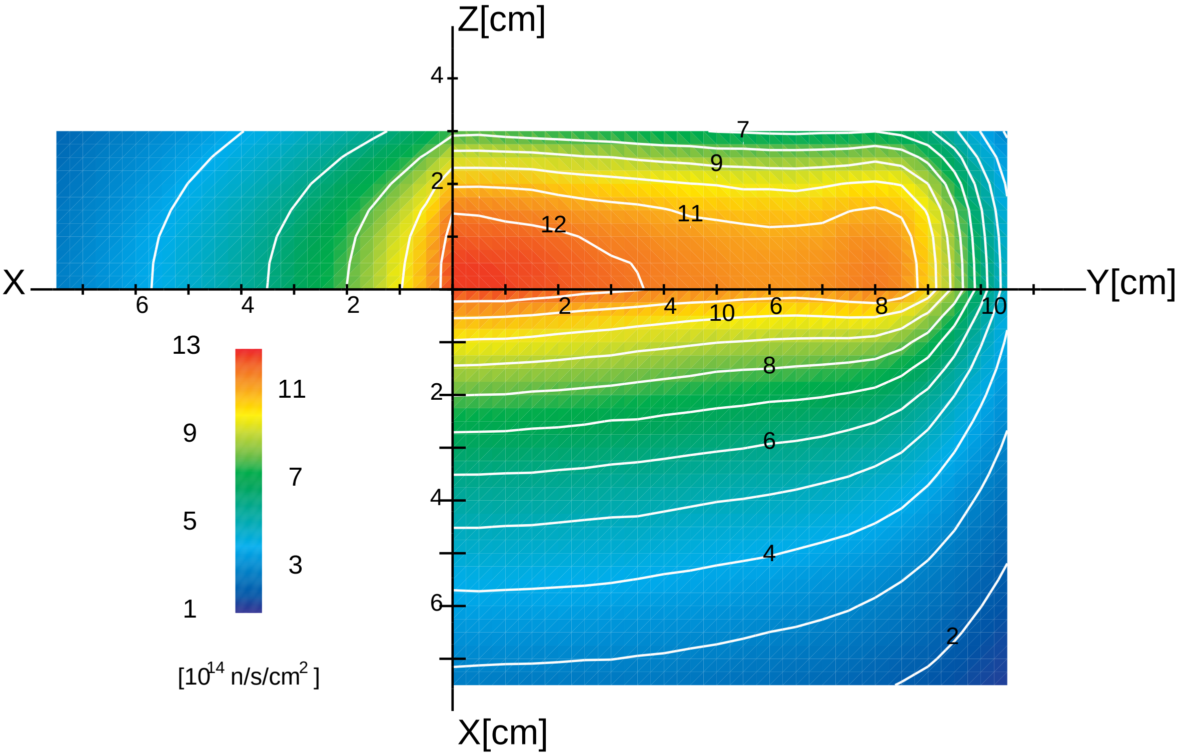

(a) Parameter set S

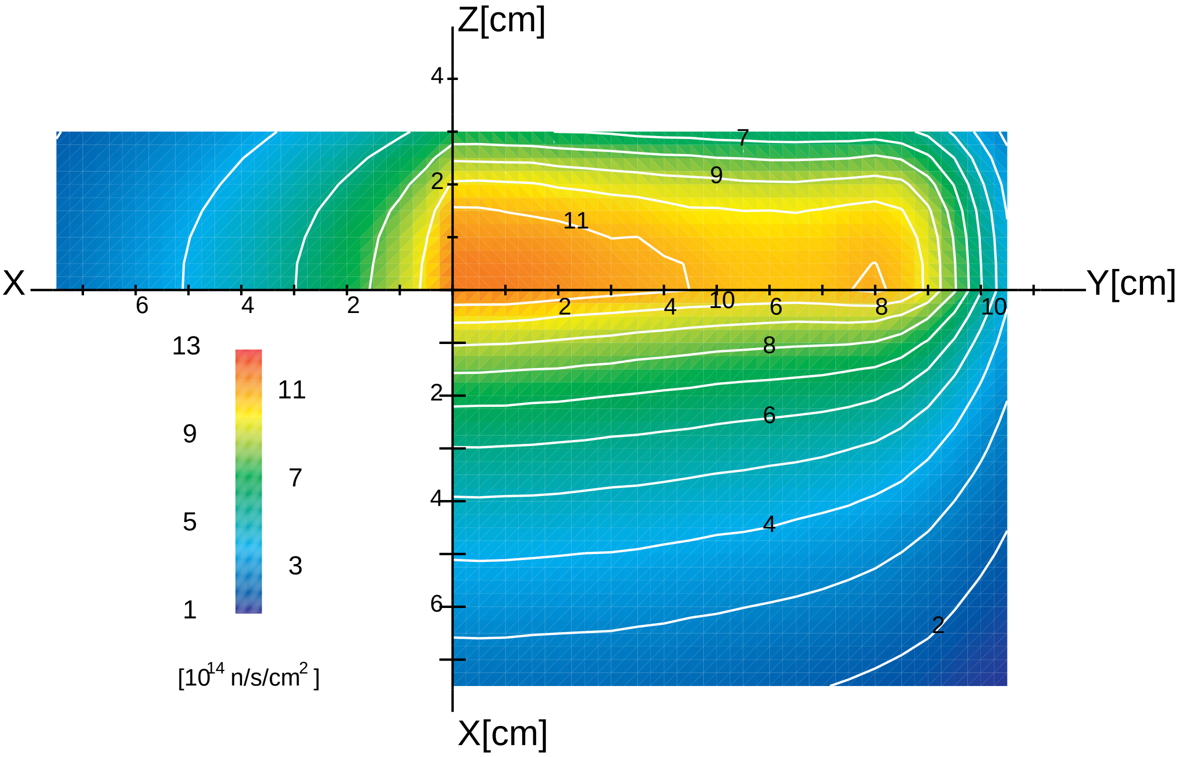

(b) Parameter set F

Figure 4.9: Total neutron flux.

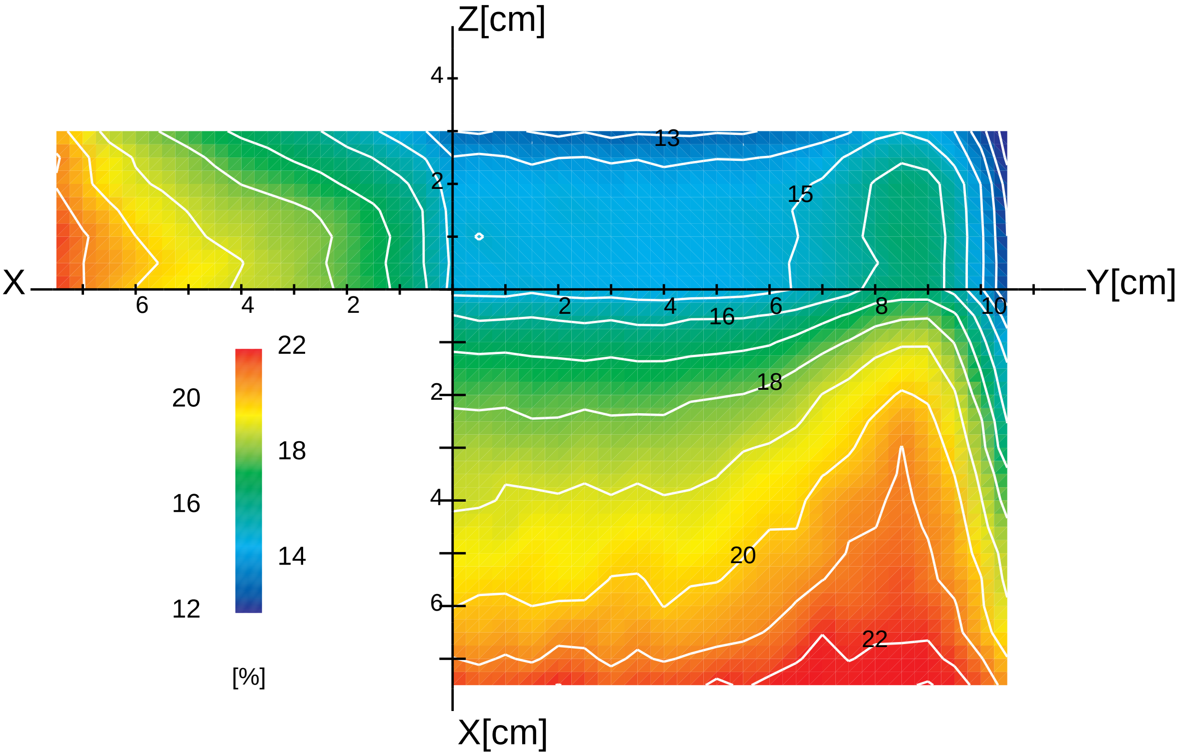

(a) Parameter set S

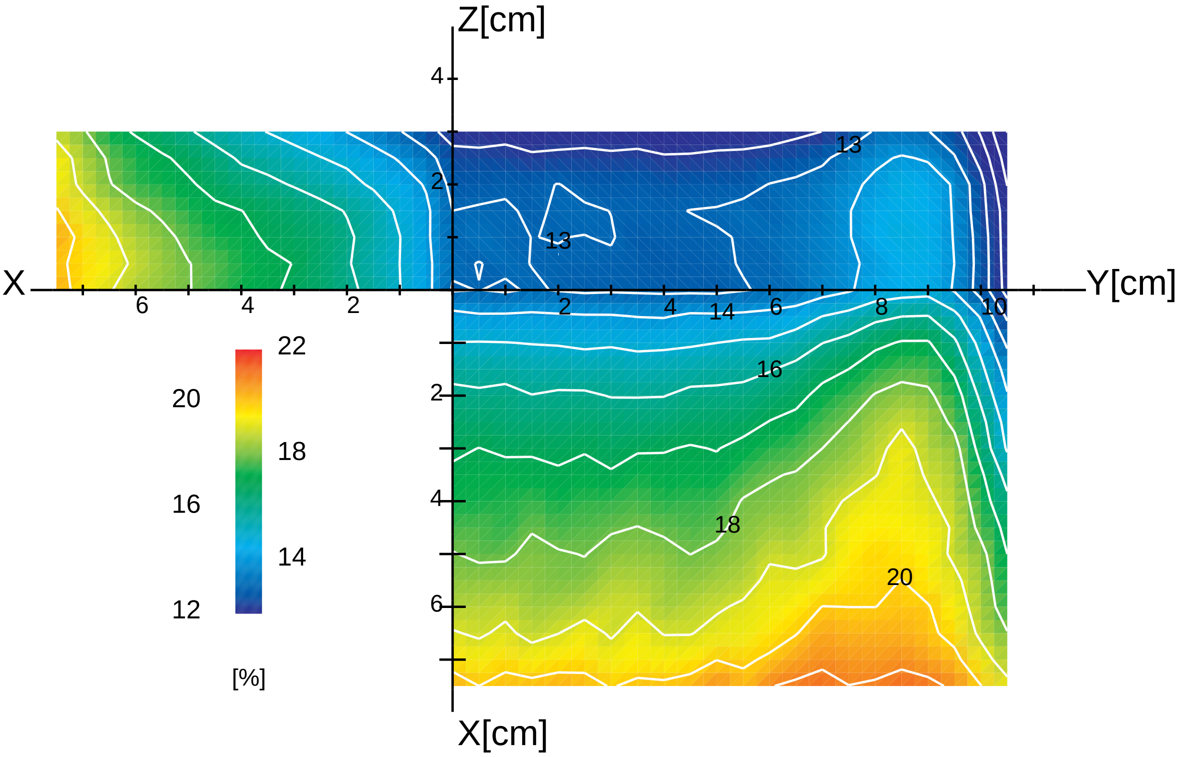

(b) Parameter set F

Figure 4.10: Fraction of total flux with energy > 14 MeV.

be given in section 5.1.5. In this section, the importance of the IEAF data will be shown by comparing it to previously available data and approximations. In addition, the completeness of this data will be partially demonstrated.

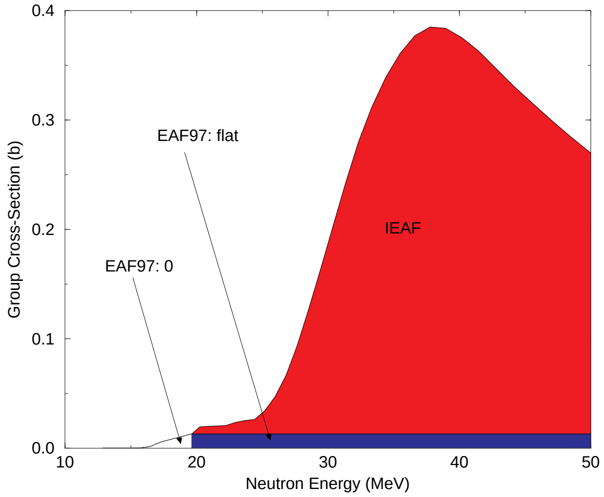

Figure 4.11: Comparison of ^{56}Fe(n,x)^{52}Mn cross section.

Until this data became available, a number of approximations had been made in order to perform some initial calculations of activation in the IFMIF facility. Although very unrealistic and rarely used, the easiest approximation is to simply assume that the cross section for all higher energy neutrons is zero. That is, use the available data library as it is, with no adjustments. Another, slightly more realistic approximation is to assume that the cross section for the higher energy neutrons, or neutron groups, is the same as the cross section at the highest energy available in the existing data. This can be implemented in two ways: extend the data library with a constant cross section to higher energies or combine the high energy neutron flux into the available data's highest group. Figure 4.11 compares the IEAF ^{56}Fe(n,x)^{52}Mn cross section to the EAF97[23] values for the same cross section, extended using the two methods described above.

Complete libraries were generated from the EAF97 files based on both approximation methods (labelled EAF97:0 and EAF97:flat, respectively) and used, in addition to the IEAF data, to calculate activation and decay heat results for natural iron in the IFMIF high flux test region. Figure 4.12 shows the relative difference between the activation results at shutdown of the EAF97:flat approximation and the IEAF data, as well as a decay heat comparison one day after shutdown.

As would be expected, the EAF97:0 approximation grossly underestimates the activity uniformly throughout the high flux test region, with an error of about 37%. The differences between the IEAF data and the EAF97:flat approximation, however, are more subtle. By comparing the specific activity alone, the EAF97:flat results appear to be well within an appropriate error range, overestimating the activity by less than 7% throughout most of the test region. The decay heat results, however, show that these results are not entirely consistent. After a one day cooling period, the EAF97:flat is underestimating the decay heat by as much as 30%. This inconsistency is easily explained by the fact that the two libraries lead to different relative inventories of radioactive isotopes. While the

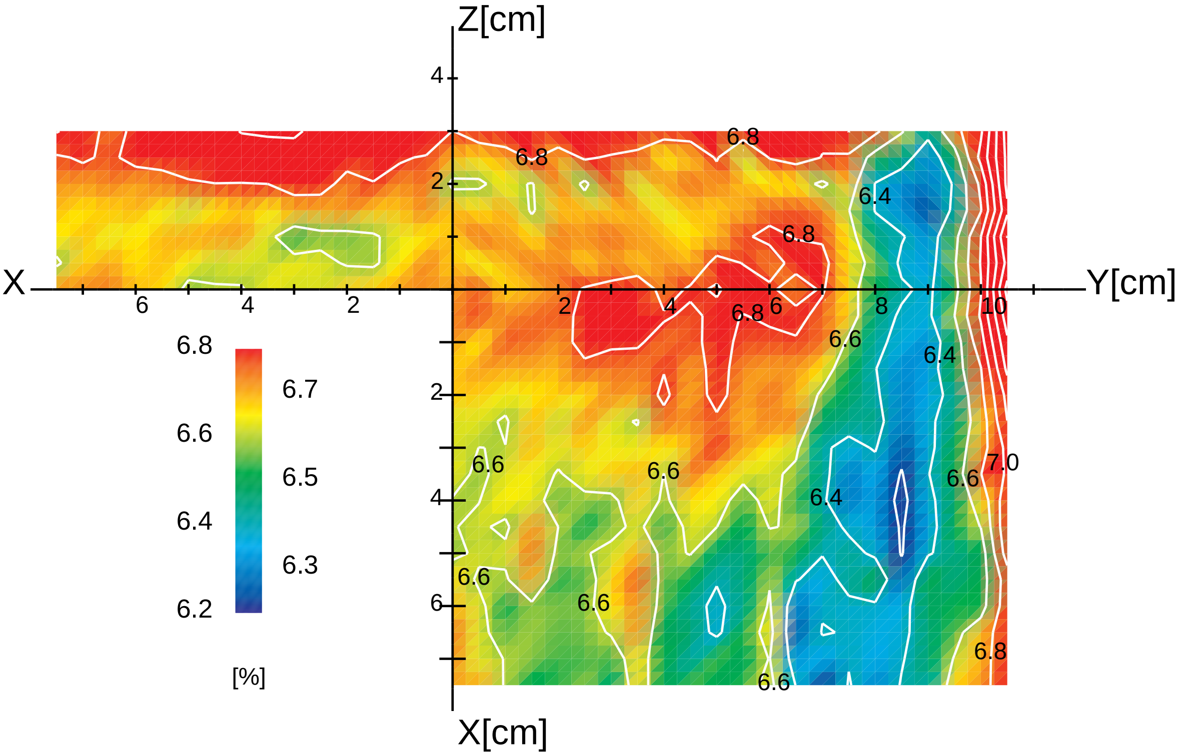

(a) Specific activity at shutdown

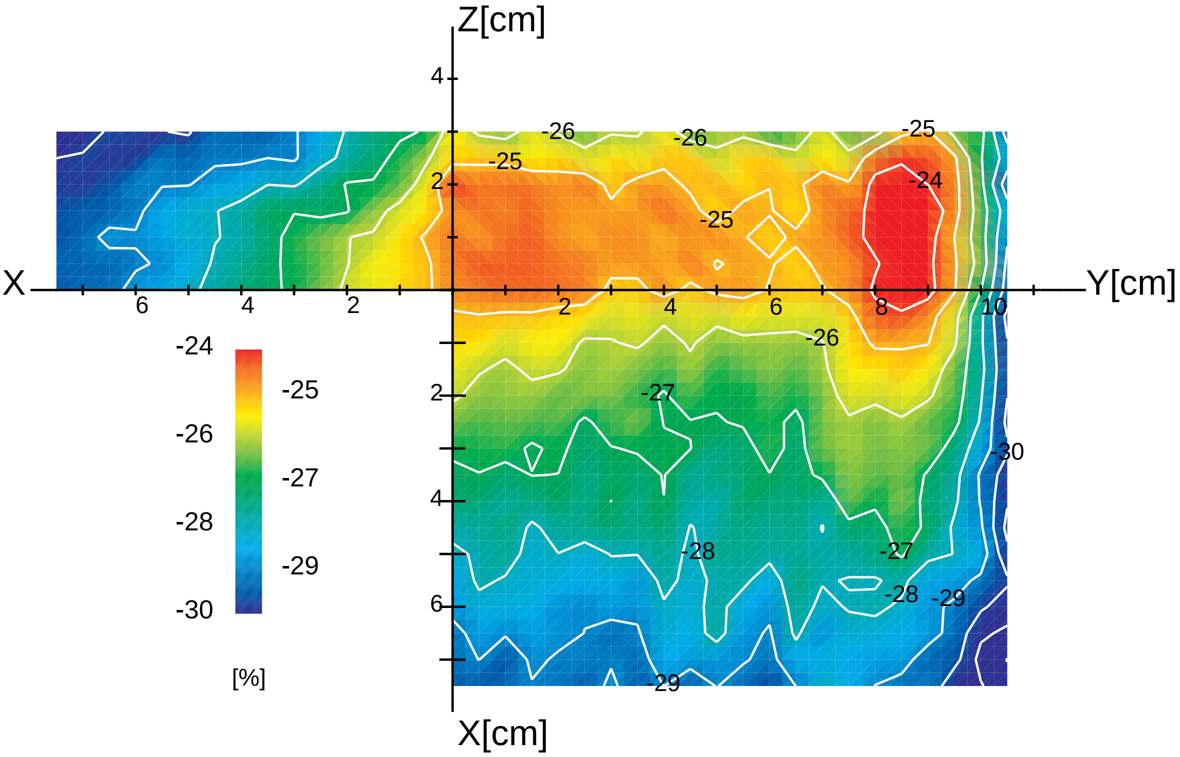

(b) Decay heat after 1 day cooling time

Figure 4.12: Relative error of EAF97:flat approximation in IFMIF high flux test region.

specific activity is dominated by the presence of ^{55}Fe, the decay heat at one day is dominated by the presence of ^{54}Mn. The EAF97:flat approximation leads to the overestimation of the former and the underestimation of the latter. These results demonstrate why it is important that the IEAF data continue to be evaluated and improved for a wide range of isotopes.

As mentioned in previous chapters, activation libraries differ from neutron transport data libraries because they require data for as many different isotopes as possible. If the data library is not sufficiently complete, the results may not include important activation pathways. The IEAF data currently includes 100 important isotopes (and isomers) between flourine and nickel. One way to measure the completeness of the current set of IEAF data is to compare it with a library which contains more isotopes. Such a library was created by supplementing the IEAF library with cross sections for other isotopes based on the EAF97:flat approximation. When comparing this library's results to the pure IEAF results, the relative differences are of the order of magnitude of the numerical accuracy. Examining the activation trees which are generated by the ALARA code shows that the only difference is that the light ions produced by the neutron reactions may undergo some inconsequential transmutations (for example, the tritium which decays to ^{3}He may be partially transmuted back to tritium). This demonstrates that the IEAF is complete enough to determine the activation related responses of iron in IFMIF.

4.6 Further Validation and Benchmarking

Future validation and benchmarking will be necessary to ensure that the tools and data which have been developed for IFMIF are capable of providing valid estimates of the neutron flux and neutron responses in IFMIF. This will require experiments designed to benchmark all three aspects mentioned in this chapter. Experiments are already underway to improve the understanding of the neutron yield from the Li(d,xn) reaction.[36] This is the most important aspect since the uncertainty in the neutron yield contributes directly to the uncertainty in all the other calculated results of IFMIF. A variety of experiments will also be important for benchmarking the cross section data. There are many ongoing experiments for benchmarking such data at energies up to 14 MeV,[52,53] but experiments will also be important at energies up to 50 MeV or higher. The recent increase in spallation neutron will hopefully provide additional incentive to perform such benchmarking activities.

Although they does not constitute a complete validation or benchmarking of the data or tools developed for IFMIF, the above results do serve to provide confidence in the results to allow a complete characterisation of the IFMIF high flux region, as will be shown in the next chapter.

Chapter 5

Neutronics Characterisation of the IFMIF High Flux Region

Using the M^{c}DeLi source module described in chapter 3, a thorough characterisation of the high flux region and the current reference High Flux Test Module [HFTM] have been carried out. First, a volumetric characterisation of the neutron responses was calculated in a uniformly filled region of space, providing information about the general characteristics of the region. Then, an analysis was performed to determine the neutron responses within the test rigs of the HFTM itself. The results of both of these analyses were compared to standard DT fusion conditions such as those anticipated in the DEMO blanket.

The primary purpose of these analysis is to determine whether the high flux region of the IFMIF test cell can meet the requirements of the facility as a whole. In particular, it is important to calculate the available volume with damage rates above 20 DPA/fpy and the response gradients throughout the region. It is also necessary to determine whether the IFMIF test cell provides a good simulation of a DT fusion environment.

5.1 Volumetric Characterisation

As in the neutron flux analysis, the geometry for the volumetric characterisation problem consisted of the $8.25 \times 24 \times 11$ cm^3 volume referred to in the previous chapter. As a rough approximation of the final material loading of the high flux test region, the volume was uniformly filled with 50% ^{56}Fe/50% He(void). In addition to 205 group neutron fluxes (175 vitamin-j groups[54] plus 30 groups of uniform lethargy width between 20 and 50 MeV), MCNP tally multipliers were used to calculate the damage rate, gas production, and nuclear heating.

Using the same data representation described in chapter 4, one plot will be used to visualise each of the important and interesting responses. For the damage rate data, one further representation is given to help visualise the actual volumes which meet the criteria of the damage rate being greater than 20 DPA/fpy. These representations also give some feeling for the behaviour of the responses in the "opposite corner" away from all three reference planes. Due to the statistical variations inherent in Monte Carlo calculations, these contours and surfaces may not appear smooth in all cases, particularly as more mathematical operations are applied to the data (eg. gradients and ratios).

5.1.1 Neutron Flux Gradients

Based on the neutron flux results shown in chapter 4, local gradients were computed throughout the high flux region, and are shown in figure 5.1. It is clear from these results that the flux gradients will always be above ≈ 20%/cm and the largest gradients are caused simply by the finite size of the target/neutron source. Due to the symmetry of the problem, the gradient's direction is perpendicular to the contours shown in figure 4.9(a).

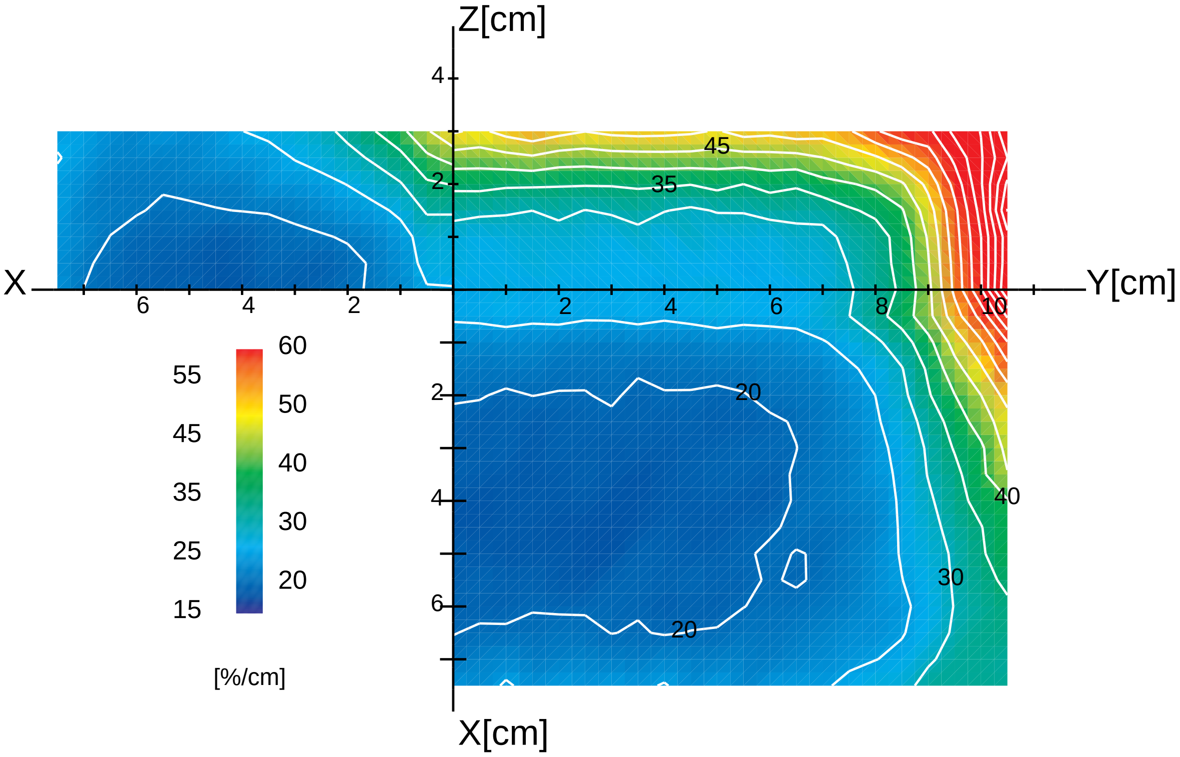

Figure 5.1: Magnitude of local flux gradients.

5.1.2 Gas Production

One important engineering response is the amount of gas produced by nuclear reactions in a material. The protons and alpha particles which are emitted by many of the nuclear reactions eventually slow down in the material and form hydrogen and helium bubbles. These bubbles cause swelling and embrittlement of the materials, both of which are detrimental to its mechanical performance. Figure 5.2 shows the both the hydrogen and helium gas production rates. The hydrogen production rate is between 500 and 2750 atom parts per million per full power year (appm/fpy). The helium production rate is roughly 4 times lower with a range of 125 to 700 appm/fpy.

5.1.3 Damage Rates

The primary response used to measure the irradiation environment of IFMIF is the damage rate, measured in displacements per atom per full power year (DPA/fpy). Figure 5.3 shows the spatial distribution of the damage rate, with a maximum damage rate of nearly 65 DPA/fpy at the backplate. Since one of the requirements for IFMIF is the available irradiation volume, figure 5.4 shows the size and shape of the 3-dimensional volumes which meet the minimum damage rate criteria of 20 DPA/fpy (green), 30 DPA/fpy (yellow) and 40 DPA/fpy (red). The grid shown in this figure represents the IFMIF CDA reference High Flux Test Module [HFTM]. Table 5.1 shows the actual volume at each of these damage rate levels. While this single value gives a quantitative measure of the radiation induced damage, a characterisation of the damage is also important. This will be done in more detail in section 5.2.3.

Displacement damage rate [DPA/fpy]	Volume [cm^3]	
	Total	inside HFTM
> 20	616	461
> 30	280	258
> 40	119	118
> 50	34	34

Table 5.1: Available volumes which meet specific damage rate criteria.

It is clear from both table 5.1 and figure 5.4 that much of the available volume with a damage rate greater than 20 DPA/fpy is outside the reference design for the HFTM. The implications of this characterisation on the HFTM design will be further addressed in section 5.3.

5.1.4 Nuclear Heating

The heat generated by nuclear reactions during operation of IFMIF is an important engineering response for determining the coolant flow requirements of the facility. In addition to ensuring the safe operation of the facility, the coolant flow must be designed to establish and maintain the different required temperature regions. Figure 5.1.4 shows the distribution of the heat source in the IFMIF high flux test region, given in watts per gram of ^{56}Fe. As with the other responses, the peak values of nearly 8 W/g occur in the backplate.

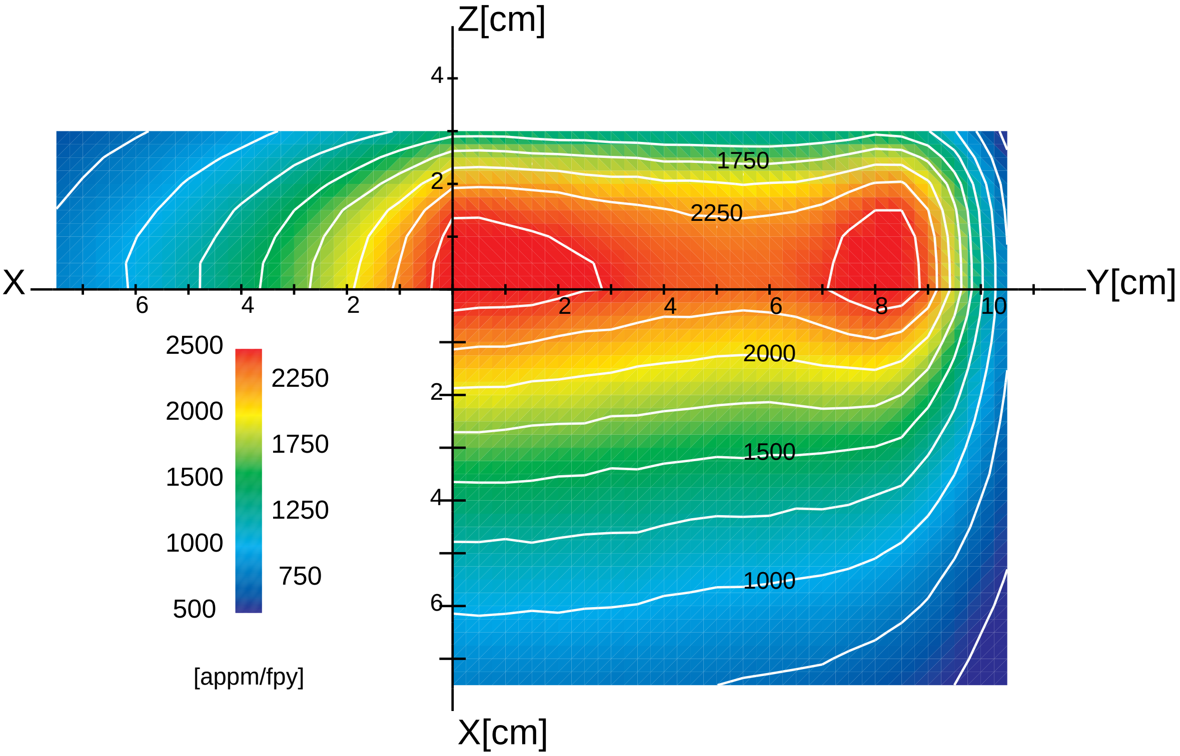

(a) Hydrogen

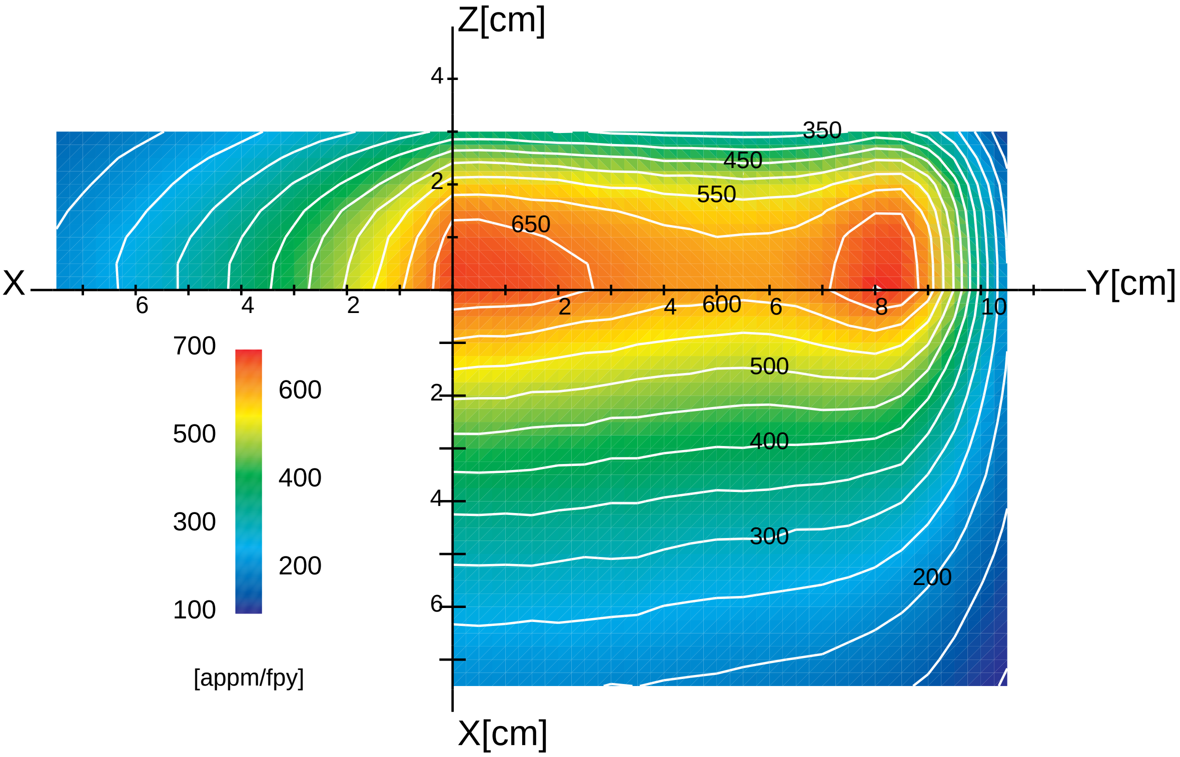

(b) Helium

Figure 5.2: Gas production rates in the IFMIF high flux test region.

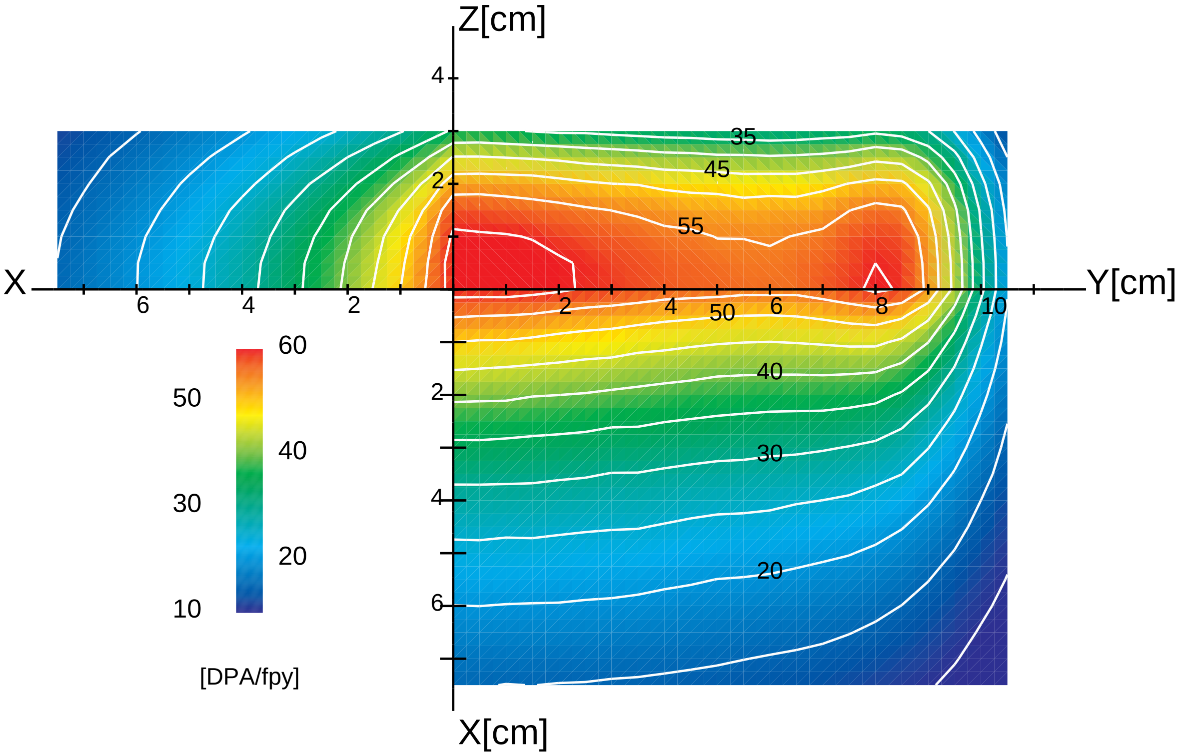

Figure 5.3: Damage production rates.

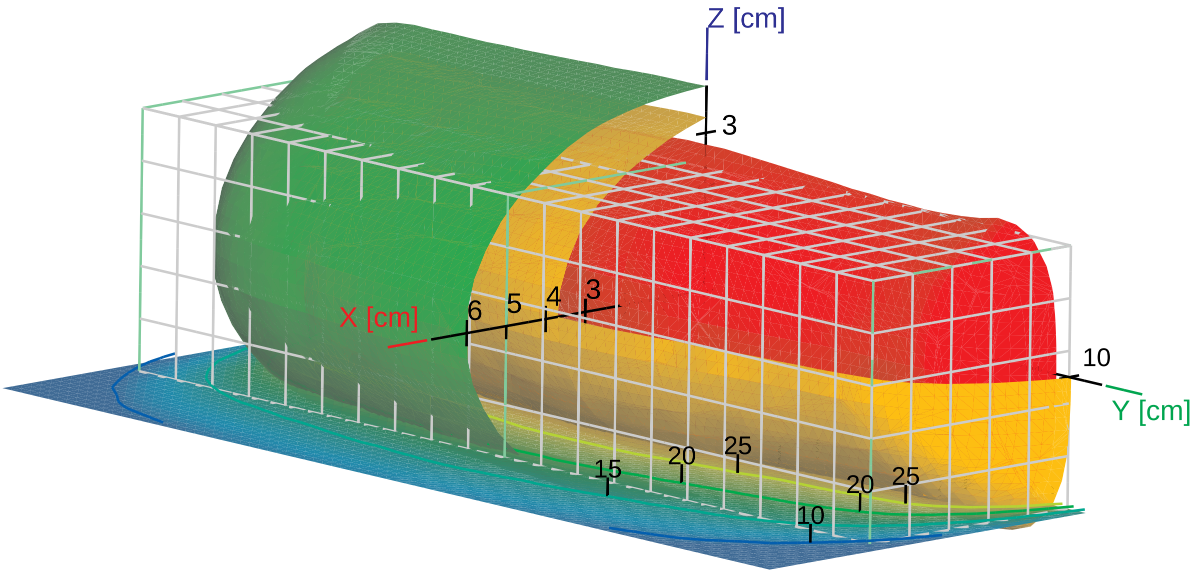

Figure 5.4: Available volumes which meet specific damage rate criteria. (Green: 20 DPA/fpy, Yellow: 30 DPA/fpy, Red: 40 DPA/fpy)

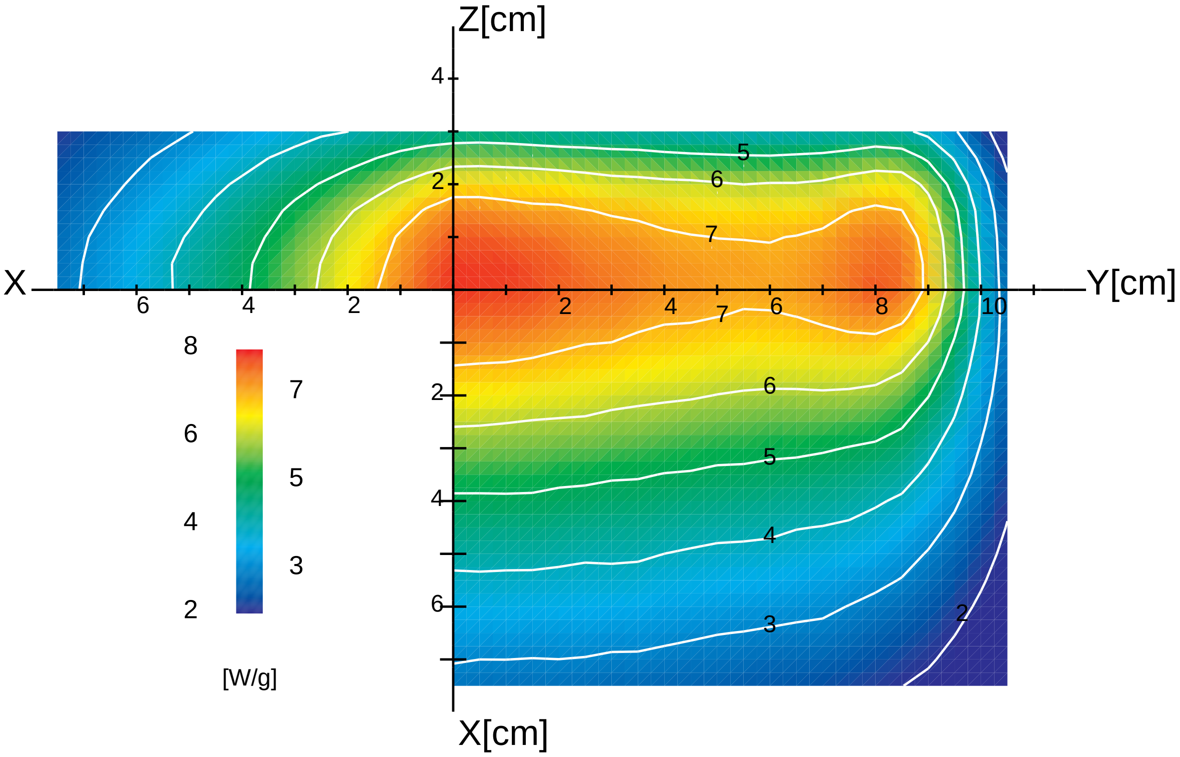

Figure 5.5: Nuclear heating distribution.

5.1.5 Activation and Decay Heat

Neutron induced activation is a primary response which, in turn leads to a number of secondary responses such as dose and decay heat. As with the radiation-induced damage, however, the specific activity is a very rough measure of the activity, and a more detailed characterisation is necessary. Furthermore, the activation and decay heat are time dependent results, decaying away after shutdown of the neutron source. Both of these issues will be addressed in section 5.2.4.

Figure 5.6 shows the specific activity and decay heat, respectively, at shutdown. For these calculations, it was assumed that the facility operated for 10 years, with 100 days of maintenance (no operation) per year, consistent with the 70% availability requirement. The activation levels are greater than 1.3×10^{15} Bq/kg in the backplate and the decay heat peaks at 150 W/kg. It is often important to know the ratio between the decay heat and the nuclear heating rates, to determine how much heat removal is required after shutdown. In this case, the decay heat at shutdown is about 2% of the nuclear heating rate during operation.

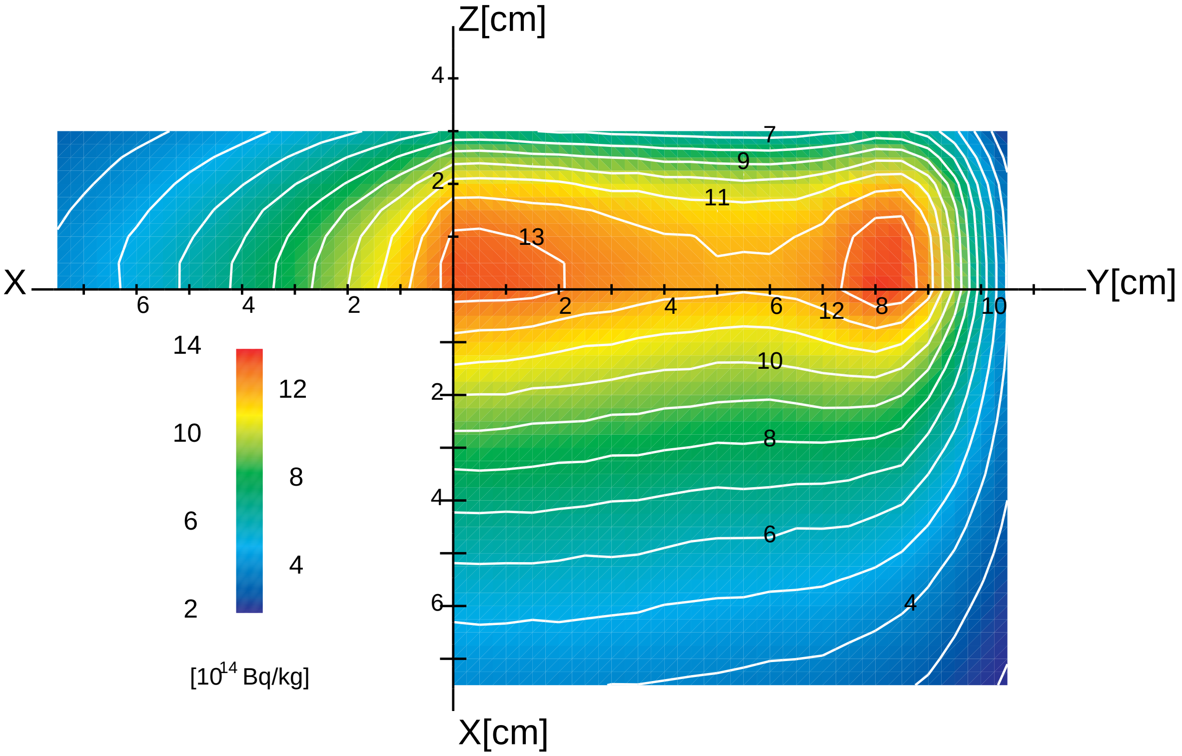

(a) Specific Activity

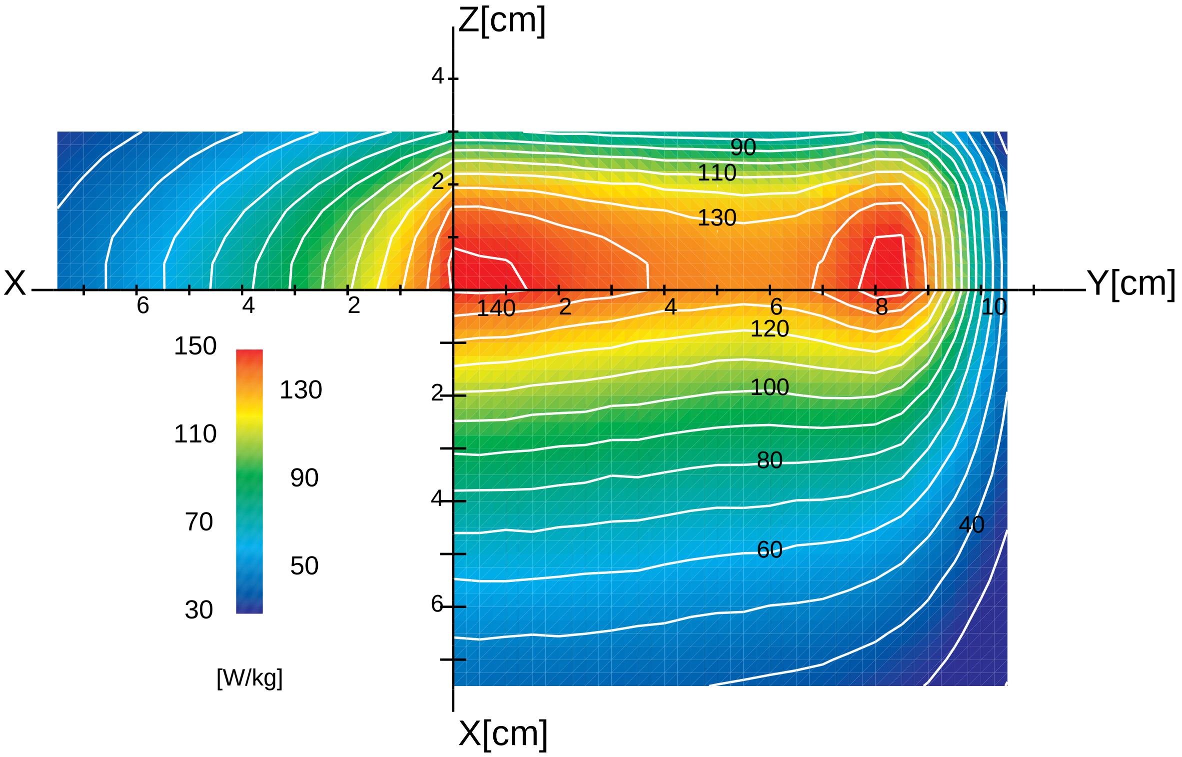

(b) Decay Heat

Figure 5.6: Activation responses at shutdown.

5.2 Comparison to DT Fusion Conditions

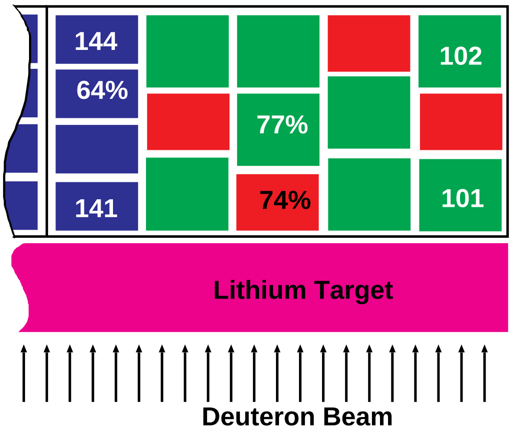

Figure 5.7: Plan view of the reference helium-cooled High Flux Test Module, indicating the cell reference numbers and relative iron densities.

While the above results offer a complete understanding of the spatial distribution of the various neutron responses, it is useful to choose a number of specific points for performing a detailed comparison to DT fusion-relevant conditions. For this purpose, calculations have been performed for the reference helium-cooled High Flux Test Module [HFTM], shown from above in figure 5.7. In these results, the same responses have been calculated, but in this case, they are averaged over the larger volume contained in a single test rig. While the local results for each of the important neutron responses will be roughly the same in the HFTM as shown in the previous sections, the results here permit a more detailed analysis of the damage and activation.

The four corner cells (101,102,141,144) will be used to represent the varied conditions of the HFTM. In table 5.2, results are for the whole cell averaged over a height of 4 cm are compared to results for both an ITER- and DEMO-type fusion reactor first wall.[6,55] The fusion reactor conditions have been normalised to maximum neutron wall loadings of 1.2 MW/m^2 and 3.6 MW/m^2 for ITER and DEMO, respectively.

	Damage Rate [DPA/fpy]	Gas Production [appm/fpy]		Gas-to-Damage Ratio [appm/DPA]		Heating
		He	H	He	H	[W/g]
DEMO	**30**	**330**	**1400**	**11**	**47**	**3.2**
ITER	**10**	**120**	**480**	**12**	**48**	**1.4**
101	33	416	1610	13	49	3.9
102	16	220	855	14	54	2.1
141	47	568	2196	12	47	5.3
144	23	321	1247	14	54	3.0

Table 5.2: Results for characteristic cells of the HFTM.

IFMIF's goal of providing an accelerated testing environment is certainly achieved. The damage rates throughout the HFTM are at least as high as in the fusion reactors and in many places they are two or three times larger. The same is true for the production rates of both helium and hydrogen.

5.2.1 Neutron Flux Spectra

Figure 5.8 shows the neutron flux spectra in cells 102 and 141 compared to the calculated neutron fluxes in an ITER and DEMO reactor first wall. All the fluxes have been normalised to a total flux of 10^{15} n/cm^2/s. It is clear from these comparisons that the flux spectra themselves are very different from those of a fusion reactor, with the most important difference being the high energy tail of the IFMIF flux, as was also apparent in figure 4.10(a). In all cases, the majority of the flux (>85% for the two fusion reactor spectra and between 75 and 80% in IFMIF) has an energy below 14 MeV. The remaining 15 to 25% of the total flux is distributed in IFMIF throughout the high energy domain, however, rather than the nearly mono-energetic peaks seen in the fusion spectra.

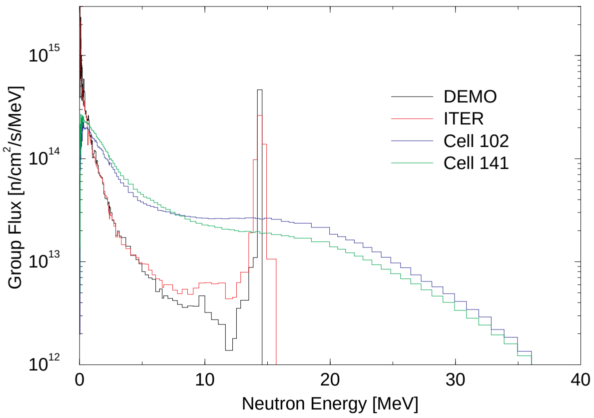

Figure 5.8: Comparison of calculated neutron fluxes for DEMO and ITER reactor first walls and IFMIF HFTM.

5.2.2 Gas-to-Damage Ratio

While a direct comparison of the gas production rates or the damage rates with fusion reactor conditions demonstrates the ability to perform accelerated testing of materials, further metrics are needed to determine IFMIF's suitability as a fusion simulation environment. The ratio of the gas production to damage rate provides such a measure. Figure 5.10 shows this ratio for both hydrogen and helium.

These distributions follow the distribution of the fast flux fraction (see figure 4.10), demonstrating that the gas production cross-section increases more rapidly for higher energies than the DPA cross-section. In figure 5.9, the gas-to-damage ratio is shown as it accumulates with increasing neutron energy. This figure demonstrates the importance of the high energy tail in the IFMIF spectra. Using only the flux under 14 MeV, the gas-to-damage ratio for IFMIF would be

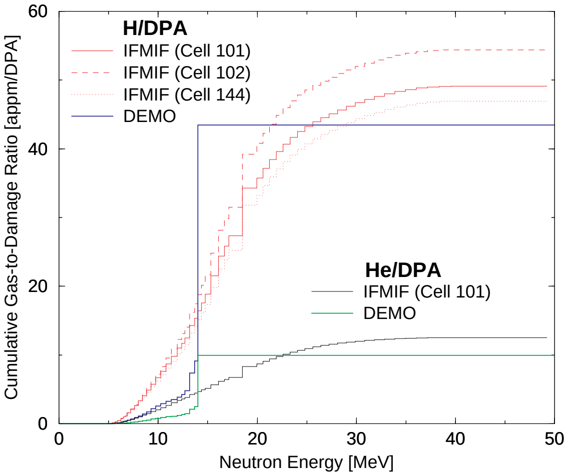

Figure 5.9: Cumulative Gas-to-Damage Ratio in ^{56}Fe.

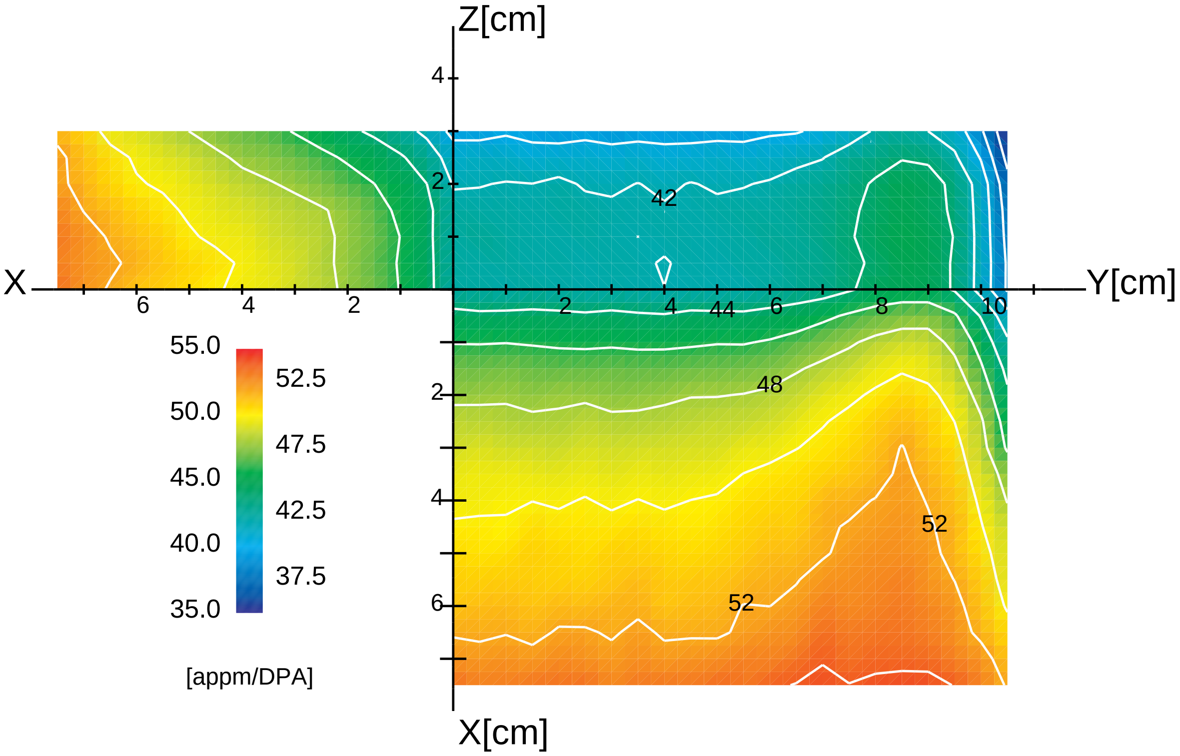

(a) Hydrogen

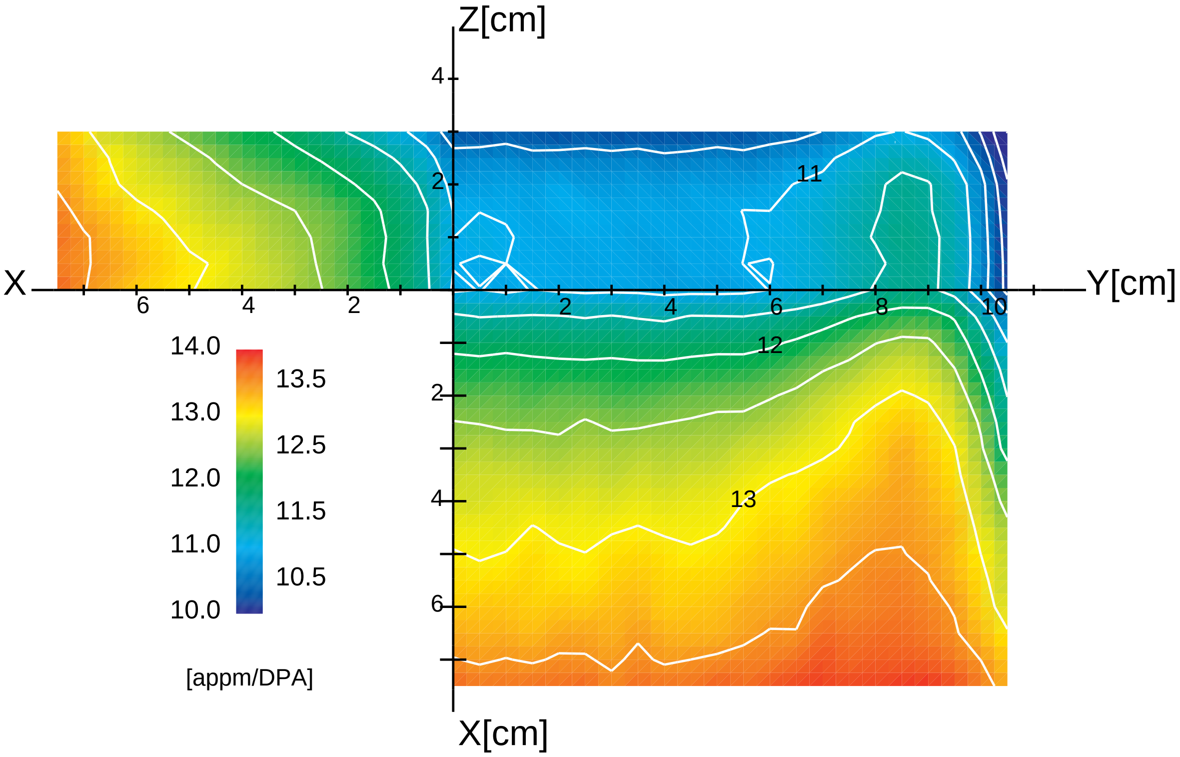

(b) Helium

Figure 5.10: Ratio of gas production rates to damage rates.

well below the DEMO values. The flux tail up to 20 or 30 MeV is needed to achieve the fusion relevant values of these ratios. The gas-to-damage ratios are within the same order of magnitude as the corresponding ratios for fusion reactors, including regions which have the same values as given in table 5.2. The conditions most similar to a DT fusion reactor are close to the backplate, also the region of highest damage and gas production.

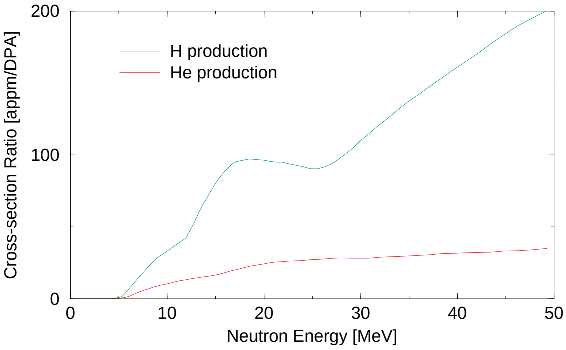

Figure 5.11: Ratio of Gas and Damage Cross-sections in ^{56}Fe.

Figure 5.11 shows the ratio of the gas production cross sections to the damage cross section. The roughly linear increase of the cross section above 14 MeV combined with the rapidly decreasing flux in IFMIF prevents the high energy tail of IFMIF from resulting in unsuitable irradiation conditions. The fast flux is less than 22% throughout the test region, and most of the fast flux is in the energy domain below 30 MeV where the gas-to-damage cross section ratio is still within about 15% of its value at 14 MeV. The non-negligible damage cross section and higher flux in IFMIF below the 5 MeV gas production threshold further compensates for the high energy tail.

5.2.3 Damage Characterisation

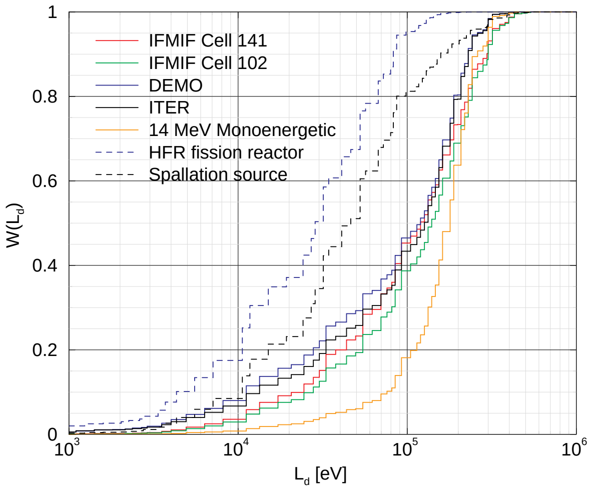

Figure 5.12: Comparison of $W(L_d)$ functions for various spectra.

As discussed previously, the total damage rate as given in table 5.2 is only one measure of the radiation-induced damage of a material. Another is the cumulative distribution function of the PKA damage energy deposition, or the $W(L_d)$ function. Figure 5.12 shows the $W(L_d)$ functions for ^{56}Fe in the IFMIF HFTM, the DEMO first wall, the ITER first wall, a 14 MeV monoenergetic neutron source, the ECN Petten High Flux Reactor [HFR], and a respresentative spallation neutron source (the fission and spallation spectra are from Ref. 56).

The saturation in the Lindhard damage energy partition function means that it is impossible for a PKA to have a damage energy higher than about 1.1 MeV in ^{56}Fe. Therefore, despite the high energy tail of the IFMIF spectrum, 95% of the damage is deposited with a damage energy less than

300 keV, compared to about 230 keV for the fusion spectra. The differences between the spectra in cells 102 and 144 can be seen to have an impact on this $W(L_d)$ function, with the softer spectrum of cell 144 having a response more similar to a fusion reactor. Most importantly, the $W(L_d)$ functions for IFMIF follow those of the fusion reactors most closely throughout.

5.2.4 Activation Characterisation

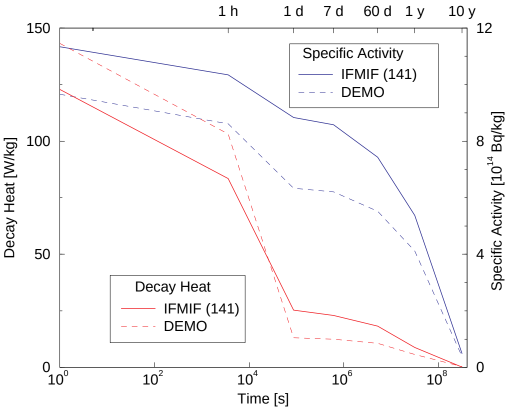

Figure 5.13: Time dependent activation and decay heat in MANET after 10 years of operation. (Cell 141)

The understanding of the neutron-induced activation also benefits from a more detailed analysis. In this case, there are two aspects which can be further explored.

First, the time dependence of the activation is important to both safety, maintenance, and waste disposal issues. Figure 5.13 shows the time dependence of both the specific activity and the decay heat following a 10 year operation with 70% availability (100 days shutdown per year). The activation was calculated for MANET[57] irradiated by the IFMIF flux as well as a DEMO first wall flux.

Additionally, it is necessary to compare the specific inventories of the dominant radioactive isotopes. Table 5.3 compares the dominant radioactive nuclides (those which together make up 98% of the activity) in natural iron and MANET irradiated in the fluxes for both IFMIF and the DEMO first wall. Table 5.4 makes the same comparison for the dominant decay heat sources (those which produce 98% of the decay heat).

Due to the high energy tail, the IFMIF spectra results in a slightly different activation product distribution than the DEMO first wall spectra. The most significant difference is the increased production of ^{54}Mn relative to ^{56}Mn in the IFMIF flux. When combined with the lower decay heat of ^{54}Mn, this is directly responsible for the lower total decay heat in the IFMIF flux. Finally, the longer half-life of ^{54}Mn explains why the decay heat curves cross at a cooling time of about 5 or 6 hours.

5.2.5 Suitability as a DT Simulation Environment

In spite of the large differences between the neutron spectra of IFMIF and those of DT fusion reactors, IFMIF provides an environment well suited to performing fusion material irradiation. Based on the above results for ^{56}Fe, there is over 500 mL of irradiation volume available with a damage rate over 20 DPA/fpy. Using the gas-to-damage ratios

	$^{\mathrm{nat}}$Fe		MANET	
	IFMIF (141)	DEMO	IFMIF (141)	DEMO
TOTAL [10^{14} Bq/kg]	10	8.7	10	8.6
^{55}Fe	68%	64%	58%	56%
^{56}Mn	16%	26%	14%	26%
^{54}Mn	14%	8.6%	13%	8.6%
^{51}Cr	1.6%	1.3%	11%	7.5%
^{58}Co	–	–	1.0%	0.36%
^{49}V	0.04%	–	0.68%	0.60%
TOTAL [%]	99.0%	99.8%	97.7%	98.5%

Table 5.3: Dominant activation products at 1 hour cooling time.

	$^{\mathrm{nat}}$Fe		MANET	
	IFMIF (141)	DEMO	IFMIF (141)	DEMO
TOTAL [W/kg]	90	103	83	103
^{56}Mn	73%	89%	68%	87%
^{54}Mn	21%	9.5%	22%	9.6%
^{52}Mn	3.6%	0.23%	3.4%	0.20
^{52m}Mn	1.1%	–	1.0%	–
^{55}Fe	0.73%	0.51%	0.68%	0.44%
^{51}Cr	0.11%	0.06%	0.79%	0.37%
^{58}Co	–	–	2.1%	0.49%
^{60}Co	–	0.06%	0.20%	0.98%
TOTAL [%]	99.6%	99.4%	98.2%	99.1%

Table 5.4: Dominant decay heat sources at 1 hour cooling time.

and the $W(L_d)$ damage function as the primary measures of its suitability, the entire high flux test region is reasonable for this testing. More importantly, much of the volume has higher damage rates, allowing accelerated testing of samples. Furthermore, the gas-to-damage ratios, $W(L_d)$ damage function and neutron flux gradients are most suitable in these accelerated testing regions.

5.3 Impact on IFMIF Design

The results of this characterisation have various implications for the design of IFMIF as a whole and the High Flux Test Module in particular. In addition to the uncertainty in the neutron source model and corresponding uncertainties in the neutron responses, the shape of the irradiation volumes has an impact on the final size and shape of the HFTM.

5.3.1 Uncertainty in Neutron Responses

Section 4.4 discusses the impact of the Li(d,xn) reaction model uncertainty on the neutron flux uncertainty. All the neutron response data given in this chapter have been based upon the M^{c}DeLi parameter set generated by fitting to the Sugimoto data (parameter set S), but many exhibit a similar dependence on the neutron source uncertainty. Of the primary or secondary responses that determine the suitability of IFMIF as a simulation of DT fusion relevant irradiation conditions, however, only the total DPA rate is significantly affected. Conversely, the lower fast flux fraction in parameter set 'F' only leads to slightly lower gas-to-damage ratios, and the $W(L_d)$ is virtually unchanged. The total available volume, however, is greatly reduced.

In comparison to table 5.1, table 5.5 shows the volumes available when using the 'F' parameter set, and also the average of the results from the two parameter sets. Here, the uncertainty is defined as simply half the width of the range defined by the two values. If the neutron source does behave more like parameter set 'F' than set 'S', other methods may be necessary to increase this volume, such as reflecting more of the flux back into the high flux region (which would beneficially reduce the gas-to-damage ratios) or increasing the beam power.

Displacement damage rate [DPA/fpy]	Volume [cm^3]	
	Set F	Average ± uncertainty
> 20	488	552 ± 64 (12%)
> 30	199	240 ± 41 (17%)
> 40	67	93 ± 26 (28%)
> 50	7	21 ± 13 (62%)

Table 5.5: Uncertainty in available volumes which meet specific damage rate criteria. (also see table 5.1)

5.3.2 HFTM Design and Loading Considerations

It is clear from table 5.1 and figure 5.4 that the rectangular shape of the CDA reference HFTM design does not make optimum use of the available radiation volume. Over a quarter of the irradiation volume with a damage rate over 20 DPA/fpy is outside of the reference HFTM. This strongly suggests design changes in the HFTM to make better use of this volume. Given the non-trivial shape of the irradiation volumes, it is not reasonable to design the HFTM to conform exactly to them. Instead, by simply increasing the size of the HFTM in the x- and z-directions, the total irradiation volume would be included. The HFTM would then have a total volume of over 700 cm^3, of which about 85% would have damage rates greater than 20 DPA/fpy.

The relatively high gradients in some locations has an impact on the loading pattern for the individual probes in the HFTM. The location and orientation of the probes will have to be carefully chosen to minimise the impact of these gradients. One of the requirements given in chapter 1 was a flux gradient of less than 10% across the important region of each probe. The anticipated dimensions of the miniaturised specimen geometries currently being developed by the material testing community are in many cases only a fraction of a centimetre, easily permitting gradients of up to 20 or 30%/cm. In many parts of the high flux test region, the direction of this gradient (perpendicular to the surfaces shown in figure 5.4) is normal to one of the three primary directions. In these regions, is it is easy to imagine a practical specimen orientation which minimises the effect of the gradient. In other domains, such as the back outside corners of the high flux region, the gradient is in a less convenient direction. This is mitigated, however, by the fact that gradient magnitude is lower in those domains.

The gradients are also important when considering the volume gained by enlarging the HFTM. Of the additional volume with damage rates greater than 20 DPA/fpy, most is in a region where the gradients are very large, up to 60 or 70%/cm. This further complicates the loading pattern of the HFTM.

Chapter 6

Summary

The International Fusion Materials Irradiation Facility [IFMIF] is important and necessary for the development of materials for use in future fusion power reactors. The test cell of IFMIF must provide a neutron irradiation environment similar to a DT fusion reactor, allowing the development of a fusion materials database. It is absolutely vital to understand the neutronics behaviour and engineering responses in the high flux region throughout all phases of the design and operation of such a facility. Neutronics characterisations are first necessary to assess the conceptual design's feasibility and will later contribute directly to the engineering design details. The same calculations will be an integral part of the operation and safety of the system once it enters service.

At the current stage in IFMIF's development, neutronics calculations are required for final validation of the conceptual design and early input into the engineering design of components such as the High Flux Test Module. The primary goal of this work has been to provide a basis for the calculation and analysis IFMIF's neutronics characteristics and contribute to the design and development of the project. As a complete set of computational tools and data to perform this analysis at the desired accuracy did not exist, it was necessary to develop new tools, evaluate new data and integrate them with existing components. This activity has produced a flexible system for the future neutronics analysis of IFMIF in all its design and operation phases.

The complete code system has been used to provide a thorough analysis of the IFMIF high flux test region. In addition to the neutron flux spectra and distributions, primary and secondary engineering responses have been calculated to fully characterise the suitability of IFMIF for fusion-relevant irradiation. Having established that IFMIF was able to fulfil its most important design requirements, the neutron responses have been further analysed to provide input into the engineering design and future development of IFMIF neutronics analysis.

6.1 INACS for IFMIF

The Integrated Neutronics Analysis Code System [INACS] has been developed and implemented for performing analyses of the IFMIF test facility. INACS was based on a number of pre-existing components:

- the ENDF-6 nuclear data format,
- the NJOY nuclear data processing code,
- the MCNP Monte Carlo neutron transport code, and
- the ALARA activation code.

In addition, a variety of new components have been developed to facilitate the generic analysis of neutron sources:

- the damChar nuclear damage data processing code and
- the Mcplot.pm and DataPath.pm Perl modules for data post-processing.

Most importantly, specific components have been developed to improve the modelling of the IFMIF neutron source itself:

- new intermediate energy neutron transport and activation data and
- the highly flexible M^{c}DeLi neutron source model package.

In addition to the flexibility in modelling the characteristics of the Li(d,xn) source, the M^{c}DeLi source model provides an efficient way to calculate the source neutrons' initial parameters within the MCNP neutron transport code. The physical models incorporated in M^{c}DeLi fully exploit the Monte Carlo nature of the transport code itself resulting in more physically realistic implementations. While the improved Serber stripping and evaporation models are still only approximations to the real physical processes, they are based on fewer physical assumptions than previous implementations.

6.2 High Flux Region Neutronics

This complete code package has been used to perform a thorough neutronics analysis of the IFMIF high flux test region. In addition to individual neutron spectra, the primary responses of this analysis include the spatial distributions of the total flux, fast flux, damage rate, gas production rates, nuclear heating and specific activity. These primary responses are most important for understanding the irradiation environment which will be available for the miniaturised samples. These values will be used directly by engineering and material scientists to analyse the effects of neutron irradiation on the materials properties.

In this analysis, however, these were used to calculate secondary responses of neutron flux gradients, gas-to-damage production ratios, irradiation volumes, damage characterisation, activation characterisation and decay heat. These secondary responses give direct insight into the ability of IFMIF to fulfill its primary goal as a simulation of a DT fusion environment.

The majority of these responses are within an appropriate range of the values derived from IFMIF's design requirements:

- The irradiation volume is larger than the original specification of 500 cm^3. This response suffers, however, from a large uncertainty.
- Based on the small specimen technology, the neutron gradients throughout most of the test cell are reasonable.
- The gas-to-damage ratios are slightly larger than in a DT fusion environment due to the high energy tail of the neutron flux. Any additional neutron reflection not accounted for in this characterisation, such as from other test modules, will further improve this response.
- The damage characterised by the $W(L_d)$ function shows good agreement with fusion conditions.
- The detailed activation characterisation shows that the activation products in MANET are similar to those caused by a fusion flux spectra.

The locations of the optimum values for each of these responses coincide in a significant volume near the target, offering greatly accelerated testing in a fusion-relevant environment.

Most importantly, the ability to calculate detailed distributions of all of these responses has been demonstrated.

6.3 Future Developments for IFMIF

The results of this work have an impact on many aspects of the IFMIF project's future.

The uncertainty of the Li(d,xn) neutron source term demonstrates the necessity for a full Li(d,xn) cross section evaluation with experimental benchmarks. This is particularly true because of the impact that this uncertainty has on the final responses and on the ability for IFMIF to fulfill its design requirements.

The complete analysis of the neutron flux and the subsequent responses has indicated possible ways to make small conceptual changes which may further improve the IFMIF simulation environment. Increased beam power would be best used by increasing the beam footprint to reduce edge gradients. Adding a reflector would slightly increase the low energy flux in the high flux region, improving the gas-to-damage ratios.

The modelling of the irradiation volumes has demonstrated that direct design changes are necessary for the High Flux Test Module to enable it to make optimum use of the available volume. The neutron flux gradient results provide guidance for designing HFTM loading patterns which minimise the effect of the gradients on the small specimen probes.

Bibliography

[1] Martone, M. (Ed.), "IFMIF - International Fusion Materials Irradiation Facility, Conceptual Design Activity, Final Report," ENEA Frascati Report RT/ERG/FUS/96/11, December 1996.

[2] Toschi, R., "Nuclear Fusion, an Energy Source," Fusion Technology 1996 (C. Varandas and F. Serra, eds.) Elsevier (1997) p. 525.

[3] Hawryluk, R.J. and the TFTR Group, "Results from D-T Experiments on TFTR and Implications for Achieving an Ignited Plasma," Princeton Plasma Physics Laboratory, Report PPL-3318, 1998

[4] Keilhacker, M., "Fusion Physics Progress on JET," Proceedings of the 20th Symposium on Fusion Technology, Marseilles, France (September 7-11, 1998) 5.

[5] Aymar, R., "Status of ITER, July 1998," Proceedings of the 20th Symposium on Fusion Technology, Marseilles, France (September 7-11, 1998) 4.

[6] Dalle Donne, M., *et al.*, "European DEMO BOT Solid Breeder Blanket," Kernforschungszentrum Karlsruhe, Report KFK-5429, November 1994.

[7] Daum, E., *et al.*, "Neutronics of the High Flux Test Region of the International Fusion Materials Irradiation Facility [IFMIF]," Forschungszentrum Karlsruhe, Report FZKA 5868, June 1997.

[8] "ENDF-102: Data Formats and Procedures for the Evaluated Nuclear Data File, ENDF-6," McLane, V., C.L. Dunford, and P.F. Rose, Eds., BNL-NCS-44945, Rev. 2/97

[9] MacFarlane, R. E., "The NJOY Nuclear Data Processing System, Version 91", Los Alamos National Laboratory, Report LA-12740-M, 1994

[10] Briesmeister, J. F. (Ed.), "MCNP – A General Monte Carlo N-Particle Transport Code, Version 4B", LA-12625-M, 1997

[11] Forrest, R. A., and J-Ch. Sublet, "FISPACT 97 - User Manual," UKAEA FUS 358, May 1997.

[12] Sisolak, J., *et al.*, "DKR-PULSAR 2.0: A Radioactivity Calculation Code that Includes Pulsed/Intermittent Operation," to be published.

[13] Attaya, H., "Radioactivity Computation of Steady State and Pulsed Fusion Reactor Operation," *Fusion Eng. and Design*, **28** 571 (1995).

[14] Mann, F., "REAC*2: Users Manual and Code Description," Westinghouse Hanford Company report, WHC-EP-0282, December 1989.

[15] Wilson, P. P. H., and D. L. Henderson, "ALARA: Analyic and Laplactian Adaptive Radioactivity Analysis, Volume I, Technical Manual," University of Wisconsin Fusion Technology Institute, UWFDM-1070, January 1998.

[16] Greenwood, L.R., "SPECOMP: Calculations of Radiation Damage in Compounds," Reactor Dosimetry: Methods, Applications, and Standardization (ed. H. Farrer, E.P. Lippincott) ASTM-STP-1001 598 (1989).

[17] Lindhard, J., V. Nielsen and M. Scharff, "Integral Equations Governing Radiation Effects," *Mat.-fys. Medd.* **22** no.10 (1963).

[18] Norgett, M.J., M.T. Robinson and I.M. Torrens, "A Proposed Method of Calculating Displacement Dose Rates," *Nuclear Eng. and Design* **33** 50 (1975).

[19] Leichtle, D., "Strahlungsinduzierte Gitterschädigung leichter Materialien in Fusionsreaktorblankets," Forschungszentrum Karlsruhe Report, to be published.

[20] "System Programming or Scripting?" *Tcl & Scripting* 1998 <http://www.scriptics.com/scripting/choose.html> (9 October 1998).

[21] Wall, L., T. Christiansen and R.L. Schwartz Programming Perl, 2^{nd} Edition, Sebastopol, CA: O'Reilly & Associates Inc., 1996.

[22] Ousterhout, J. K., Tcl and the Tk Toolkit, Reading, MA: Addison-Wesley, 1994.

[23] Sublet, J.-Ch., Kopecky, J., and Forrest, R.A., "The European Activation File: EAF-97 - Cross section library" UKAEA Fusion *Report UKAEA-FUS-351*, June 1997

[24] Pashchenko, A.B., *et al.*, "FENDL/A-2.0 Neutron activation cross section data library for fusion applications", International Atomic Energy Agency report IAEA(NDS)-173 (IAEA October 1998).Data library retrieved online from the IAEA Nuclear Data Section.

[25] Shubin, Yu.N., *et al.*, "MENDL-2 Neutron reaction data library for nuclear activation and transmutation at intermediate energies," International Atomic Energy Agency report IAEA(CCP)-385 (1995).

[26] Monti, S., "Shielding and Activation Analysis" in Proceedings of the IEA-Technical Workshop on IFMIF Test Facilities, Karlsruhe, Germany (July 7-9, 1997), Forschungszentrum Karlsrhue report, FZKA 5993, 115 (December 1997).

[27] Greenwood, L.R., "Extended H- and He-production data up to 44 MeV and extended damage energy cross sectiosn up to 50 MeV," private communication, 1992.

[28] Korovin, Yu.A., *et al.*, "Evaluation and Test of Nuclear Data for Investigation of Neutron Transport, Radiation Damage and Processes of Activation and Transmutation in Materials Irradiated by Intermediate and High Energy Particles," Nuclear Data for Science and Technology, (Reffo, G., Ventura, A., and Grandi, C., Eds.) Editrice Compositori (1997) p. 851.

[29] Chadwick, M.B., *et al.*, "Cross Section Evaluations to 150 MeV for Accelerator-Driven Systems and Implementation in MCNPX," Los Alamos National Laboratory report LA-UR-98-1825 (1998); submitted to Nuclear Science and Engineering (1998) .

[30] Korovin, Yu.A., *et al.*, "Radiation Damage and Process of Activation and Transmutation in Materials Irradiated by Intermediate and High Energy Particles," *presented at the 9th Int'l Conf. on Emerging Nuclear Energy Systems [ICENES]*, Tel Aviv, Isreal, June 26-July 2, 1998

[31] Ziegler, J.F., *et al.*, The Stopping and Range of Ions in Solids, Volume I, Pergamon Press, 1985.

[32] Lone, M.A., *et al.*, "Thick Target Neutron Yields and Spectral Distributions from the ^{7}Li(^d_p,n) and ^{9}Be(^d_p,n) Reactions," *Nuclear Instruments and Methods* **143** 331 (1977).

[33] Weaver, K.A., *et al.*, "Neutron Spectra from Deuteron Bombardment of D, Li, Be, and C," *Nuclear Science and Engineering*, **52** 35 (1973).

[34] Brede, H.J., *et al.*, "Neutron Yields from Thick Be Targets Bombarded with Deuterons or Protons," *Nuclear Instruments and Methods*, **A274** 332 (1989).

[35] Saltmarsh, M.J., *et al.*, "Characteristics of an Intense Neutron Source Based on the d+Be Reaction," *Nuclear Instruments and Methods*, **145** 81 (1977).

[36] von Möllendorff, U., H. Feuerstein and H. Giese, "Measurements of Radioactivity Production in the IFMIF Target," Proceedings of the 20th Symposium on Fusion Technology, Marseilles, France (September 7-11, 1998) 1445.

[37] Ajzenberg-Selove, F., "Energy Levels of Light Nuclear A=5-10," *Nuclear Physics* **A490** 1 (1988).

[38] Christensen, P.R. and C.L. Cocke, "Neutron Decay of the 2.43 MeV and 3.03 MeV States in ^{9}Be to ^{8}Be(g.s.)," *Nuclear Physics* **89** 656 (1966).

[39] Heggie, J.C.P. and P.W. Martin, "Angular Correlation Measurements in the ^{7}Li(d,nα)^{4}He Reaction," *Nuclear Physics* **A212** 78 (1973).

[40] McClenahan, C.R. and R.E. Segel, "Cross sections for the ^{7}Li(d,p)^{8}Li, ^{6}Li(^{3}He,n)^{8}B, ^{6}Li(d,α)^{4}He, ^{6}Li(d,p)^{7}Li, ^{6}Li(d,n)^{7}Be reactions," *Physical Review C* **11** 370 (1975).

[41] Mann, F.M, F. Schmittroth and L.L. Carter, "Neutrons from d+Li and the FMIT Irradiation Environment," Hanford Engineering Development Laboratory report HEDL-TC-1459 (November 1981).

[42] Serber, R., "The Production of High Energy Neutrons by Stripping," *Physical Review* **72** 1008 (1947).

[43] August, L.S., *et al.*, "Stripping-theory Analysis of Thick-target Neutron Production for d+Be," *Physics of Medicine and Biology* **21** 931 (1976).

[44] Oyama, Y., "Neutron Source Function for given Target-, Beam-, and Energy Parameters," Proceedings of the IEA-Technical Workshop on the Test Cell System for an International Fusion Materials Irradiation Facility, Karlsruhe, Germany (July 3-6, 1995), Forschungszentrum Karlsrhue report, FZKA 5633, 25 (1995).

[45] Blatt, John M., and Victor F. Weisskopf, Theoretical Nuclear Physics, New York: John Wiley & Sons, 1958

[46] Sugimoto, M., "Double-differential Neutron Yields from Li(d,n) Experiments", JAERI, private communication, 1995.

[47] Mann, F.M., "Double-differential Neutron Cross Sections of Li(d,n) Reaction," private communication.

[48] Dancoff, S.M., "Disintegration of the Deuteron in Flight," *Physical Review* **72** 1017 (1947).

[49] Bruhwiler, D.L., "Non-unfiform IFMIF beam profile," Northrop-Grumman Corp., private communication, May 1996.

[50] Lawrence, G.P., *et al.*, "A High-Flux Accelerator-Based Neutron Source for Fusion Technology and Materials Testing," *Journal of Fusion Energy* **8** 201 (1989).

[51] Daum, E., "User and Reference Manual for the KfK Code INS," KFK 5230, Kernforschungszentrum Karlsruhe, September 1993.

[52] Unholzer, S., *et al.*, "Neutron and Photon Spectra in an ITER Shield Mock-up with Open Channel," Proceedings of the 20th Symposium on Fusion Technology, Marseilles, France (September 7-11, 1998) 1357.

[53] Batistoni, P. *et al.*, "Neutron Streaming Experiment for ITER Bulk Shield at the Frascati 14-MeV Neutron Generator," Proceedings of the 20th Symposium on Fusion Technology, Marseilles, France (September 7-11, 1998) 1417.

[54] Sartori, E., "VITAMIN-J, A 175 Group Neutron Cross Section Library Based on JEF-1 for Shielding Benchmark Calculations," JEF/DOC-100 (October 1985).

[55] Fischer, U. and M. Sawan, "Three-dimensional Neutronics Analysis for the Electron Cyclotron Wave Heating System of ITER," Fusion Technology 1994 (K. Herschbach *et al.*, eds.) Elsevier (1995) p. 525.

[56] Daum, E., Forschungszentrum Karlsruhe, August 1997.

[57] Schirra, M., *et al.*, "Untersuchungen zum Vergütungsverhalten, Umwandlungsverhalten und der mechanischen Eigenschaften am martensitischen Stahl 1.4914 (NET-Charge MANET-1)", Forschungszentrum Karlsruhe, Report KFK 4561, 1989.

Acknowledgements

At this point I wish to thank all those people who have supported me professionally, technically, and morally throughout the development of this research. While I cannot list them all here, certain groups and individuals are deserving of special acknowledgement.

This work was carried out in the Institut für Neutronenphysik und Reaktortechnik (INR) at the Forschungszentrum Karlsruhe (FZK) with the support of the European Community. I gratefully acknowledge the assistance of all my INR colleagues, and in particular, R. Bohrmann and Dr. C. Broeders for helping me push the envelope of my technical expertise.

Prof. Dr.-Ing. G. Keßler is deserving of particular recognition for providing valuable feedback and guidance while presiding over my research and for allowing me to carry out the research in the above institute. Also for Profs. D. Cacuci and K. Ehrlich, whose careful reading of and feedback on this dissertation were invaluable.

I am indebted to the entire FZK IFMIF group, especially Drs. E. Daum, A. Möslang, and U. von Möllendorff, who have given this work a broader context and who, through my discussions with them, helped me understand why it needed to be done.

Special thanks are due to Dr. U. Fischer, whose day-to-day support and feedback have guided me throughout and helped keep the goals of this work in focus. Hours of discussion with Dr. Y. Tsige-Tamirat have led to many new insights, both professionally and personally.

Le centinaia di pause per il caffé, piene di elucubrazioni filosofiche morali, politiche e professionali di marcato stampo italiano saranno ricordate sempre con grande piacere.

Finally, a very special thanks to my wife, Laurie Nagus. In addition to her unwavering confidence in my abilities, her careful reading and non-technical eye have greatly contributed to the quality of this dissertation.

Appendix A

Detailed Description of M^{c}DeLi Input Parameters

These parameters were first introduced in section 3.2.6 and shown in figure 3.9. The parameters for the neutron source use 15 of the `SI` source description cards of the normal MCNP input with an optional `SC` comment card. Figure A.1 shows a sample input listing for the IFMIF source.

```
SI901 L 1 1                         \$ target number
SC901 Test Of Source Comment
SI902 L 125 125                     \$ beam current
SI903 L 40 40                       \$ beam energy
SI904 L 0 0.174 0.985 0 -0.174 0.985 \$ beam direction
SI905 L 1 0 0 1 0 0                 \$ beam orientation vector
SI906 L 9   0.6  1    9   0.6  1    \$ main y parameters
SI907 L 2   0.6  1    2   0.6  1    \$ main z parameters
SI908 L 8.5 0.25 0.35 8.5 0.25 0.35 \$ first y correction
SI909 L 0   0    0    0   0    0    \$ first z correction
SI910 L 0   10   0.2  0   10   0.2  \$ second y correction
SI911 L 0   0    0    0   0    0    \$ second z correction
SI912 L 0   0 -2.76   0   0 -2.76   \$ beam spot center
SI913 L 1                           \$ program cell number
SI914 L 0 0 1                       \$ target surface normal
SI915 L 0.512                       \$ target density
```

Figure A.1: Sample listing of MCNP input for M^{c}DeLi source description.

While the source module allows an arbitrary number of beams impinging on an arbitrary (and different) number of targets, it is important that each target be defined in the geometry specification of the MCNP input file and that that assigned cell number be used for the parameter below.

A.1 Beam Parameters

The first 12 distribution cards are used to specify all the beam parameters, including the beam profile. The actual distribution numbers are not important, but the order is. Each distribution is either a scalar or vector distribution, with the order of the data in each corresponding to the order of the data in the others. True vector distributions need not be normalised.

1. Target number
   The target data provided in the last 3 source distribution cards will be entered in a specific order. This card indicates, for each beam, which target the beam strikes by indicating the number in this order. Note that this is most likely different from the cell number assigned to this target in the MCNP geometry specification.

2. Beam current [mA]

3. Beam Energy [MeV]

4. Beam Direction vector

5. Beam Orientation vector
   This vector is perpendicular to the beam direction vector (4) and defines the first direction of the beam profile. If the beam profile is mapped on a Cartesian plane normal to the beam direction vector, this is one of the two directions of the Cartesian system which are used to define the beam profile as outlined in section 3.2.5. The other Cartesian direction will be found by simply taking the cross-product of the beam direction vector and this vector.

6. Basic beam profile parameters in 1^{st} direction
   Following the model described in section 3.2.5, this distributions gives three parameters for each beam which define the basic shape of the profile in the direction of the beam orientation vector (5). In this and the following beam profile parameter distributions, the order of the parameters is (centre, standard deviation, magnitude) or, for example, (x_o, σ_{x_o}, m_{x_o}) for the basic shape parameters.

7. Basic beam profile parameters in 2^{nd} direction
   As (6) but in the direction which is calculated by crossing the beam orientation and direction vectors.

8. and (9): First beam profile correction parameters in 1st (2nd) direction [2 cards]
   These parameters are given in the order as defined in (6) for each beam and follow the model outlined in section 3.2.5.

10. and (11): Second beam profile correction parameters in 1st (2nd) direction [2 cards]
    These parameters are given in the order as defined in (6) for each beam and follow the model outlined in section 3.2.5.
12. Beam spot centre vector
    This vector defines the centre position of the symmetric beam spot on the target surface.

A.2 Target parameters

Three cards are used to define the target. As explained in section 3.2.6 it is important that the target, as it is described in the MCNP geometry specification, be larger than the volume in which the beam deposits its energy.

13. MCNP Cell number
    This card lists the MCNP geometry cell numbers for the targets listed as described for card (1). If there are 2 targets, then the MCNP cell numbers for these two targets are ordered to be consistent with card (1).
14. Target normal vector
    This vector indicates a normal to the surface of the target. The primary importance of this is to convert the beam energy density distribution from the Cartesian system described above (normal to the beam direction vector) to a Cartesian system which is parallel to the target surface.
15. Target density [g/cm3]
    This density is only used to determine the track length of penetration of the deuteron, and is important for determining the birthplace of the neutron.

Appendix B

Command Syntax for **INACS** Modules

B.1 Mcplot.pm

The Mcplot.pm module scans and indexes an MCTAL file which can be produced by MCNP containing the tally results in a readable text format. Various information about the problem itself and each individual tally can be garnered directly from the information stored in the data structure defined by this module. The user interface has the following methods, some of which are borrowed from the MCPLOT mode of MCNP itself.

`new(`*`filename`*`)` This method is called to create a new Mcplot.pm object. The *`filename`* argument is required to indicate which MCTAL file should be referenced by this object.

`problem_def()` This method is called with no arguments and returns a Perl hash which is a copy of the Mcplot.pm object's problem member with the following data structure:

> {`title`} Scalar: The title string of the MCTAL file from the MCNP input file.
>
> {`code`},{`version`},{`id`} Scalar: Information about the code and when the problem was run.
>
> {`nps`},{`rnr`},{`dump`} Scalar: The number of particles which have been simulated, how many random numbers have been generated and which dump this is.
>
> {`ntal`} Scalar: The number of individual tallies that were defined in this problem.
>
> {`tally_list`} List reference: The tally numbers defined in this problem.

`tally_rw(`*`tally_num`*`)` This method is used to read the information about a specific tally defined by tally number *`tally_num`*. It returns a Perl hash which is a copy of data contained in the Mcplot.pm object with the following data structure:

{`type`} Scalar: The type of tally, found simply by taking the modulus of the tally number with base 10.

{`part`} Scalar: The particle being tallied in this tally.

{`comment`} Scalar: Possible comments which the user provided for this tally in the MCNP input file.

{`num_bins`} List reference: The number of tally bins in each of the 8 dimensions used to report tally results. The order is the same as defined in the MCPLOT mode documentation.

{`total_bins`} List reference: A flag indicating whether or not the number of bins in the previous object also contains a bin for the total in that dimension. Although this list has an entry for every dimension this option is available only in the last six dimensions.

{`bin_plot_pnts`} List reference: A flag indicating whether or not the bin values are the bin boundaries (0) or the points where the bins should be plotted (1). Although this list has an entry for every dimension it only has meaning for the last three dimensions.

{`bins`} List reference: Each element of this list is a reference to a list of bin values which are either the bin boundaries or bin plot points (see previous data member) for the tally dimension. Although this list has an entry for every dimension it only has meaning for the last three dimensions.

{`num_values`} Scalar: Product of values in `num_bins` times two (one value and one error value) to indicate how many data points are contained in the value section for this tally.

{`num_tfcs`} Scalar: The number of tally fluctuation charts available for this tally.

{`tfc_index`} List reference: The 8-dimensional bin indexes in which the TFC's have been evaluated.

{`tfc_data`} List reference: Each element of this list is a reference to a list of TFC data.

`set(`*`bin_index_bounds`*`)` This method is directly related to the SET command of the MCPLOT mode of MCNP. The argument *`bin_index_bounds`* is a list with one value for each of the 8 dimensions of the tally data. Each of these elements can have three possible entries, the first two of which are identical to those in MCPLOT:

- a single number indicating which bin index should be used in this dimension,

- the string “*” indicating that this dimension should be a free independent variable, or
- a reference to a list, from which the first and last elements will be used to define a continuous range.

This last option is similar to the second option (“*”), but allow the user to exclude some unwanted bins in a specific dimension such as a total bin or initial or leftover segment bins. Up to 8 variables can be declared as free independent variables, in which case, the entire array will be output through the DataPath.pm interface.

`free(`*`free_type`*`)` This method is identical to the FREE command of the MCPLOT mode of MCNP, used to define which variables are free independent variables. The argument *`free_type`* is a list of single character strings following the syntax in the MCPLOT documentation. All variables which were previously declared as free independent variables will be reset to the first bin. Up to 8 variables can be declared as free independent variables, in which case, the entire array will be output through the DataPath.pm interface.

`fixed(`*`fixed_type, fixed_index`*`)` This method is identical to the FIXED command of the MCPLOT mode of MCNP, used to define the bin index of the fixed dependent variables. The two arguments are a single character string defined as for `free()` which defines the dimension and a number defining the index.

`tally(`*`tally_num`*`)` This method defines which tally is the current tally for use by the DataPath.pm interface when generating the output.

B.2 DataPath.pm

The DataPath.pm module provides a generic user interface to a variety of output formats. A sub-module is written for each output format which interacts with the DataPath.pm module through a standardised API.

The DataPath.pm module uses the currently defined tally and array subset of its Mcplot.pm data member. This version of DataPath.pm assumes that the output file requires some variation of the neutron spectrum, and therefore ignores the energy bin indexes (the seventh dimension of the value array), and sends all the neutron energy groups to the sub-module for each of the elements in the array subset.

The user interface has the following methods:

`new(`*`mctal,type,fname,*`*`)` This method creates and initialises a new DataPath.pm object as a link between the already created Mcplot.pm object *`mctal`* and the output file *`fname`* of type *`type`*. All subsequent arguments are passed to the initialising method of the output file sub-module. See the documentation for the particular sub-module for the correct arguments.

`close(*)` This method closes the output file. The arguments are passed directly to the `close()` method of the appropriate sub-module. See the documentation for the particular sub-module for the correct arguments.

`write(*)` This method writes the defined subset of the value array for the currently defined tally to the output file (see the Mcplot.pm module for how to define the current tally and the current array subset). The arguments are passed to the `write_setup()` method of the appropriate sub-module to initialise the write and then each value of the array subset is written to the output file in turn.

B.2.1 Writing new sub-modules

When writing new sub-modules for other output formats, a new entry has to be made in each of the following methods of DataPath.pm: `init()`, `close()`, `write()`. Some output type specific processing can be performed here if necessary, although this should avoided. Otherwise, the first two of these methods simply pass arguments to the `new()` and `close()` methods of the appropriate sub-module described in the following API. The `write()` method calls the internal method which sequentially extracts the energy-dependent fluxes for each element of the Mcplot.pm array subset. It is in this method that you must determine whether the flux passed to the new output format contains the total bin or not, if present in the energy dimension.

The DataPath.pm module API to the sub-modules expects the following methods to exist for each sub-module description:

`new(`*`fname,*`*`)` The constructor for the specific type of output file object. A base filename is passed from the `new()` method of the DataPath.pm module, as well as other arguments as defined in the documentation for each sub-module.

`write_setup(*)` This method takes user input passed from the `write()` method of the DataPath.pm module and processes and stores it where appropriate in the output file object for later use. Some initialisation may also be performed.

`write_next(`*`data`*`)` This method takes a single list of values in the argument *`data`* and writes it to the output file. The data represents a single element of the array subset defined by the Mcplot.pm methods. This routine is also responsible for writing any other information required by that output format.

`close(*)` This method cleans up and closes the output file. If user-defined post-processing of the file is necessary it is done in this method and controlled by the arguments passed through the DataPath.pm API.

The DataPath.pm module provides the method `scale_data(`*`scale,data`*`)` to each sub-module to scale the data as required. The argument *`scale`* can be either a scalar (scalar), a list reference to scalar variables (vector), or a list reference to list references (matrix). For scalar multipliers, each of the elements of *`data`* is scaled accordingly. For vector multipliers, a dot product of the vector and the data is returned and for matrices, the normal matrix product, $\vec{y} = A \cdot \vec{x}$, is returned.

Some data types may need to write summary information at the top of the file or post-process the data after it has all been written but before closing the file. In such cases, it is advisable to open a temporary file in method `new()` and then use the data stored there to create the final file in method `close()`.

B.2.2 Flux.pm and ALARA.pm

The Flux.pm sub-module is used to write the neutron flux vectors to an output format appropriate for viewing or plotting the individual spectra. When creating a new DataPath.pm object of this type, the scaling data is passed as the last argument. This is can be a scalar variable which is used to renormalise the flux, a vector cross section used to calculate a scalar response, or a matrix cross section operator used to calculate a functional response. This module has been used for generating the fluxes for figure 4.6 and the $W(L_d)$ functions in figure 5.12. The implementation of `write()` for ALARA.pm requires no arguments. The `close()` method has an optional argument, ``` ``norm'' ```, which causes the flux of each group to be normalised by the group width. For practical reasons, this module is only able to put 8 fluxes in a single file. This is controlled by the internal `checkLimits()` method.

The ALARA.pm sub-module is a subclass of the Flux.pm module and is used to write the neutron flux vectors to an output format appropriate for the ALARA activation code. When creating a new DataPath.pm object of this type, the scaling data is passed as the last argument. The implementation of `write()` for ALARA.pm requires no arguments. The `close()` method requires a single argument as a comment for the flux file. The 8 flux limitation has been removed by overriding the `checkLimits()` method.

B.2.3 Geom.pm

The Geom.pm sub-module addresses the issue of assigning geometrical coordinates to the tally results extracted from the MCTAL file. As with the Flux.pm sub-module, scaling data should be provided when creating a new object of this type. The power of the Geom.pm sub-module, however, is in its implementation of the `write()` and `close()` methods.

The arguments to the `write()` method of the DataPath.pm object, when implemented for a Geom.pm output type, are three references to lists, x_o, N_x, and x_1, each of length three. These three lists define the initial point in space, the number of points in space, and the final point in space, in each of three dimensions. The number of spatial points defined in this manner should be the same as the size of the array subset defined by the `set()` method of the objects Mcplot.pm data member. The dimensions generally do not follow a standard ordering, but rather, are ordered with the knowledge that the value of first dimension will be changed most rapidly, followed the second and then the third. That is, the values should be ordered to properly coincide with the appropriate tally order, rather than with the particular directions, x, y, or z. These can be sorted when closing the file as described below. For each dimension, the value of the initial point may be either higher or lower than that of the final point.

The arguments to the `close()` method of the Geom.pm implementation of DataPath.pm are a scalar comment and two list references. The first of these list references is the output order and simply defines which order the co-ordinates will be written to the file for each record. The numbers [1,2,3] refer to the order the dimensions were given to the `write()` method. The second list reference, the sort order, is somewhat more complicated and defines the order in which all the records will be sorted. Again the numbers [1,2,3] refer to the order of the dimensions given to the `write()` method. In this case, however, the first number represents the dimension which will be varied most slowly and the last number represents the dimension which will be varied most quickly. If the numbers are negative, that dimension will be sorted in reverse order. This sorting order allows the output to be in a different order than the order in which the tallies are defined in the MCTAL file.

With a little imagination, it is also possible to at least partially process tallies which are not arranged on a regular grid. Two options are available. In simpler cases, where the irregular grid can be considered as a number of overlapping regular grids, each regular grid can be written to the file with the Geom.pm module and then sorted when closed. In more complicated cases, the Geom.pm module would be used to sort the tallies and provide them with arbitrary but unique codes using the coordinates. In a separate user defined process, these codes can then be remapped onto the irregular geometry.

B.2.4 Sample **INACS** Applications

The following commented (#) script was used to transfer some of the data required for the calculations in chapters 4 and 5.

```
#!/usr/bin/perl

# use INACS modules
use Mcplot;
use DataPath;

# make a connection to, read and index the MCTAL file defined
#      by the first command-line argument
my $mctal = Mcplot->new($ARGV[0]);

# make a new dataPath object
my $dataPath;

# info for whole problem
#===========================
#   ordered list of responses to extract
@responseList = ("dpa","he","h");
#   variables described below should be printed in this order
#        change [x,z,y] to [x,y,z]
$print_order = [1,3,2];
#   data should be sorted in this order,
#        with right-most index varying most rapidly
#        - this is the order required by AVS visualisation program
$sort_order = [2,3,1];

# info for cell tallies (type 4)
#=================================
#   geometry of cell tallies goes from [x,z,y]=[8,0,0] to [0.5,5,11.5] in
#         steps of [0.5,0.5,0.5]
@block_geom = ( [8,0,0],[15,10,23],[0.5,5,11.5] );
#   list of cell bins to extract
#         first 264 bins in each cell tally
$cellBins = [0..263];
#   list of segment bins to extract in each cell bin
#         first 16 segments in each cell tally
$cellSegs = [0..15];
#   arguments to set() command
#         this is the list of arguments given to the
#         MCPLOT set() command
@cellSet = ($cellBins,0,0,$cellSegs,0,0,’*’,0);

# info for surface tallies (type 2)
#====================================
#   list used to index surfaces
#         each response has 11 surface tallies
@surfList = (0..10);
# list of segments in each tally
#         use segments 4 through 27 for each
#         surface tally
$surfSegs = [3..26];
# arguments to set() command
#         this is the list of arguments given to the
```

```
#         MCPLOT set() command
@surfSet = (0,0,0,$surfSegs,0,0,'*',0);

# START PROCSESING
# for each response in list
foreach $respNum (0..$#responseList) {

    # user output
    print STDERR "Reading $responseList[$respNum]...\n";

    # create filename
    my $fileName = $responseList[$respNum] . ".dat";
    # calculate the cell tally number and
    #    first surface tally number of
    #    this response
    my $blockTally = ($respNum+1)*10 + 4;
    my $surfOffset = ($respNum+1)*200;

    # set up datapath with new output file of type "Geom"
    #    with a scalar normalisation factor defined by the
    #    second command-line argument
    $dataPath = DataPath->new($mctal,"Geom",$fileName,$ARGV[1]);

    # set the cell tally number
    $mctal->tally($blockTally);
    # set the cell tally subset
    $mctal->set(@cellSet);
    # copy the data to the output file
    $dataPath->write(@block_geom);

    # read each surface tally's info
    foreach $surf (@surfList) {

# calculate the exact tally number
$surfTally = $surfOffset+$surf*10+2;
# set the z value of this surface tally
$z = $surf*0.5;

# set the surface tally number
$mctal->tally($surfTally);
# set the surface tally subset
$mctal->set(@surfSet);
# copy the data to the output file
$dataPath->write([0,$z,11.5],[1,1,23],[0,$z,0]);

    }

    # user output
    print STDERR "Sorting $responseList[$respNum]...\n";
    # sort and close file
    $dataPath->close("",$print_order,$sort_order);

}
```

Appendix C

damChar Damage Data Processor

The **damChar** program is written in $C++$ and performs the relatively simple task of evaluating equations 2.1 and 2.2. **damChar** expects the following from the standard input:

- one line text string as title card in output
- integer indicating number of isotopes in the mixture
- list of isotopes and isotope data, each consisting of:
    - integer isotope ZA number: ZA = Z*1000 + A,
    - real A,
    - real $E_d \equiv$ displacement energy [eV],
    - real $T_\gamma \equiv$ effective gamma damage energy [eV] as defined in SPECOMP,[16] and
    - real $fr \equiv$ isotopic fraction.

Following the first line, there can be any amount type of white space between the numbers.

damChar also expects an data file named `dam.dat` with data for each required isotope in the order of increasing ZA number. Each isotope has the following format:

- integer `nKas` = number of charged particle production spectra
- list of charged particle ZA numbers and masses in format `nKas*`(integer,real)
- integer `nGrps` = number of neutron energy groups
- `(nGrps+1)`*real neutron energy group boundaries
- integer `kaGrps` = number of recoil energy groups
- `(kaGrps+1)`*real recoil energy group boundaries
- for each isotope in library
    - integer ZA number and real mass

  - SPECTRUM for each charged particle in order above
    - ∗ integer number of empty neutron groups
    - ∗ for each subsequent neutron group
      - · integer number of empty recoil groups
      - · integer `numGrps` = number of recoil groups with data
      - · `numGrps`*real production matrix values
  - SPECTRUM for primary knock-one recoil with same format as a SPECTRUM for charged particles
  - `nGrps`*real (n,γ) cross-section

This input is essentially the same information contained in a GENDF output file as produced by the GROUPR module of NJOY. However, since GENDF files contain much more information than required by damChar a preprocessing Perl program, gendf2dat.pl has also been provided. This allows the one-time processing of the GENDF files into the smaller `dam.dat` files for more frequent use.

There are two possible syntaxes depending on whether or note a new `dam.dat` file is being initialised:

```
gendf2dat.pl init < gendf_file > dam.dat
gendf2dat.pl < gendf_file >> dam.dat
```

The initialisation is responsible for writing the flux and recoil energy group structure once at the beginning of the file. The user is responsible for ensuring that the entries are added to `dam.dat` in the correct order and that they all have the same energy group structure.

The output from damChar is written to standard output with the following format:

- one line text string as title card in output
- integer `nGrps` = number of neutron groups
- `nGrps`*real neutron energy group middle points
- `nGrps`*real damage cross-sections
- `nKas` = number of charged particle production cross-sections
- for each of the `nKas` charged particles:
  - integer ZA number
  - `nGrps`*real production cross-sections
- integer `kaGrps` = number of recoil groups

- `kaGrps`*real recoil energy group middle points
- for each of the `kaGrps` recoil energy groups
  - `nGrps`*real $W(L_d, E_n)$ values